Magnesium- and intermetallic alloys-based hydrides for energy storage: modelling, synthesis and properties

Progress in Energy

TOPICAL REVIEW

Magnesium- and intermetallic alloys-based hydrides for energy storage: modelling, synthesis and properties

Luca Pasquini[1,*], Kouji Sakaki[2,*], Etsuo Akiba[3], Mark D Allendorf[4], Ebert Alvares[5], Josè R Ares[6], Dotan Babai[7], Marcello Baricco[8], Josè Bellosta von Colbe[5], Matvey Bereznitsky[7], Craig E Buckley[9], Young Whan Cho[10], Fermin Cuevas[11], Patricia de Rango[12], Erika Michela Dematteis[8], Roman V Denys[13], Martin Dornheim[5], J F Fernández[6], Arif Hariyadi[14], Bjørn C Hauback[13], Tae Wook Heo[15], Michael Hirscher[16], Terry D Humphries[9], Jacques Huot[17], Isaac Jacob[7], Torben R Jensen[18], Paul Jerabek[5], Shin Young Kang[15], Nathan Keilbart[15], Hyunjeong Kim[2], Michel Latroche[11,†], F Leardini[6], Haiwen Li[19], Sanliang Ling[20], Mykhaylo V Lototskyy[21], Ryan Mullen[15], Shin-ichi Orimo[22,23], Mark Paskevicius[9], Claudio Pistidda[5], Marek Polanski[24,*], Julián Puszkiel[5,25], Eugen Rabkin[26], Martin Sahlberg[27], Sabrina Sartori[28], Archa Santhosh[5], Toyoto Sato[29], Roni Z Shneck[7], Magnus H Sørby[13], Yuanyuan Shang[5], Vitalie Stavila[4], Jin-Yoo Suh[10], Suwarno Suwarno[14], Le Thi Thu[5], Liwen F Wan[15], Colin J Webb[30], Matthew Witman[4], ChuBin Wan[31], Brandon C Wood[15] and Volodymyr A Yartys[13]

[1] Department of Physics and Astronomy, University of Bologna, Viale Berti Pichat 6-2, I-40127 Bologna, Italy
[2] National Institute of Advanced Industrial Science and Technology, 16-1 Onogawa, Tsukuba, Ibaraki, Japan
[3] International Research Center for Hydrogen Energy, Kyushu University, 744 Motooka, Fukuoka, Japan
[4] Sandia National Laboratories, Livermore, CA 94551, United States of America
[5] Helmholtz Zentrum Hereon GmbH, Max Planck Str 1, D-21502 Geesthacht, Germany
[6] MIRE-group, Dpto. de Fisica de Materiales, Facultad de Ciencias, Universidad Autonoma de Madrid, C/Tomás y Valiente 7, 28049 Cantoblanco, Madrid, Spain
[7] Faculty of Engineering Sciences, Ben Gurion University of the Negev, Beer Sheva 8410501, Israel
[8] Department of Chemistry, NIS and INSTM, University of Turin, Via Pietro Giuria 7, 10125 Torino, Italy
[9] Physics and Astronomy, Curtin University, GPO Box U1987, Perth, WA 6845, Australia
[10] Center for Energy Materials Research, Korea Institute of Science and Technology, 5 Hwarang-ro 14-gil, Seongbuk-gu, Seoul 02792, Republic of Korea
[11] University Paris-Est Creteil, CNRS, ICMPE, UMR7182, 2 rue H. Dunant, F-94320 Thiais, France
[12] Université Grenoble Alpes, CNRS, Institut Néel, 38000 Grenoble, France
[13] Institute for Energy Technology (IFE), Instituttveien 18, 2007 Kjeller, Norway
[14] Department of Mechanical Engineering, Institut Teknologi Sepuluh Nopember (ITS), Kampus ITS Sukolilo, Surabaya, 60111, Indonesia
[15] Laboratory for Energy Applications for the Future (LEAF), Lawrence Livermore National Laboratory, 7000 East Avenue, Livermore, CA 94550, United States of America
[16] Max Planck Institute for Intelligent Systems, Heisenbergstr. 3, 70569 Stuttgart, Germany
[17] Hydrogen Research Institute, Université du Québec à Trois-Rivières, 3351 Des Forges, Trois Rivières, QC G9A 5H7, Canada
[18] Department of Chemistry and the Interdisciplinary Nanoscience Center (iNANO), Aarhus University, Langelandsgade 140, DK-8000 Aarhus C, Denmark
[19] Hefei General Machinery Research Institute, No. 888, Changjiang West Road, Shushan District, Hefei 230031, People's Republic of China
[20] Advanced Materials Research Group, Faculty of Engineering, University of Nottingham, University Park, Nottingham NG7 2RD, United Kingdom
[21] HySA Systems, University of the Western Cape, Bellville 7535, South Africa
[22] Institute for Materials Research, Tohoku University, 2-1-1 Katahira, Aoba-ku, Sendai, Japan
[23] Advanced Institute for Materials Research (WPI-AIMR), Tohoku University, 2-1-1 Katahira, Aoba-ku, Sendai, Japan
[24] Military University of Technology, 2 Kaliskiego St, PL-00908 Warsaw, Poland
[25] Helmut Schmidt Universität, Holstenhogweg 85, 22043 Hamburg, Germany
[26] Department of Materials Science and Engineering, Technion—Israel Institute of Technology, 3200003 Haifa, Israel
[27] Department of Chemistry—Ångström Laboratory, Uppsala University, BOX 538, SE-75121 Uppsala, Sweden
[28] Department of Technology Systems, University of Oslo, NO-2027 Kjeller, Norway
[29] Shibaura Institute of Technology, 3-7-5 Toyosu, Koto-ku, Tokyo, Japan
[30] Qld Micro- and Nanotechnology Centre, Griffith University, Brisbane, QLD 4111, Australia
[31] Physics Department, University of Science and Technology Beijing, Beijing, 100083, People's Republic of China
† Deceased author.
* Authors to whom any correspondence should be addressed.

E-mail: luca.pasquini@unibo.it, kouji.sakaki@aist.go.jp and marek.polanski@wat.edu.pl

Keywords: hydrogen storage materials, magnesium, intermetallic alloys, multiscale modelling, energy storage, catalysts, nanostructure

OPEN ACCESS

RECEIVED
17 March 2022

REVISED
16 May 2022

ACCEPTED FOR PUBLICATION
19 May 2022

PUBLISHED
8 June 2022

Abstract

Hydrides based on magnesium and intermetallic compounds provide a viable solution to the challenge of energy storage from renewable sources, thanks to their ability to absorb and desorb hydrogen in a reversible way with a proper tuning of pressure and temperature conditions. Therefore, they are expected to play an important role in the clean energy transition and in the deployment of hydrogen as an efficient energy vector. This review, by experts of Task 40 'Energy Storage and Conversion based on Hydrogen' of the Hydrogen Technology Collaboration Programme of the International Energy Agency, reports on the latest activities of the working group 'Magnesium- and Intermetallic alloys-based Hydrides for Energy Storage'. The following topics are covered by the review: multiscale modelling of hydrides and hydrogen sorption mechanisms; synthesis and processing techniques; catalysts for hydrogen sorption in Mg; Mg-based nanostructures and new compounds; hydrides based on intermetallic TiFe alloys, high entropy alloys, Laves phases, and Pd-containing alloys. Finally, an outlook is presented on current worldwide investments and future research directions for hydrogen-based energy storage.

1. Introduction

The storage of renewable energy is one of the greatest challenges that humanity faces today and is a key ingredient of the transition to a carbon-neutral society. The achievement of such an ambitious goal will only be possible through the development of materials that meet strict sustainability and efficiency requirements anticipated for the coming decades [1]. In this scenario, among other well-known families of compounds such as oxides, sulfides and carbides, hydrides are emerging as a promising class of materials for energy storage, as figure 1(a) suggests. The versatile character of the chemistry of hydrogen (H), i.e. its various bonding types with other elements, such as metallic, ionic, or covalent bonding, provides a great variety of compounds with different properties along with promising perspectives for the design and development of novel materials and composites with relevant and useful properties.

Hydrides have witnessed a rapidly growing interest for energy storage purposes over the last two decades, as illustrated in figure 1(b). Among them, magnesium-based hydrides are particularly appealing due to their sustainability, non-toxicity, low density, and abundancy of magnesium. In addition, hydrides based on intermetallic alloys are promising for a number of key enabling technologies such as stationary H storage and H compression, as seen in the commercial success of rechargeable nickel–metal hydride (Ni–MH) batteries.

The Hydrogen Technology Collaboration Programme (Hydrogen TCP), established under the auspices of the International Energy Agency (IEA), aims to promote collaborative H research and development between its member countries [2]. Among a number of tasks created by the Hydrogen TCP, Task 40 addresses energy storage and conversion based on H by developing reversible or regenerative H storage materials [3]. The targeted applications include H storage for use in stationary, mobile, and portable applications, electrochemical storage, and solar thermal heat storage.

Three reviews by experts of IEA—Hydrogen TCP were published recently on Mg-based materials [4, 5] and on the different classes of materials for H-based energy storage [6]. The present review, written by the working group *Magnesium- and Intermetallic Alloys-based Hydrides for Energy Storage* of the Hydrogen TCP-Task 40, is intended to highlight the latest progress achieved as a result of worldwide research on two important families of hydrides. After a general introduction on the thermodynamics of hydride formation and decomposition in section 1.1, section 2 presents multiscale computational modelling of hydride and H sorption processes. Section 3 describes the most widely used synthesis and processing methods for the preparation of hydrides and hydride-forming alloys. Section 4 focuses on Mg-based hydrides, in particular new alloys and compounds (section 4.2), catalysts and additives (section 4.3), and nanostructures (section 4.4). Section 5 is dedicated to various classes of intermetallic hydride-forming alloys, in particular TiFe (section 5.2) Laves phases (section 5.3), high entropy alloys (section 5.4), pseudo-binary alloys (section 5.5) and binary hydrides as model systems (section 5.6). Section 6 presents a short overview of applications involving these hydride families. Finally, a summarizing outlook on future research directions is presented in section 7.

1.1. Thermodynamics of solid-state hydrogen storage

The storage of H in the solid state relies on the reversible phase transformation from a metal to a metal hydride via absorption or desorption of gaseous H_2, as described by the reaction:

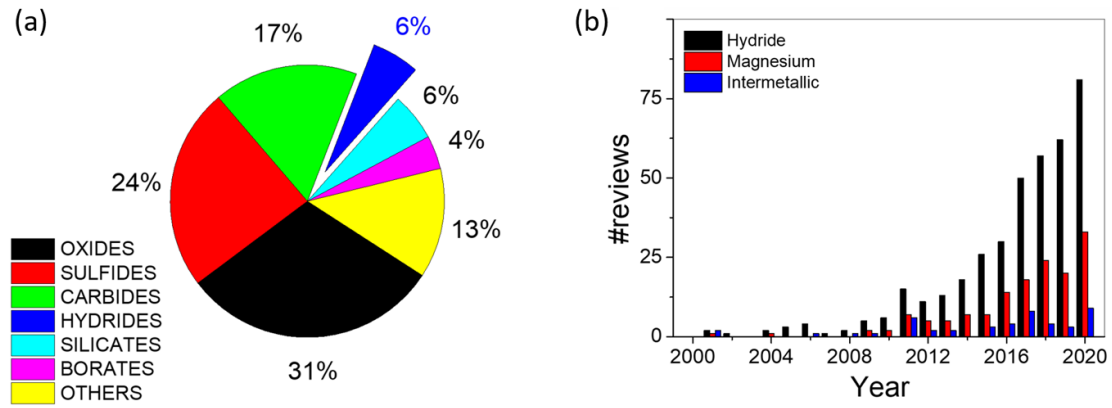

Figure 1. (a) Percentage of published scientific reviews with words 'energy storage' and a type of chemical compounds, i.e. oxides, or sulfides, or carbides, etc, included in keywords, title or abstract during the past two decades (Source: Scopus). (b) Number of published scientific reviews per year with words 'energy storage' and 'hydride', or 'magnesium', or 'intermetallic' included in keywords, title or abstract (Source: Scopus).

$$\mathrm{M\,(s)} + \frac{x}{2}\mathrm{H_2\,(g)} \rightleftarrows \mathrm{MH}_x\,\mathrm{(s)}\,. \tag{1}$$

The entire cycle is enthalpy- and entropy-driven and can be controlled by tuning the H_2 pressure $p\,(H_2)$. The equilibrium pressure $p_{eq}\,(H_2)$, at which the metal is in equilibrium with the hydride and the surrounding H_2 gas depends exponentially on temperature T according to the van 't Hoff equation:

$$\ln\frac{p_{eq}\,(H_2)}{p^\circ} = \frac{\Delta H_r}{RT} - \frac{\Delta S_r}{R} \tag{2}$$

where p° is the standard pressure (usually taken as 1 bar), R is the universal gas constant, and ΔH_r and ΔS_r are the enthalpy and entropy of the reaction per mole H_2 at p°, respectively. Therefore, when $p\,(H_2) > p_{eq}\,(H_2)$, the hydride state is stable and H is absorbed, unless there are kinetic bottlenecks that hamper the reaction. Conversely, when $p\,(H_2) < p_{eq}\,(H_2)$, the metallic state is stable and H_2 release is expected on purely thermodynamical grounds. The complete characterization of thermodynamic equilibrium is accomplished by measuring the so-called pressure-composition isotherms (PCIs), which represent the change of $p_{eq}\,(H_2)$ as a function of the amount of H absorbed in the solid phase. The pressure-composition-temperature (PCT) diagram can then be constructed by collecting PCIs at several temperatures, as discussed in section 2.3. PCT diagrams are important because they convey useful information beyond the ideal van 't Hoff relation, such as sloping plateaus and hysteresis losses, which are crucial for applications.

It should be noted that ΔH_r is not exactly the same as the well-defined enthalpy of formation ΔH_f^o, because the reaction may occur at elevated temperatures. Moreover, ΔH_r often consists of several contributions, e.g. from side reactions due to additives present in composite samples and/or phase changes, such as evaporation of minor amounts of metal, or melting of some components. The reaction enthalpy for H release is usually denoted the *decomposition enthalpy* and is endothermic ($\Delta H_{dec} > 0$) both for magnesium-based hydrides and for the intermetallic hydrides discussed in this review. The decomposition enthalpy is challenging to measure accurately, owing to slow kinetics, and may depend somewhat on the method used for the measurement and on the physical conditions [7].

The relation given by equation (2) also permits the determination of the temperature T_{dec}, above which the hydride decomposes (or vice versa, below which the hydride forms) for a given H_2 pressure. In particular, by setting $p_{eq}\,(H_2) = p^\circ = 1$ bar, one obtains:

$$T_{dec}\,(1\ \mathrm{bar}) = \Delta H_{dec}/\Delta S_{dec}. \tag{3}$$

This value is particularly important for applications since it gives the minimum operational temperature for H_2 release at 1 bar. The *decomposition entropy* ΔS_{dec} (i.e. ΔS_r for H_2 release) is mainly due to the transition of H from bonded in the solid to gaseous, and is thus often quite close to the standard entropy of H_2, i.e. $\Delta S_{dec} \approx S^\circ\,(H_2) = 130.7$ J (K mol H_2)$^{-1}$ [8]. If this is true, then T_{dec} is determined mainly by ΔH_{dec}, and by using equation (3) with $\Delta S_{dec} \approx S^0\,(H_2)$ one obtains that the condition $T_{dec}\,(1\ \mathrm{bar}) = 298$ K corresponds to $\Delta H_{dec} \approx 39$ kJ mol^{-1} H_2. This enthalpy value represents a target for materials that will operate close to ambient conditions. However, dynamic disorder, defects and nano-scale effects in the solid

state can also contribute to ΔS_{dec} [9, 10], leading to significant departures from $S°\,(H_2)$ in systems like nanoparticles (NPs) and high entropy alloys, which are discussed later on in this review.

Two other important parameters for storage applications are the gravimetric H density ρ_m, given by the weight percentage of H in the hydride, and the volumetric H density ρ_V. For MgH_2 these densities are $\rho_m = 7.6$ wt.% H (a reasonably high value that contributes to the popularity of the material) and $\rho_V = 110$ kg H m^{-3}.

The low-temperature proton-exchange membrane (PEM) fuel cell has usually been the target for H applications, which has created a demand for materials with decomposition enthalpies in the range $42 < \Delta H_{dec} < 62$ kJ mol^{-1} H_2 that correspond to $50 < T_{dec}\,(1\,bar) < 200$ °C. For instance, the experimental decomposition enthalpy of MgH_2 is 74 kJ mol^{-1} H_2, whereas the entropy is $\Delta S_{dec} = 133$ J $(K\,mol\,H_2)^{-1}$ [9], which results in $T_{dec}\,(1\,bar) \approx 283$ °C. This is why intense research efforts have focused on changing the thermodynamics of the Mg–MgH_2 system with the aim of lowering its decomposition temperature.

The interest in intermetallic alloys for H storage began in 1958, when Libowitz *et al* discovered that the intermetallic compound ZrNi reversibly stores H and forms $ZrNiH_3$. It contains hydride-forming Zr and Ni with low H affinity. Therefore, the stability of this hydride lies between that of the stable ZrH_2 and the unstable NiH [11]. This was followed by the discovery of Mg_2Ni/Mg_2NiH_4, which has a relatively high capacity (3.6 wt.%), and various room-temperature H storage materials with interesting thermodynamic properties, such as $LaNi_5/LaNi_5H_6$ and $FeTi/FeTiH_2$ [12–15].

These developments led to a new strategy to design (primarily) ternary transition metal (TM) hydrides for H storage. Several new classes of metal compounds were identified with the general formula A_mB_n with *m:n* ratios of 1:2, 1:3, 2:7, 1:5, etc. In this notation, the metallic elements denoted by *A* (examples of which are Mg, Ti, Zr, Y, La, and Ce) exhibit high H affinities, while those denoted by *B* have low H affinities, such as Cr, Mn, Fe, Ni. Many of the ternary hydrides based on A_mB_n intermetallic alloys exhibit excellent reversible H storage behaviour, but their maximum H/metal ratio is typically $H/M \approx 1$; consequently, their gravimetric H storage densities are low [16–18].

The thermodynamic properties of the ternary hydrides are rationalized by the empirical relation denoted *Miedema's rule of reversed stability* [18, 19]. In fact, Miedema's rule is very similar to the well-known Hess law of thermodynamics, which states that the enthalpy change for a reaction is the sum of enthalpy changes for the individual reactions, into which it can be divided. Miedema's rule states that the enthalpy of formation of a ternary hydride is the sum of the enthalpies of formation of the elemental hydrides minus the enthalpy of formation of the alloy. Therefore, a more stable intermetallic alloy (i.e. a more exothermic ΔH_f^o) tends to make the formation enthalpy of the ternary hydride less negative, thus lowering its thermodynamic stability. Miedema's rule provides a useful framework to design intermetallic hydrides optimized for specific applications that require H sorption in a well-defined $p_{eq}\,(H_2)\,, T$ range.

2. Modelling of hydrides

2.1. Multiscale modelling of hydrides: enthalpies, reaction pathways, phase-field methods

2.1.1. Addressing the need for more realistic models

In collaboration with the TCP-Task 40 activities and in conjunction with the US Department of Energy (DOE) HyMARC consortium, Lawrence Livermore National Laboratory has been developing and applying novel computational methods for improving simulations of metal hydrides. These activities are organized along three pillars: (a) incorporating factors beyond idealized thermodynamics to describe evolving surfaces and interfaces during operation; (b) improving multiscale integration from the atomistic to the continuum scale; and (c) tightening experiment-theory feedback through an integrated approach. Wood *et al* recently described several examples of the first pillar in a perspective/review on beyond-idealized models, with a focus on nanoscale metal hydride materials [20]. They highlighted four factors that influence performance and provided potential pathways for accounting for each. First, the authors discussed the role of interface and surface enthalpic penalties in determining reaction pathways. A simple construct for estimating interfacial energies based on weighted fractional surface energies during solid-state metal hydride reactions was applied, and a new statistical analysis was used to predict likelihood of reaction pathway changes. Second, the authors discussed the role of anharmonicity in determining the entropy of surfaces and interfaces. This oft-neglected factor arises from reduced constraint with respect to the bulk, which in turn has implications for understanding enthalpy-entropy compensation effects for nanoscale materials. Third, the authors showed how continuum micromechanics could be used to predict the effects of confinement stresses on reaction enthalpies in metal hydrides confined in a stiff matrix. Finally, the work provided an example of how surface oxidation effects can be incorporated and explored using complex interface models based on *ab-initio* molecular dynamics (MD) and density functional theory (DFT). Examples were introduced to show that

native surface oxidation, which is nearly always overlooked in models, can significantly impact barriers for H dissociation and diffusion.

2.1.2. Mesoscale modelling methods for metal hydride microstructures

Hydrogen storage mechanisms in metals occur by reaction-induced metal-to-hydride phase transformations. Capturing these in kinetically aware, non-equilibrium models represents a grand challenge because the operating mechanisms feature complex coupling of surface/interfacial reactions, diffusion, structural changes, and large volume expansion. Moreover, each of these is a dynamic, atomic-scale process strongly influenced by the microstructures of the parent metal and precipitated hydride to determine thermodynamics and kinetics. Therefore, several modelling approaches that cover different length and time scales must be properly integrated to comprehensively explore the co-evolution of relevant chemical and materials processes. A mesoscale modelling framework can provide a unified platform for integrating atomistic approaches, which typically provide higher accuracy for nanoscale chemical processes. Alternatively, continuum approaches offer far greater flexibility and scalability and can describe materials at the microstructural level. As an example, Heo *et al* recently developed a comprehensive mesoscale modelling framework based on the phase-field method, which integrates key physical factors for simulating metal hydride formation involving large volume expansion in both single-crystal and polycrystalline metals [21]. The model enables analysis of the morphological characteristics of hydride phases involving multiple structural variants and their interactions with grain boundaries. The modelling framework is generally applicable to metal hydride formation and is being extended to account for quantitative description of surface reactions. Another challenge is to simulate nucleation of metal hydride phases, which often occurs at the interface between dehydrided and hydrided phases and cannot be correctly described by conventional models. To this end, Shi *et al* developed a new generalized methodology for predicting the critical nucleus size and the associated energy barrier for phase nucleation at reactive hetero-phase interfaces [22]. This advanced nucleation model extends classical nucleation theory to account for the effects of the chemical potential driving force across the phase boundary. Such mesoscale models can directly incorporate parameters derived from predictive atomistic modelling approaches, including DFT and MD simulations, to simulate microstructure evolution in metal hydrides.

2.1.3. Modelling confinement effects

Another simulation challenge for metal hydrides involves properly capturing the coupling between chemistry and solid mechanics for systems under nano-confinement or nano-encapsulation, which are promising strategies to improve thermodynamics and kinetics. Nano-encapsulation involves a combination of nanosizing, chemical interaction, and confinement, which introduce complex chemomechanical interactions at the encapsulant-hydride interface that are difficult to quantify and decouple yet must be properly accounted for in advanced models. Recently, Kim *et al* [23] performed a detailed experiment-theory analysis to identify three factors contributing to the reaction enthalpy change of Pd/PdH_x ($0 < x < 1$) NPs induced by reduced graphene oxide (rGO) encapsulation: nanosizing, chemical interactions, and strain energy. By combining *ab initio* and classical atomistic computations, high-resolution transmission electron microscopy (TEM), and continuum elasticity theory, each of the three factors was quantified and the collective sum was compared with the measured reaction enthalpy change upon encapsulation. It was determined that all three factors play a non-negligible role in determining the reaction enthalpy and their contributions have similar magnitudes. For instance, the effects of chemical interaction and mechanical strain by the confining medium on the reaction enthalpy were found to be $<+1.6$ and 1.3–2.8 kJ $(\text{mol } H_2)^{-1}$, respectively, and the authors concluded that the net effect was in agreement with the measured enthalpy increase of 3.7 kJ $(\text{mol } H_2)^{-1}$. Such studies can provide a template for future detailed predictions of chemomechanical impacts of nanosizing and nano-confinement on thermodynamics of metal hydrides. These effects could be much larger in stiffer confining media. We point out that the theoretical models used in this study assumed an elastic response and did not directly incorporate plastic deformation. Future work along these lines is recommended to development quantitatively accurate approaches for studying hydriding in a wider array of metal compositions.

In addition to chemomechanics, confinement can also affect kinetic properties associated with cycling of metal hydrides. One example is thermal conductivity, deriving from the fact that the confining host can be an active participant in thermal transport. In principle, this property may be leveraged for overcoming the poor thermal management properties of metal hydrides. Along these lines, Kim *et al* recently established and validated an efficient mesoscale model for computing the thermal conductivities of realistic microstructures [24]. The model was applied to complex microstructures of Mg/MgH_2 confined within rGO composites. The authors used experimental characterization data to reconstruct synthetic digital microstructures. The effective thermal conductivity of the composite was numerically extracted from these microstructures using

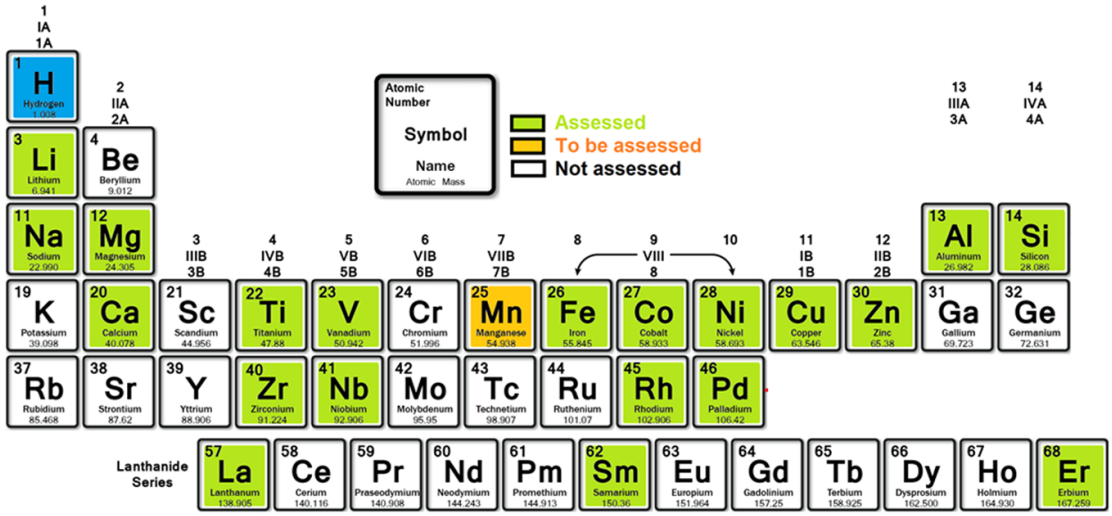

Figure 2. Binary M–H systems evaluated by the CALPHAD method.

the steady-state thermal conduction equation by incorporating individual local thermal conductivity properties of Mg and the rGO host material. The computed effective thermal conductivities are in excellent agreement with measurements, validating the model for complex microstructures. In principle, this mesoscale modelling capability can determine the thermal conductivity of a generic composite with varying porosity, loading ratio, and gas environment.

2.2. CALculation of PHase Diagram (CALPHAD)-assessed thermodynamic databases

Although considerable research has focused on defining new compositions for metal hydride materials, there is still a need for public databases of thermodynamic and structural data, which are currently dispersed in the literature. Developing these databases will accelerate efforts to determine the design rules that dictate thermodynamic properties across the wide chemical and crystallographic space [25].

A powerful approach is the CALPHADs method, which can fit and model experimental and *ab initio* data for metal hydrides across wide compositional, temperature and pressure ranges. Supported by DFT [26], CALPHAD assessments provide a thermodynamic description and model of experimental data that can interpolate properties of multicomponent systems and be used to compute phase equilibria and predict reaction hierarchies [27, 28].

CALPHAD database development and optimization, which integrates various thermodynamic data to create self-consistent models, opens the way for exploring multicomponent materials. It can also compute thousands of thermodynamic data that can be used to develop and validate machine learning (ML) models [29]. The understanding of thermodynamic properties and structure-chemistry relationships will pave the way for prediction and validation of enthalpy and especially entropy values of hydriding reactions that are still unknown.

Tailored CALPHAD approaches are being developed to assess specific H storage materials, including the mixing of different metal hydrides. The goal is to anticipate positive interaction effects on the H storage properties of hydride mixtures or the assessment of ternary compounds. An example is the thermodynamic description of the $NaMgH_3$ phase, for which the available literature data were critically assessed to compute the equilibrium pressure-temperature phase diagram [30]. In another example, the thermodynamics of hydriding–dehydriding in simple hydrides (NaH, AlH_3 and CaH_2) has been included in CALPHAD assessments, providing evidence for either the formation or hindering of a stable hydride–fluoride solid solution that enables a reversible hydriding reaction [31, 32]. Moreover, CALPHAD assessments are able to support further thermo-fluid-dynamic modelling of H absorption and desorption in a $LaNi_{4.8}Al_{0.2}$ material for application in a hydride bed [33, 34].

The development of a unique thermodynamic database for H storage systems by the CALPHAD approach is fundamental and can be implemented by a collection of literature and experimental data, to be integrated with estimations of the energy of formation of hydrides by *ab-initio* calculations [35]. Figure 2 shows a summary of available M–H assessed binary systems, neglecting elements that are not of interest for H storage applications.

The combination of experimental (x-ray diffraction (XRD), volumetric and calorimetric measurements) and theoretical (*ab-initio* calculations) investigations is an especially powerful approach to assess the thermodynamics of metal hydrides systems and to identify structural or chemical relationships. To this end, coupled *ab-initio*, experimental, and thermodynamic CALPHAD assessments were performed for the Mg–Al–H and TiFe–H systems [36–38].

In the case of the La–Ni–Al–H intermetallic-based systems [39], the CALPHAD assessment predicted the role of para-equilibrium, which combines thermodynamic and kinetic aspects in the H sorption–desorption reactions [40]. This is primarily a characteristic of multicomponent hydrides and is mainly related to sloped plateaus observed in PCT isotherms in this material. These are the result of fast H diffusion in the solid state and limited continuous redistribution of metallic elements during hydriding to form the fully hydrided compound [40]. When para-equilibrium occurs, the chemical potential of H becomes nearly equal in the two co-existing phases, whereas the alloy maintains its composition. With some care, the CALPHAD method can be used to describe these metastable conditions. A special case is the hydriding of TiFe, in which the formed hydrides retain the intermetallic ordered structure (B2) under mild conditions but disorder at higher temperature and pressure [41]. Under ambient conditions, the system is not in complete equilibrium and tends to disproportionate into $Fe_2Ti + TiH_2$, given sufficient time [42]. Alvares *et al* demonstrated the use of CALPHAD to assess thermodynamic parameters under these non-equilibrium conditions by considering a pseudo-binary system in which the different metals are considered as one species and by applying parameters of the ordered B2 phase taken from a previously assessed order–disorder model of the TiFe body-centred cubic (BCC) phase. Despite the crystallographic complexities, especially concerning the phase transition between the hydrides, this CALPHAD assessment agrees with most previously reported thermodynamic data and represents the first complete assessment of a system solely utilizing the open-source thermodynamic software OpenCalphad [38, 43, 44].

2.3. Modelling of pressure-composition-temperature (PCT) diagrams for optimization of metal hydride behaviour in hydrogen storage and compression

The use of metal hydrides in H storage and compression applications requires the knowledge of physical parameters that describe the M–H interaction on both micro- and macro-scale.

This needs a precise determination of thermodynamic equilibrium in the M–H system to establish an interrelation between T, $p_{eq}\,(H_2)$, and H concentration in the solid C_H, which enables constructing a PCT diagram for a hydride-forming metal or intermetallic alloy in the temperature-pressure range that corresponds to the operating conditions of the target application. The PCT diagram allows the reversible H sorption capacities at the conditions of H absorption and desorption to be directly determined [47], as shown in figure 3. The PCT interrelations at variable p_{eq}, T, and C_H form a core of the governing equations for the heat-and-mass transfer calculations when developing metal hydride reactors for H storage and compression [48–51].

2.3.1. Modelling of multi-segment PCT diagrams

Modelling PCT diagrams is a powerful tool for evaluating the H sorption properties of metal hydrides followed by performance optimization of the reactors for H storage, compression, and heat management applications. Conventionally, this is done in a simplified way when p_{eq} at a given T and C_H corresponding to plateau midpoint are calculated by using the van 't Hoff equation modified by applying additional empirically derived terms, which account for a plateau slope and absorption/desorption hysteresis [50, 51]. Application of this approach is simple, straightforward and time efficient. However, it results in unacceptably high errors beyond the pressure—temperature limits of the experimental PCT diagrams used for the determination of the empirical coefficients. Moreover, it is not applicable to PCIs containing several plateau segments.

The modelling of the multi-segment PCT diagrams requires application of more accurate PCT models based on statistical and/or thermodynamic prerequisites [46, 52–55] and results in realistic extrapolations. The latter feature is important for the mixtures of metal hydrides (see one typical example in figure 3) and is usually realised following the scheme suggested by Kierstead, which consists of modelling a multi-segment PCI by the superposition of independent single-segment ones [56]. This method yields adequate fitting of the data when the binding energies of H atoms in different types of interstitial sites are significantly different, while the interactions between the H atoms can be neglected, resulting in appearance of the plateau segments at two or more distinct pressures. Unfortunately, accounting of H–H interactions brings a significant sophistication to the modelling procedure, making it impossible to derive an analytical solution if the number of interstitial sites exceeds two [57].

Nevertheless, the combination of theoretical and empirical methods attains a reasonable accuracy in the modelling of both single- and multi-segment PCT diagrams. Mostly, semi-empirical approaches are used when modelling sloping plateaus by introducing a convolution of the $C_H\,(p_{eq}, T)$ dependences

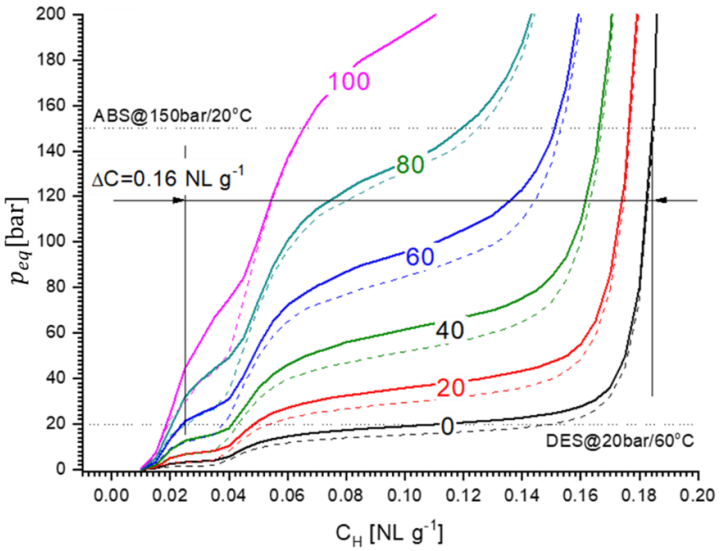

Figure 3. Results of the modelling of a PCT diagram for the mixture 90 wt.% $Ti_{0.65}Zr_{0.35}(Mn,Cr,Fe,Ni)_2$ + 10 wt.% $La_{0.8}Ce_{0.2}Ni_5$ used for H storage on-board fuel cell forklift [45]. The simulated PCT diagram for H_2 absorption (solid lines) and desorption (dashed lines) isotherms was built by fitting the experimental data for the constituent intermetallic alloys using a model [46]. Curve captions correspond to the temperatures of the isotherms [°C]; the value of ΔC specifies the reversible H sorption capacity at the absorption (ABS) and desorption (DES) conditions (dotted lines).

[46, 52, 58, 59]. The semi-empirical modelling describes the whole PCT diagram by using a set of physical parameters that represent the interactions in the system, such as critical temperature, hysteresis losses, enthalpy and entropy of the hydride formation. In addition, semi-empirical parameters are introduced to account for the dependences of plateau slopes on both T and C_H. Lototskyy [52] provides a detailed discussion of these methods along with the description of a software package used to implement them.

2.3.2. Modelling alloying effects on PCT diagrams

The thermodynamics of hydride formation by an element M, as described by equation (4), can be tailored via alloying with an element A that does not react with H but forms either a disordered solid solution or an ordered compound M_nA with M. A good example is provided by the ordered intermetallic compound Mg_3Cd [60]. During H absorption by this system, MgH_2 is leached from the Mg–Cd alloy, which becomes enriched with Cd as illustrated in figure 4. The overall reaction is a modification of the simple equation (4) that can be written as a function of the amount of absorbed H_2 as (assuming that M forms a di-hydride):

$$M_nA + yH_2 \rightarrow M_yH_{2y} + M_{n-y}A. \tag{4}$$

The composition-dependent equilibrium H_2 pressure for this process is described by the equation:

$$p_{\mathrm{eq}}(y) = p_{M-\mathrm{H}} \exp\left(-\frac{\mu_M(y)}{RT}\right) \tag{5}$$

where $\mu_M(y)$ is the composition-dependent chemical potential of M in the $M_{n-y}A$ phase, and $p_{M-\mathrm{H}}$ is the equilibrium pressure for the elemental M–H system. The expression for $\mu_M(y)$ can be obtained employing the CALPHAD framework or other available thermodynamic databases. The calculation of $p_{\mathrm{eq}}(y)$ using equation (5) finally yields the PCT diagram, as shown for the hydriding of Mg_3Cd in figure 4 [60].

Equation (5) can be used for estimating the effects of various factors on the PCT diagram. Let us compare the potentials to increase the plateau pressure in the PCT diagram by manipulating the alloy's thermodynamics, and by elastic stresses in the hydride phase. A good order-of-magnitude estimate of the increase in plateau pressure that can be achieved by manipulating the alloy's thermodynamics can be made by assuming $\mu_M \approx -RT$. This corresponds to assuming that the configurational entropy term is the leading one in defining the Gibbs free energy of the solid solution. Employing suitable parameters for Mg, i.e. $T_{\mathrm{dec}} \approx 570\,\mathrm{K}$ and molar volume $\bar{V}_M \approx 14\ \mathrm{cm^3\ mol^{-1}}$ yields $\mu_M/\bar{V}_M \approx -340\ \mathrm{MJ\ m^{-3}}$.

On the other hand, the elastic stresses that develop in the hydride phase due to the large volume expansion tend to increase its enthalpy, which in turn makes the ΔH_r of H absorption less negative, thus increasing p_{eq}. While this effect is negligible in the case of hydride particles significantly larger than 1 μm because they experience a brittle fracture at the moderate stress levels, smaller particles can sustain large

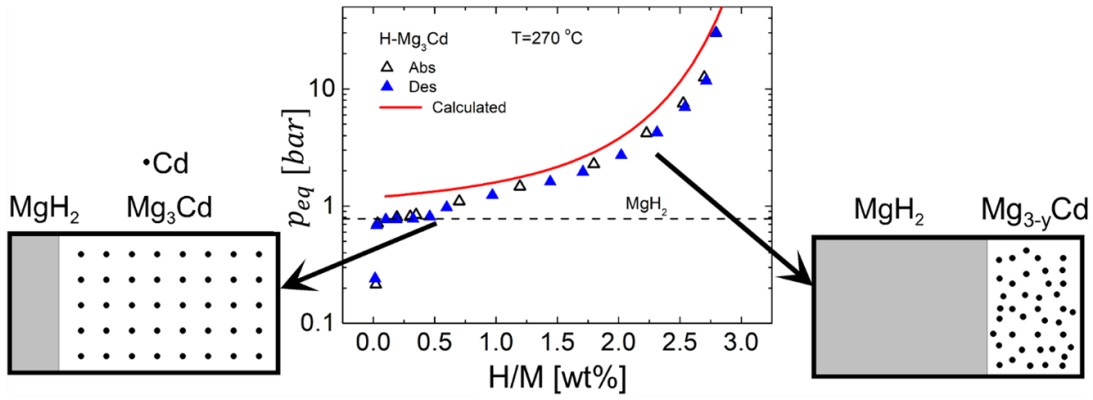

Figure 4. The PCT of the Mg_3Cd phase measured at 270 °C (points) with superimposed red line describing the pressure plateau calculated according to the thermodynamic model. The dashed line shows the calculated plateau pressure for MgH_2 formation at the same temperature using thermodynamic data from the literature. The rejection of Cd atoms by growing MgH_2 into the residual metal phase is schematically shown. The decrease of the chemical potential of Mg in the residual metal phase causes an increase in p_{eq}. Note that $p_{eq}(y) \to +\infty$ for $3 - y \to 0$ (infinite Mg dilution). Reprinted from [60], Copyright (2012), with permission from Elsevier.

stresses approaching the theoretical strength limit of the considered material [61, 62]. The corresponding contribution of the elastic stress energy to the chemical potential of Mg atoms in MgH_2 depends on the morphology of the MgH_2 phase and the nature of its interface with the metal or with the confining medium. In the case of fully coherent metal–hydride interface this contribution can be estimated as $0.5E\varepsilon^2$, where E and ε are the elastic modulus of MgH_2 and elastic strain in it, respectively. The value of E estimated by employing the nanoindentation method is about 65.4 GPa [29]. Based on literature data on compression of metallic [61] and ceramic [62] NPs, the value of $\varepsilon = 5\%$ will be employed as an estimate of the maximum elastic strain that can be sustained by a NP of the hydride phase. Formally, the shift of the plateau pressure due to the increased chemical potential of Mg in MgH_2 can be described by assigning an opposite change of μ_M in equation (5). With the above values one obtains a stress-induced effect $\mu_M/\bar{V}_M \approx -82$ MJ m^{-3}, i.e. only about one-fourth of the effect associated with depleting Mg in the Mg–Cd alloy. On the other hand, when the metal–hydride interface, or the interface of hydride phase with confining medium are incoherent (i.e. can serve as perfect source/sink of vacancies) the contribution of stress to the chemical potential of Mg atoms in the hydride phase can be estimated as $-\sigma_n \Delta\bar{V}_M/\bar{V}_M$, where σ_n is the normal stress at the interface, and $\Delta\bar{V}_M$ is the change of atomic volume of Mg associated with the transition of Mg atom from metallic to hydride phase. Assuming $\sigma_n \approx E\varepsilon$ yields $\mu_M/\bar{V}_M \approx -740$ MJ m^{-3}, i.e. higher than the thermodynamic contribution. Therefore, it can be concluded that elastic strain engineering can be utilized on par with manipulating the chemical composition of the hydride-forming alloy to modify its thermodynamics. The morphology of the hydride phase and the nature of its interface with the metal and/or confining medium are the critical parameters that need to be studied in more detail.

2.4. Modelling of thermal desorption spectroscopy (TDS)

The investigation of gas–solid interactions can be carried out by thermal analysis techniques that measure physical parameters as a function of temperature during a heating/cooling ramp [63, 64]. Differential scanning calorimetry (DSC) measures the absorbed/released heat that accompanies chemical reactions or phase transformations in the material. TDS employs a mass spectrometer to determine both the amount and nature of gaseous species released from a solid sample due to bulk and/or surface reactions. The release of a given gaseous species typically yields a peak in the TDS traces, the peak temperature and area being linked to the binding energy and the amount of the species, respectively. Both DSC and TDS are considered as powerful tools to study the thermal decomposition of various metal hydrides, including MgH_2 [65, 66] and rare earth (RE) hydrides [67, 68].

The application of Kissinger's method [69, 70] and its numerous modifications [70–73] makes it possible to determine the activation energy of the thermal decomposition reaction by analysing the peak shifts as a function of the heating rate. Furthermore, the shape analysis of TDS or DSC peaks provides other important kinetic parameters [71–75]. Most frequently, this analysis is based on the Johnson–Mehl–Avrami–Kolmogorov (JMAK) kinetic equation [71, 72, 74], although other rate-limiting mechanisms can be considered as well [72, 73]. Recently, the activation energies of hydrogen desorption estimated from the Kissinger plots of both TDS and DSC data in $Mg_2Fe_xCo_{1-x}D_y$ alloys were reported to be consistent [76]. In

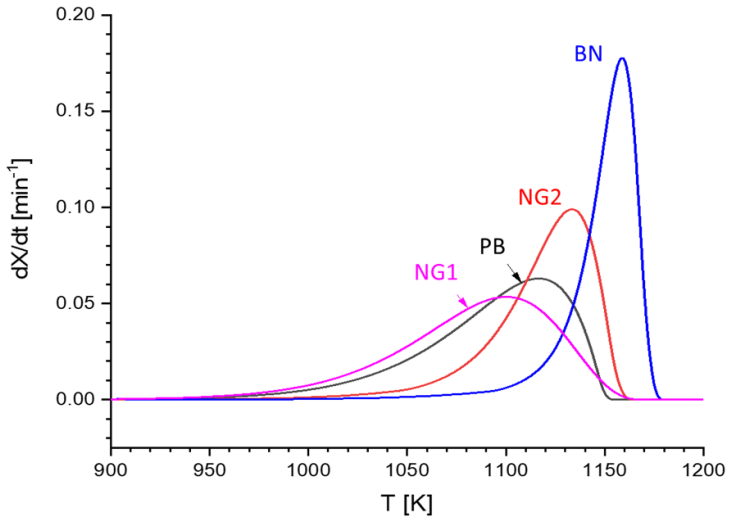

Figure 5. Calculated TDS peaks for the several typical reaction mechanisms of hydride decomposition. NG1: nucleation and growth with Avrami exponent $n = 1$; NG2—nucleation and growth with $n = 2$; BN: branching nuclei interacting during their growth; PB: phase boundary reaction (3D interface moving with a constant velocity). The spectra were simulated for a heating rate of 5 K min^{-1} assuming the same kinetic parameters: $\ln(K_0\ [\mathrm{min}^{-1}]) = 24.7$, $E_A = 256$ kJ mol^{-1}, and transformed fraction at the maximum $X_m = 0.6$.

addition, the activation energies in $La_7Sm_3Mg_{80}Ni_{10}$–$5TiO_2$ and $La_{10-x}Ce_xMg_{80}Ni_{10}$ alloys were determined from both Kissinger plot and JMAK analysis, obtaining consistent results [77, 78].

One general modelling approach, described in [73], uses a combined form of the differential kinetic equation proposed by Šesták and Berggren [79]:

$$\frac{\mathrm{d}X}{\mathrm{d}t}(T,X) = K_0 \exp\left(-\frac{E_A}{RT}\right) \times X^M \times (1-X)^N \times [-\ln(1-X)]^P \tag{6}$$

where X is the transformed fraction, K_0 is a pre-exponential rate factor, and E_A is the activation energy. Different rate-controlling mechanisms, such as nucleation and growth or phase boundary reaction with a constant interface velocity, give rise to specific peak positions and shapes of the desorption traces as exemplified in figure 5. The various possible mechanisms are described in detail in [73]. This approach was successfully applied to assess the mechanisms and the activation energies of thermal decomposition of the RE hydrides [68] and nanocomposites based on MgH_2 [73]. Such a consideration was recently extended to the modelling of multi-peak thermal analysis data [80].

3. Synthesis and processing methods

This section provides a short overview of processing methods employed for the fabrication of hydride-forming alloys and metal hydrides with improved H sorption properties. Melting and casting have always been, and continue to be the method of choice for producing hydride-forming alloys (section 3.4). This method can be easily up scaled, yet resulting microstructures are in most cases quite coarse, which may cause a slow H sorption kinetics. Casting of eutectic compositions may be used for producing nanocrystalline microstructures in the as-cast state. The mechanochemical methods currently are the most widescale used synthesis method of hydride-forming alloys and their hydrides (section 3.1). Nanostructuring and metastability can be easily achieved by increasing the input of mechanical energy, while the contamination of the final product by the milling media appears an issue. Recently, nanostructuring methods adapted from the classical metallurgy, such as severe plastic deformation (SPD) (section 3.2) and forging (section 3.3) have gained increased attention because they combine the advantages of melting/casting and mechanochemical methods. Finally, the gas phase condensation method is a good example of the bottom-up fabrication method of nanostructured hydride-forming alloys (section 3.5). Figure 6 summarizes the synthesis and processing methods considered in this section, and their effect on the microstructure and properties of the resulting materials.

3.1. Mechanochemical methods of synthesis and modification

Mechanical milling, or mechanochemistry, is a versatile and efficient method to reduce particle sizes and induce defects in materials, and is extensively used to prepare a wide range of materials. Mechanochemical

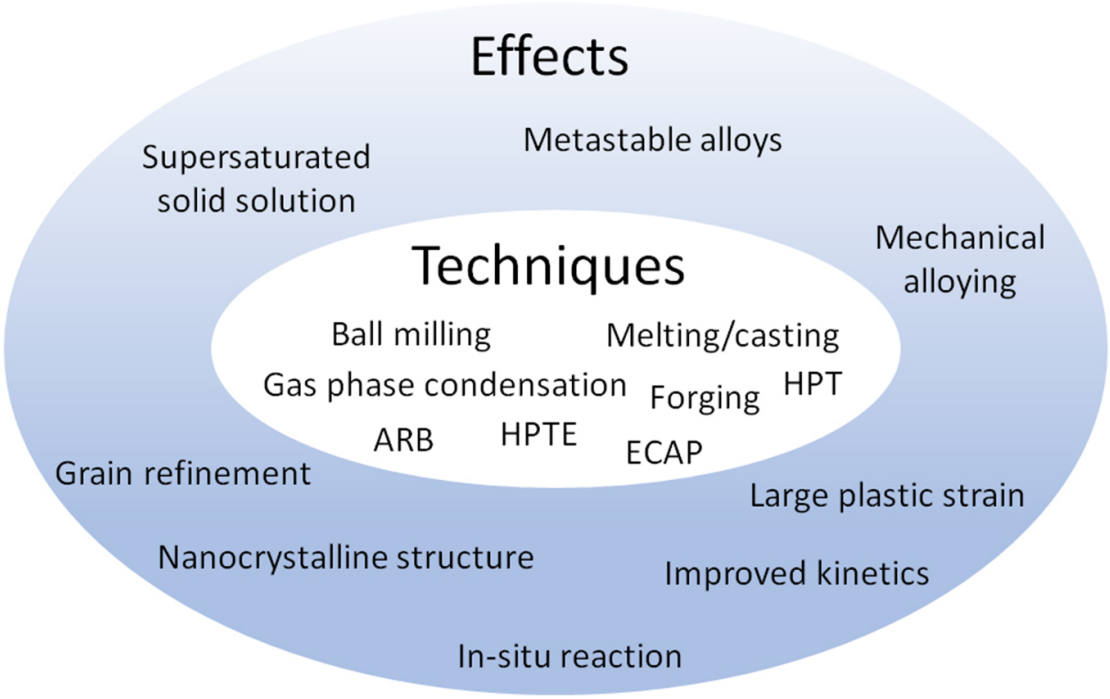

Figure 6. Materials processing methods considered in this section and their effect on the microstructure and properties of the synthesized alloys.

synthesis can be performed under inert or reactive atmosphere, at elevated gas pressures, using high-energy impact between reacting compounds, with a solvent, or at cryogenic temperatures. In the process of ball milling the mechanical action of repeated fracture and welding of elemental particles forces interdiffusion between the components. Diffusion is enhanced by the decreased particle size, increased defect density and a local rise in temperature. Ball milling can achieve supersaturated solid solutions, even for immiscible systems with a positive heat of mixing that have no solid solubility under equilibrium conditions [81]. The extension of solid solubility depends on milling time and intensity, as well as on other parameters such as milling temperature [82] and use of process control agent [83].

Mechanochemistry is widely used to modify and synthesize stable and metastable metal hydrides and allowed significant advances in the variety of their compositions and structures [84]. Typically, the material is processed under an inert atmosphere such as argon. This is necessary because the high energy of milling will induces formation of oxides and hydroxides in the presence of air. This will deteriorate the H storage properties (capacity, kinetics), particularly for nanostructured materials [85]. Because the crucible is closed, the amount of oxygen inside it is small. Once this oxygen reacted, there is no further oxidation of the material processed and the deleterious effect inside the crucible is limited [86]. Nevertheless, milling must be performed in an inert oxygen-free atmosphere.

Because milling is a quite energetic process, one can take advantage of this to stimulate a chemical reaction. For formation of metal hydrides, this means milling under high hydrogen pressure. This is another versatile method to obtain both stable and metastable hydrides. Here, the pressure and temperature can be measured in real time during milling, allowing H sorption and exothermic reactions to be followed. A significant improvement in the ability to characterize the reaction paths while milling can be achieved by combining mechanochemical synthesis with synchrotron x-ray powder diffraction, as was recently demonstrated. Improvements in the design and material of the jar during the last decade reduce background impurities from the jar and cause sharpening of the Bragg peaks from the powder under investigation.

3.2. Severe plastic deformation (SPD)

SPD was originally developed for producing ultrafine grain metals and alloys by introducing large plastic strain in the workpiece while preserving its mechanical integrity and overall dimensions. The plastic strains achievable in SPD are normally much higher than in conventional cold- and hot-working techniques such as rolling or forging. Major SPD techniques that have been utilized to improve H storage properties of hydride-forming alloys include equal channel angular pressing (ECAP), high-pressure torsion (HPT), and accumulative roll bonding (ARB) [87]. In the ECAP method, a metal billet is extruded through the bent

channel, and the process is repeated several times with or without rotation of the billet between consecutive passes. In the HPT method, a thin metal coupon is placed between high-pressure anvils and is deformed in torsion under simultaneously applied high compressive load (usually in the GPa range). The HPT process usually results in more significant grain refinement than its ECAP counterpart, yet it is limited to thin samples and is less suited for industrial upscaling. Recently, a novel technique resembling the HPT but eliminating its main disadvantage of small sample dimensions has been proposed: the high pressure torsion extrusion (HPTE) [88]. The HPTE technique is based on extruding the metal billet through a die consisting of two tightly fitted cylindrical containers that can revolve relative to each other. The extruded material undergoes a simultaneous shear (extrusion) and twist (container rotation) deformation, and is subjected to a hydrostatic pressure generated by the narrowing of the extrusion channel. The potential of the HPTE method to enhance the kinetics of hydride-forming metals has been recently demonstrated [89]. Finally, in the ARB method the conventional rolling is followed by folding of the rolled piece and the rolling-folding cycle is repeated again and again, so that significant plastic strain can be introduced in the sample with minimal thickness reduction. The ARB process results in significant grain refinement, yet the samples exhibit typical rolling texture and anisotropic microstructure and impurities can be trapped in the material upon folding. The advantage of this method is its relative simplicity and the possibility of industrial upscaling.

It should be noted that bulk metallic pieces processed by SPD must be further dispersed before performing hydriding test. The usual techniques include lathe machining, manual filing, and high-energy ball milling. These final dispersion steps introduce additional plastic strain into the material that is difficult to quantify and that assuredly induces further changes in the microstructure. For example, it has been shown that conventional lathe machining causes grain refinement and increased hardness in metallic chips comparable to that of other SPD techniques [90].

Originally, the SPD-based nanostructuring techniques were developed in the field of structural materials with the aim of producing bulk ultrafine grain and nanocrystalline materials with improved mechanical properties. Preserving the overall dimensions of the processed piece is less of a concern in H storage applications and thus more conventional cold working techniques such as rolling can be also employed for improving the hydriding kinetics [91]. Finally, all SPD techniques mentioned above can be employed not only for the processing of bulk metal billets, but also of the hydride powders. The intrinsic brittleness of metal hydrides prevents their full densification; consequently, the processed samples can be directly tested for H desorption/adsorption.

3.3. Forging

Widely used for centuries in metallurgical manufacturing, forging is an alternative to SPD processes. It consists of applying a significant compressive force to a piece of metal, either cold or hot, to modify its mechanical properties and/or give it a particular shape. The plastic deformation induces a refinement of the microstructure as well as a certain degree of texture of the metal. During forging, mechanical energy is transformed into heat, which allows, in some cases, to stabilize metastable phases.

Forging was recently used to improve the properties of magnesium-based metal hydrides [92, 93]. The applied process consists of dropping a hammer of several tens of kilograms from a given height, either on a closed-die where the material is confined, or using a flat open-die, which allows the metal to flow under the impact of the stress.

Close-die forging was first applied at room temperature (RT) in air using MgH_2 powders [92]. The impact of parameters such as the height of the hammer, the number of forging passes, and the sample thickness were studied. A pronounced grain refinement was obtained at higher energy processing (higher height of the hammer and ten forging passes). This cold forging process leads to sorption kinetics similar to those observed on MgH_2 powders processed by cold rolling or HPT. For a larger number of forging passes, a partial oxidation of the sample occurred during the process, so that thicker samples, less sensitive to oxidation, exhibit better properties.

Open-die forging was applied to pure Mg or Mg–Ni eutectic composition using a single pass at temperatures up to 530 °C [93]. Samples, either as-cast cylinders or compacts prepared by uniaxial compaction of powders, were introduced into a thin stainless-steel tube to prevent their dispersion during forging, then placed in a chamber under an argon atmosphere, where they were heated using a high-frequency inductor. This U-shaped inductor, mounted on a sliding arm, was removed at the last moment to avoid damage during forging. The H sorption properties depend significantly on the forging temperature through the induced microstructures. Below the brittle-ductile transition of magnesium (225 °C–250 °C) the forging process leads to a pronounced fibre texture and to internal strain that promotes the diffusion of H through the bulk material, whereas forging above 400 °C induces the formation of the intermetallic compound Mg_2Ni. After optimization of the forging process, Mg–Ni bulk materials with good reactivity already after the first H absorption were obtained.

Compared to mechanical milling, which leads to highly pyrophoric powders, forging is a simpler and less time- and energy-consuming process that provides a safe and cost-efficient way to produce bulk H storage materials at large scale.

3.4. Melting and casting

Arc button, plasma or vacuum arc, and induction melting are used to prepare intermetallic alloys. Arc button melting is suitable for laboratory samples up to a few tens of gram with high concentration of reactive TMs. Vacuum arc melting (VAM) has been applied to produce 227 kg of TiFe alloy [94] and much larger VAM furnaces are commercially available. These use an inert gas atmosphere such as Ar or He inside a vacuum chamber and have a water-cooled cold hearth, which yields clean as-cast alloys. Induction melting, on the other hand, can be done either in air with protective gas or under vacuum, depending on the alloy composition. For example, Mg–Ni eutectic alloys can be produced by induction melting in air under a protective mixture of SF_6 and CO_2 gas [95]. However, most intermetallic alloys, including AB_5, AB_2, AB, are normally produced by vacuum induction melting. Once the charge becomes melted and homogenized by an inherent stirring motion, ingots can be made by pouring the melt into a mould usually made of steel coated with mould-releasing agent. A 400 kg ingot of TiFe alloy was successfully produced in an air induction furnace using a clay graphite crucible and mischmetal as deoxidant [94].

3.5. Gas phase condensation of nanoparticles (NPs)

As discussed above, SPD and ball milling produce materials with ultrafine-grained microstructure and improved H sorption properties. However, the outer size of the processed powders or metal pieces is typically well beyond the nanoscale. On the other hand, the synthesis of hydrides NPs with a diameter between 5 and 50 nm is interesting for two reasons. First, the possibility exists to carry out fundamental studies of nanoscale effects, such as surface energetics and elastic confinement, on H sorption behaviour. Second, the potential exists to achieve the ultimate sorption kinetics, because H diffusion must take place over a very short distance of few nanometres that separates the NP core from its surface. This aspect is particularly appealing in the case of Mg and thus it is no surprise that many strategies have been developed to synthesize MgH_2-based NPs, resulting in different materials architectures. For example, impregnation with dibutylmagnesium ($MgBu_2$) or infiltration with molten Mg of porous materials, followed by hydriding, were employed to produce MgH_2 NPs supported on a scaffold [96]. The reduction of an organometallic precursor in the presence of a polymeric capping ligand was able to provide Mg NPs embedded in a gas-selective polymer [97]. Alternatively, gas-phase condensation (GPC) is a bottom-up method that yields freestanding NPs without the ballast of a porous host or embedding matrix. GPC relies on the production of atomic vapours within a cooling gas that leads to supersaturation and homogeneous nucleation of NPs. Vapours are typically generated by thermal evaporation, arc discharge or magnetron sputtering, and the cooling gas is usually He or a He/H_2 mixture. Although GPC of elemental Mg under pure conditions results in large particles with characteristic hexagonal habit and average size above 100 nm [98], NPs with a much smaller size of 10–20 nm can be obtained by co-evaporation of Mg and another metal such as Ti [99]. This suggests that, in the case of mixed vapours, the coarsening of NPs by mutual coalescence is significantly hindered, i.e. the added element acts as a particle growth inhibitor. Therefore, such a strategy offers a double advantage, because both the stabilization of NPs to a smaller size and the incorporation of a H_2 dissociation catalyst can be achieved in a single fabrication step. Even if the mixed vapours are immiscible in the solid state, as for Mg and Ti, GPC can yield metastable alloy NPs [99], in analogy with metastable alloys produced by ball milling. The metastable NPs readily decompose upon H sorption leading to an interesting composite morphology, where TiH_2 clusters are embedded in Mg or MgH_2 NPs [100]. By tuning the individual vapour production rates, the composition of the NPs can be adjusted to optimize the reversible H storage capacity while maintaining outstanding kinetics [101].

4. Hydrogen storage in Mg-based hydrides

4.1. State of the art and issues to be solved

The alkaline earth element Mg is unique among metals, being on the border between metals that form dominantly covalent hydrides, as observed for beryllium (Be), and metals that form ionic hydrides, such as calcium (Ca). In fact, H forms covalent bonds with Be and aluminium (Al) forming polymeric solids, whereas the bonding with Mg shows a mixed ionic-covalent nature, with a prevalence of the former. Magnesium hydride, MgH_2, adopts the rutile (TiO_2) structure with a directional Mg–H bonding. However, Mg does not show the ability to form coordination complexes such as Be and Al forming tetrahydridoberyllate BeH_4^- and tetrahydridoaluminate AlH_4^- ions. In addition to the rutile-type phase, MgH_2 forms two other polymorphs [4], which are only stable at very high pressures and are not relevant to

Table 1. Properties of MgH_2 and Mg compared to selected metals and their ionic hydrides: molar mass M of the hydride, density ρ, melting point of the metal T_{mp}, decomposition temperature T_{dec} of the hydride at 1 bar, gravimetric H density ρ_m.

	M (g mol^{-1})	ρ_{hyd} (g cm^{-3})	ρ_{met} (g cm^{-3})	T_{mp} (°C)	T_{dec} (°C)	ρ_m (wt.% H)
MgH_2	26.32	1.45	1.74	650	283	7.6
LiH	7.95	0.769	0.535	181	720	12.7
NaH	24.00	1.36	0.971	98	420	4.2
KH	40.11	1.43	0.862	63	417	2.5
CaH_2	42.10	1.7	1.54	842	600	4.8

practical H storage. After synthesis by non-equilibrium methods such as ball milling, they exist in metastable conditions, but disappear after just one cycle of H release and uptake.

In contrast, the heavier alkaline earth metals, Ca to Ba, all form hydrides with the fluorite or lead (II) dichloride type structures. These hydrides have high lattice energies, high decomposition temperatures and conduct electricity in the molten state, which confirms their ionic character. The coordination number for the hydride ion, H^-, in these hydrides is in the range four to six, whereas it is only three for H^- in MgH_2.

Magnesium is among the lightest and most abundant elements, and is plentiful in seawater. Furthermore, magnesium and its oxide are also non-toxic and environmentally friendly, which makes Mg as well suitable for large-scale energy storage purposes.

Table 1 compares the properties of MgH_2 with those of selected ionic hydrides formed by alkaline and alkaline earth metals. The two hydrides of lighter metals, MgH_2 and LiH, have relatively high gravimetric densities, $\rho_m = 7.6$ and 12.7 wt.% H, respectively. Unfortunately, these hydrides are rather stable and have high decomposition temperatures T_{dec} (1 bar) = 283 °C and 720 °C, due to their high decomposition enthalpies $\Delta H_{dec} = 74$ and 91 kJ mol^{-1} H_2. Furthermore, because of the relatively low enthalpy of evaporation of the metals, $\Delta H_{vap} = 127.6$ and 147.7 kJ mol^{-1} [8, 102], Mg and Li are prone to sublimation when the hydride decomposes.

The high stability of ionic hydrides, while being a drawback for H storage, becomes extremely useful for heat storage in solar thermal power technology [103–105]. In fact, as explained in section 1.1, by changing $p(H_2)$ or T a metal can be forced to absorb H and release heat, whereas the hydride releases H when absorbing heat. Thus, an efficient heat exchange for H release and uptake will allow to store solar energy and make it available during the night [30, 103, 106].

In addition, Mg has recently attracted attention as a potential alternative to Li battery electrode material. This is due to both the high abundance of Mg and to its lower tendency to form dendrites, reducing the risk of dangerous internal battery shorting as compared to Li-ion batteries [4, 107].

Besides unfavourable thermodynamics, the Mg–MgH_2 system also suffers from sluggish H sorption kinetics. Several models have been used to describe the kinetics [108, 109], in particular the Jander model for absorption [110] and the JMAK nucleation and growth for desorption [111]. This suggests that the rate limiting steps for H absorption and desorption are the diffusion of atomic H through the formed layer of MgH_2 and the nucleation and growth of Mg in bulk MgH_2, respectively. In the later stages after the formation of Mg nuclei, the transformation can become rate-limited by associative desorption at the metal surface [65]. During hydride formation, the outer MgH_2 layer not only blocks the reaction, leading to the slowing down of the rate of H absorption [5, 112], but also shields the interior parts of the particles, so that the quantity of metallic Mg can be underestimated by XRD or electron microscopy observations. To overcome this issue, a realistic observation of the cross section of the particles and/or accurate thermogravimetric/volumetric H_2 absorption data are required [113].

Various synthesis and processing methods that have been developed for the preparation of Mg-based hydrides are reviewed in section 3. In order to improve the hydriding performance, it is important to produce a refined microstructure that accelerates H diffusion and promotes heterogeneous nucleation of the hydride or metal phase. At the same time, several additive phases, which can be incorporated during the synthesis, proved to be effective in improving the H sorption kinetics, as is discussed in section 4.3. As an example, small amounts of TMs and their oxides, proved to be very effective in enhancing the kinetics of H sorption [114–120]. In particular, studies using *in-situ* x-ray synchrotron powder diffraction at variable $p(H_2)$ and T have revealed the mechanism of chemical reactions between Mg/MgH_2 and the additives. Therefore, although the improvement of H sorption kinetics after introducing additives is often assigned to their catalytic effect, in many cases a chemical reaction among the components in the composite sample may happen and the real catalyst is a product of the reaction between Mg/MgH_2 and the additive, identification of which is often a challenge.

Thermal treatment of metal hydrides may also result in a phase segregation, recrystallization, and NPs agglomeration [121, 122]. There are various ways to overcome these issues by applying non thermal (and

non-straightforward) methods [123]. In fact, electrochemical methods were routinely used during the last decade, but new methods are now being explored, such as electromagnetic radiation (microwave, UV, visible light), mechanical forces, sonication, electric voltage, and electron beam mediated desorption. These methods offer a new landscape for altering the hydride formation/decomposition routes. For instance, the tribochemical decomposition of MgH_2 is able to release H_2 locally at RT, suggesting that novel reaction pathways may exist [124]. The thermoplasmonic effect can also be exploited to release H_2 using visible light [125]. Such unusual approaches are worth exploring, since they could boost the next generation of hydride materials to be used not only as H storage media but also for H-based energy conversion applications.

4.2. Mg-based alloys and compounds

4.2.1. Mg alloys processed by severe plastic deformation (SPD)

Since the pioneering work of Skripnyuk *et al* [126] SPD methods have been widely employed for improving H storage properties of Mg-based alloys. A short review of the efforts in this field until the year 2018 was recently published by Rabkin *et al* [127]. In this respect, it should be noted that all attempts to improve the thermodynamics of hydriding with the aid of SPD were inconclusive. Indeed, the holy grail of improving H storage properties of the Mg-based alloys is significantly decreasing T_{dec} of MgH_2. To accomplish this, the formation enthalpy of MgH_2 should be significantly reduced. The effect of nanostructuring on the reaction enthalpy was considered by Berube *et al* [128]. For the enthalpy ΔH_r to decrease, the increase of internal energy of the metallic phase due to nano-structuring by SPD (i.e. due to the newly created grain boundaries and dislocations) should be accompanied by its larger increase for the same reason in the hydride phase. The change $\delta\Delta H_r$ in the reaction enthalpy can be estimated by assuming that all grain boundaries in metallic Mg are inherited by the hydride phase, and then reversibly reappear after H_2 is desorbed:

$$\delta\Delta H_r = 3V_{Mg}\Delta\gamma_b/d \tag{7}$$

where V_{Mg}, $\Delta\gamma_b$ and d are the molar volume of Mg, the difference in energy of large-angle grain boundaries in MgH_2 and in metallic Mg, and the grain size in the SPD-processed metallic Mg. In deriving of equation (7), a simple assumption of a polycrystal with cuboidal grains was made and elastic energy associated with the stored dislocations was neglected. The energy of random large-angle grain boundaries in Mg and MgH_2 can be estimated as one-third of their surface energies γ_s ($\gamma_s = 0.55$ J m^{-2} for metallic Mg and 2.08 J m^{-2} for MgH_2 [128]). We will accept $d = 20$ nm as a lower limit of grain refinement by SPD. With these data, equation (7) predicts $\delta\Delta H_r \approx 1.1$ kJ mol^{-1} H_2, which is negligible compared to ΔH_r. Such change can cause a decrease of dehydriding temperature of MgH_2 of only a few degrees. However, the SPD of Mg alloys can effectively reduce or eliminate the pressure hysteresis, as demonstrated by Skripnyuk *et al* [126].

It should be noted that discussion above refers only to the two-phase Mg–MgH_2 equilibrium and does not include the possibility of formation of new metastable phases induced by SPD. A recent promising example of such a possibility is the work by Edalati *et al* reporting the synthesis of a Mg_4NiPd compound with the aid of HPT [129]. This highly homogeneous ternary phase with a B2 structure absorbed and desorbed H at RT. It remains to be seen, however, whether this approach will lead to the synthesis of novel game-changing Mg-based compounds capable of absorbing significantly more than 2 wt.% of H when operating close to RT.

In a number of recent works, an appreciable acceleration of H sorption kinetics in the SPD-processed Mg and Mg-based alloys has been reported [127, 130–133]. The SPD process can accelerate the hydriding kinetics due to the several enhancement factors: (a) increased density of grain boundaries and dislocations serving as fast diffusion paths for H; (b) superior nucleation rate of the hydride phase (during hydriding) or metal phase (during dehydriding) due to heterogeneous nucleation on defects; (c) high activity of the defect surface sites (i.e. the triple lines at the free surface) in dissociation of H_2, and (d) increased density of defects in the Mg oxide layer favouring H penetration in metallic Mg. The reports indicating shortened activation time of SPD-processed Mg alloys indicate that the last mechanism may be at work [134]. Unfortunately, no detailed study of the mechanisms responsible for accelerated hydriding of SPD-processed alloys has been performed so far, so that at present it cannot be claimed with certainty which of the above listed mechanisms is the leading one. We hope that this review will stimulate further research efforts in this direction.

4.2.2. Forged Mg-based alloys

Forging offers an alternative to SPD processes in nanostructuring of the alloys. It allows for a mass production, is energy efficient and avoids the handling of pyrophoric powders. Recently applied to various magnesium-based compounds [93, 135], the forging process appears to be efficient since the very first cycles when applied at RT or below the ductile-to-brittle temperature of transition of Mg (≈220 °C), which favours texturing magnesium along the *c*-axis of the unit cell of Mg and induces a large amount of structural defects.

When starting from the compacted MgH_2 powder, this leads to very a fast H absorption from the first cycle at 360 °C—20 bar, whereas starting with pure magnesium powder leads to moderate sorption kinetics even after three cycles when studied at the same experimental conditions. Starting from the eutectic Mg–Ni alloy shows that the impact of the forging process on the activation step also strongly depends on its initial microstructure. A sample consisting of compacted Mg + Ni powders annealed to form the Mg_2Ni phase before forging leads to the remarkable properties from the first cycle, both on absorption and desorption, whereas a raw Mg–Ni ingot of the same composition shows a very poor activation.

4.2.3. Mg/Mg_2Ni eutectic alloys

The Mg/Mg_2Ni eutectic alloys prepared by conventional melting and casting process have a typical lamellar eutectic microstructure with either primary Mg or Mg_2Ni depending on Ni content. The Mg_2Ni lamellae are typically less than one micron in width and about a few microns in length. For H storage alloys, Ni content has to be controlled in such a way that the alloys have fast enough sorption kinetics while maintaining the H storage capacity as high as possible. The existence of Mg_2Ni in Mg/Mg_2Ni eutectic alloys improves both absorption and desorption kinetics by activating the sorption process of Mg/MgH_2. There is no need of applying additional mechanical activation processes or adding catalysts to obtain such an improvement. During a simple activation cycle the alloy chips fragment, with a large volume expansion due to the formation of hydrides. The reaction kinetics of fully activated alloys become faster; for instance, absorption requires less than 10 min at 325 °C under 20 bar H_2.

It has been found [95] that both absorption and desorption in Mg/Mg_2Ni eutectic alloys proceed via a 3D diffusion-controlled mechanism regardless of Ni content. The higher the Ni content, the faster the reaction kinetics for both absorption and desorption processes. However, the apparent activation energy of 143 kJ mol^{-1} for the desorption process did not change with Ni content. Under the given temperature, H_2 partial pressure, and reaction time condition, the effective H storage capacity is much higher with eutectic and hyper-eutectic compared with hypo-eutectic composition. Moreover, the results of long-term cycling test show that the storage capacity of both the eutectic and hypo-eutectic alloys remains stable between 93% and 95% of the initial value after 100 cycles.

Concerning the mechanism of H sorption in the eutectic alloys, it is worth noticing that H release from Mg_2NiH_4 to form $Mg_2NiH_{0.3}$ is over before the onset of MgH_2 decomposition [136]. Therefore, the catalyst effect of Mg_2Ni on MgH_2 formation and decomposition is based on fast diffusion of atomic H in $Mg_2NiH_{0.3}$, i.e. a solid solution of H in Mg_2Ni that facilitates H exchange in the Mg ↔ MgH_2 system [137]. *In situ* TEM studies unravelled the microscopic mechanism of H release from the single phase Mg_2NiH_4 [138].

4.2.4. REMgNi-based hydrides with layered structures

REMgNi-based hydrides have recently attracted much interest because their versatile crystallochemistry, based on layer intergrowth, leads to a rich chemistry that allows their thermodynamic properties to be tuned maintaining a good H storage capacity. They were primarily developed as anode materials for Ni–MH batteries, but nowadays are considered for storage purposes as well. The main research objective is to identify new compositions with improved resistance to corrosion in order to extend their cycle life. From the fundamental point of view, a better understanding of their physicochemical properties, the hydride formation paths and the corrosion mechanisms at their surface deserve further investigation.

These compounds are pseudo-binary alloys (RE,Mg)Ni_y ($y = 3, 3.5, 3.8$) composed by the intergrowth of $[A_2B_4]$ and $[AB_5]$ layers stacked along the *c*-axis [139]. The formula is then $n[AB_5] + m[A_2B_4]$, where *m* and *n* are the numbers of successive layers in a stacking block unit. For $m = 1$ and $n = 1, 2, 3$, the compounds (RE,Mg)Ni_3, (RE,Mg)$_2Ni_7$, and (RE,Mg)$_5Ni_{19}$ are formed, respectively. Each phase adopts two types of structures: hexagonal (2*H*, $P6_3/mmc$) and rhombohedral (3*R*, $R\bar{3}m$) depending on the stacking sequences of the constituting layers. Mg substitution for RE in the $[A_2B_4]$ layer is limited to half of the *A* sites ($[REMgB_4]$) except for RE = La, Pr and Nd in the (RE,Mg)Ni_3 intermetallics, for which a complete substitution is reported ($[RE_2B_4] \rightarrow [Mg_2B_4]$) [140]. This results in the $REMg_2Ni_9$ intermetallics that form hydrides at higher pressures (10–100 bar H_2) than RE_2MgNi_9 intermetallics (0.01–0.1 bar H_2) [141] with an uncommon distribution of H in the $[Mg_2Ni_4]$ layers [142] that differs significantly from the structure of the ternary hydride $MgNi_2D_3$ formed by the Laves type $MgNi_2$ intermetallic [143, 144].

The reversible H sorption properties of the quaternary system $A_{0.5}La_{1.1}Mg_{0.4}Ni_7$ (*A* = Sm, Gd and Y), which belongs to the family (RE,Mg)$_2Ni_7$, have been recently studied by Zhang *et al* [145]. These compounds exhibit better sorption properties for energy storage than their binary or ternary counterparts; the substitution of *A* by La and Mg leads to a single, large, stable and reversible plateau pressure suitable for

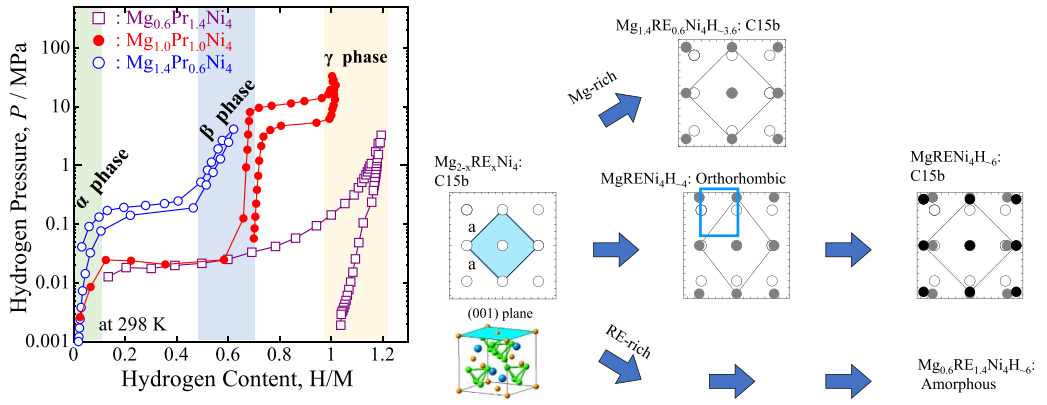

Figure 7. Isotherms of H absorption–desorption for $Mg_{2-x}Pr_xNi_4$ (left) and their phase transformation pathway upon hydriding (right).

energy storage applications. In particular, the compound $Sm_{0.5}La_{1.1}Mg_{0.4}Ni_7$ reached a reversible capacity equivalent to 400 mAh g^{-1}. Their behaviour can be anticipated from the volume matching of $[A_2B_4]$ and $[AB_5]$, linked to the substitution rates.

The role of Mg substitution was also explored comparing binary Sm_2Ni_7 and Sm_5Ni_{19} with pseudo-binary $(Sm,Mg)_2Ni_7$ and $(Sm,Mg)_5Ni_{19}$ [146]. Better stability was obtained for Mg-containing pseudo-binaries with $n = 3$, related to the higher strength/stability of the three stacked $[AB_5]$ units. Substitutions in the *A* or *B* sites are of major importance as this decreases the molar mass, reduces the number of plateaus, flattens the PCI curves, and controls the corrosion rates. Such fine adjustments lead to hydrides suitable for reversible H storage.

Another interesting example of composition-structure-properties relationships is provided by the layered 1/3 type $La_{3-x}Mg_xNi_9$ alloys ($x = 1.0$, 1.1 and 1.2). In these systems, the degree of La substitution by Mg allows the crystallographic characteristics and H storage properties to be tuned [147]. *In situ* studies of the phase-structural transformations in these alloys allow to define the heat treatment that leads to optimized properties based on the established transformations mechanism [147, 148].

4.2.5. Mg-based ternary $Mg_{2-x}RE_xNi_4$ compounds

$Mg_{2-x}RE_xNi_4$ is one of the constituent units for $Mg_{1-x}RE_xNi_3$ and $Mg_{2-x}RE_xNi_7$, making the hydriding properties and crystal structure of their hydride of interest. $Mg_{2-x}RE_xNi_4$ has a face-centred cubic (FCC) structure ($AuBe_5$ type) in the space group $F\bar{4}3m$ (No. 216), which is similar to a C15-type structure ($MgCu_2$ type) of a Laves phase alloy in the space group $Fd\bar{3}m$ (No. 227) [149–159]. Mg and RE atoms are ordered in the structures of $Mg_{2-x}RE_xNi_4$ but disordered in the structures of the Laves phase alloys.

$Mg_{2-x}Pr_xNi_4$ shows compositional dependence of hydride formation. As shown in figure 7, $Mg_{1.0}Pr_{1.0}Ni_4$ has two distinct plateaus of H absorption–desorption, indicating appearance of three hydride phases, including α, β, and γ phases, while Mg-rich $Mg_{1.4}Pr_{0.6}Ni_4$ shows a plateau only up to H/M = 0.5. On hydriding, the crystal structure of the metal sublattice remains cubic (C15b) or undergoes an orthorhombic deformation, as related to the ration RE/Mg in the alloys. A similar compositional dependence was also observed in other $Mg_{2-x}RE_xNi_4$ [157] except for Ce [155]. In addition, studies of $MgRETM_4$ (TM = Co, Cu) [159–161] showed a wide, sloping plateau for $MgRECo_4$ which exceeded H/M = 1.0, whereas $MgRECu_4$ compounds remained inert to hydriding. Thus, hydride formation in $Mg_{2-x}RE_xTM_4$ is affected by RE elements, RE/Mg ratio, and the type of the TM element.

As described above, three hydride phases appear during the hydriding reaction of stoichiometric $MgRENi_4$. In those hydrides, H atoms are located inside the $RENi_3$ tetrahedra and triangular bipyramids RE_2MgNi_2 (H atoms in the α phase have been reported to occupy a tetrahedral site Ni_4 [154]). Recently, the structure of the β phase hydride of $Mg_{2-x}Y_xNi_4$ was reported to contain a short H–H distance of less than 2.1 Å [151] similar to the γ hydride [158], although the H atomic pairs do not simultaneously exist at the neighbouring atomic sites. Such short H–H interatomic distances have been observed using a combination of neutron powder diffraction (NPD) and inelastic neutron scattering (INS) in (La/Ce/Nd)NiInH$_{1.3}$ [162, 163] and INS in the amorphous ZrV_2-based tetrahydride [164].

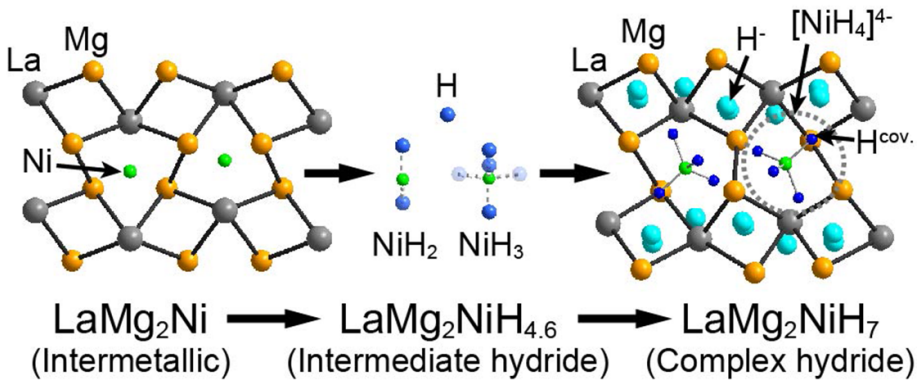

Figure 8. Local atomic arrangements during the H absorption reaction from intermetallic $LaMg_2Ni$ to the complex hydride $LaMg_2NiH_7$ through the intermediate hydride $LaMg_2NiH_{4.6}$.

4.2.6. $LaMg_2Ni$ intermetallic

The Mg-containing intermetallic compound $LaMg_2Ni$ forms the complex hydride $LaMg_2NiH_7$ composed of La^{3+}, $2 \times Mg^{2+}$, $[NiH_4]^{4-}$, and $3 \times H^-$ which contains both covalently bonded H (H^{cov}) and hydride ions (H^-), through an intermediate hydride $LaMg_2NiH_{4.6}$ [165–170] (figure 8). In $LaMg_2NiH_{4.6}$, H atoms around Ni atoms form NiH_2 or NiH_3 units, and the remaining H atoms are located inside tetrahedra coordinated by two La and Mg atoms. $LaMg_2NiH_{4.6}$ was suggested to be an intermediate hydride among complex hydrides, ionic hydrides and interstitial hydrides [167, 170] studied by NPD, INS, and computational modelling.

Hydrogen release reactions proceeding on a heating of $LaMg_2NiH_7$ were investigated by NPD and INS from 10 K to 600 K [170]. The results showed remarkable weakening of H^{cov} chemical bonding in $[NiH_4]^{4-}$ and increasing of H^{cov} atomic displacement factor at around 200 K, which was much lower than the H release temperature (∼600 K). Those facts might cause an easy H release reaction from $LaMg_2NiH_7$. Such phenomena have been also observed in an Al-based complex hydrides [171, 172]. The H absorption and desorption reactions of $LaMg_2Ni$ are partially reversible and maintain the metal atomic sublattice unchanged [170].

4.3. Catalyst development and performance

Achieving fast hydriding kinetics of bulk Mg powders requires use of nanostructuration and additives [173]. Many types of additives, such as metals, oxides, nitrides, fluorides, carbons and hydrides, have been used as promoters [115]. Their exact role in the hydriding reaction—likely depending on additive chemistry, location, and microstructure—remains unclear. Systematic studies on the efficiency and role of additives in hydriding kinetics are needed. We here review recent advances performed in Task 40 regarding catalytic effects promoted by early TM (ETM) hydrides, carbonaceous materials, Ni-graphene, and ferrovanadium (FeV) additives.

4.3.1. Early transition metal (ETM) hydrides

Since H diffusion in magnesium hydride is intrinsically slow, magnesium nanostructuring is required to shorten the diffusion paths and thereby enable faster reaction kinetics in the Mg–H system [174]. Moreover, due to the poor catalytic properties of Mg towards H chemisorption, the presence of active phases at the Mg surface is required for catalysing surface reactions [175]. An elegant route to achieve both nanostructuring and to modify the surface reactivity is one-pot mechanochemical reaction of Mg with *d*-block TMs under H_2 [176–178]. Indeed, while ETMs belonging to Ti and V-columns of the periodic table are immiscible with Mg, upon H absorption they easily form MgH_2 to $ETMH_x$ nanocomposites.

Within this context, Rizo-Acosta *et al* have undertaken a systematic and comprehensive experimental investigation of the kinetic and cycling properties of MgH_2–$ETMH_x$ nanocomposites with 5% mol of Y or ETM = Sc, Ti, Zr, V, Nb [179]. Isothermal kinetic studies under quasi-constant $p(H_2)$ demonstrate that, during desorption, all ETM hydrides but YH_3 behave as gates for Mg dehydriding by catalysing H_2 recombination. Moreover, absorption kinetics and structural assessments suggest the formation of coherent interfaces between ETM hydrides and MgH_2. Epitaxial effects would favour nucleation of MgH_2 as reveals the fact that ZrH_2, having the closest molar volume to MgH_2, induces the fastest absorption kinetics. Last but not least, ETM hydrides ensure good cycling stability of reversible H sorption in Mg at high rates by inhibiting Mg grain growth. For this property, TiH_2 turns to be the best additive, likely due to its closer molar volume to Mg. Consequently, among all studied ETM hydrides, TiH_2 provides the best trade-off

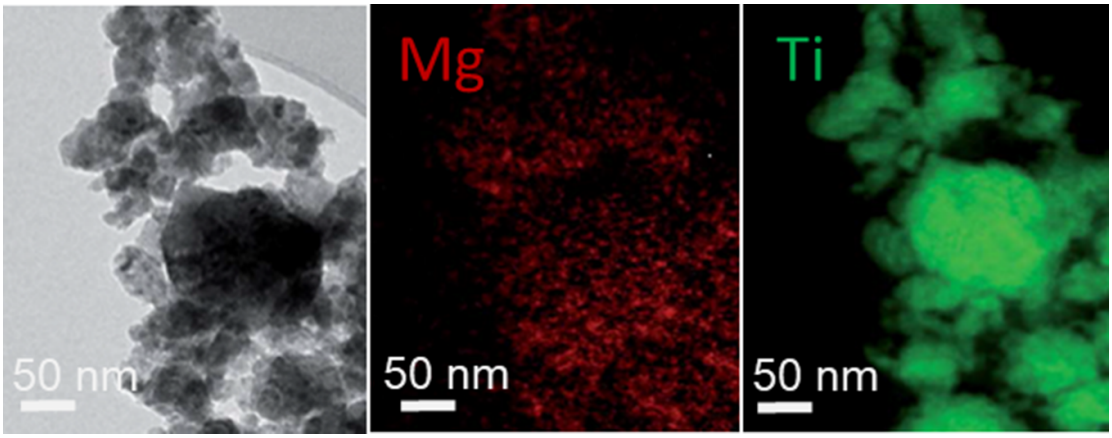

Figure 9. Elemental mapping of $Mg_{0.9}Ti_{0.1}$ + 5% C after 105 H sorption cycles. Left: morphology of the composite particles; middle: Mg mapping; right: Ti mapping.

between capacity and cycle-life properties enabling a reversible capacity of 4.8 wt.% at 573 K when passing through 20 sorption cycles during a reaction time intentionally limited to 15 min.

The cycle-life of ball-milled MgH_2–TiH_2 composites with a small Ti content can be further improved by adding a small amount of graphite [180]. In particular, the composition $(MgH_2)_{0.9}(TiH_2)_{0.1}$ with the addition of 5 wt.% C displayed a reversible storage capacity of about 5.8 wt.% H over 100 H sorption cycles. The modelling of H sorption kinetics explained the different behaviour of the Mg–Ti and Mg–Ti–C composites. It appears that H absorption proceeds via two overlapping processes, i.e. nucleation and growth ('fast' process) and H diffusion-controlled process ('slow' process). Their relative temperature-dependent impact was directly connected to the presence or absence of graphite and the number of absorption–desorption cycles.

For the graphite-containing composites, a significant decrease of the contribution of the 'slow' process of H diffusion to the H absorption takes place. TEM studies of the initial and cycled at $T = 350$ °C samples showed dramatic changes in the distribution of Mg and TiH_2, resulting in a segregation of TiH_2 for the non-optimized materials. Without graphite, the cycling results in the sintering/recrystallization of Mg, while in the presence of graphite it leads to a further refinement that yields a uniform distribution of Mg NPs and a surface covered by TiH_2 (see figure 9). In conclusion, the addition of carbon (5 wt.% graphite) to the MgH_2–TiH_2 nanostructured hydride composites maintains excellent H sorption performance, conferring prolonged stability during cycles at high temperatures in contrast to the composites not containing graphite [180].

4.3.2. Ferrovanadium (FeV) alloys

FeV alloys containing 80–85 wt.% V are commercial products of high demand and find applications in the metallurgy and automotive industry. FeV has a potential to become a cheaper and effective alternative to a pure vanadium in the development of the weight-efficient H storage materials based on the nanostructured magnesium hydride thus promoting applications of Mg–V based H storage materials.

Additives of FeV (∼80 wt.% V) improve H sorption performance of magnesium-based nanocomposites. This improvement includes facilitation of hydriding during the reactive ball milling in H_2 and causes faster dehydriding and re-hydriding kinetics. The most pronounced improvements were observed at a FeV concentration of about 10 wt.%. This ball milled composite showed an H storage capacity of about 7 wt.% H with both lowered activation energy of MgH_2 decomposition (60–80 kJ mol^{-1} H_2 vs 107–130 kJ mol^{-1} H_2) and shortened H_2 absorption time (by a factor of 10) compared to MgH_2 without additives [181].

FeV catalyst remained nanocrystalline under the cycling of H absorption–desorption at 350 °C, and its fine particles were uniformly distributed in the matrix of Mg or MgH_2. This is the likely origin of a relatively high cycle stability of the Mg–(FeV) composites exhibiting no loss of the H sorption performance during at least 30 cycles at 350 °C.

4.3.3. Nickel-graphene composites

Nanocomposites of graphene like material (GLM) and nickel containing 5–60 wt.% Ni when prepared by a co-reduction of graphite oxide and Ni^{2+} ions serve as effective catalysts for of Mg-based materials and show a high stability on cycling. Composites of MgH_2 with Ni/GLM prepared by high-energy ball milling under H contain Ni NPs having size of 2–5 nm uniformly distributed in the composites (figure 10) [182].

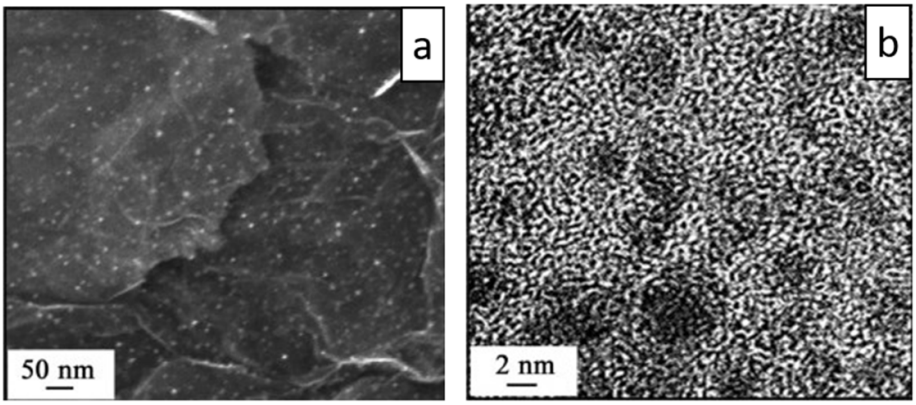

Figure 10. Scanning electron microscopy (a) and TEM (b) images of the Ni/GLM composite catalyst (5 wt.% Ni deposited on GLM). Reprinted from [182], Copyright (2019), with permission from Elsevier.

The composites of Mg with Ni/GLM have a high reversible H capacity exceeding 6.5 wt% H and also show high rates of H absorption and desorption thus belonging to the promising H storage materials. Adding GLM and Ni/GLM significantly improves both the kinetics of the formation of MgH_2 during the ball milling under H_2, and the sorption kinetics at elevated temperatures of the ball-milled material.

4.3.4. Carbon nanotubes (CNTs)

The beneficial effect of adding carbon and its various allotropes to hydride-forming alloys on their H storage properties has been documented in several studies [66, 183, 184]. For example, Mg and Mg-based alloys co-milled with various carbon allotropes (such as graphite, activated carbon, single- and multiwall CNTs, and graphene nanoplatelets) exhibit accelerated hydriding kinetics and shorter activation times. At the same time, it is now firmly established that at RT all known carbon allotropes absorb only insignificant amount of H (of an order of one-tenth of wt.% H) [185]. Also, carbon allotropes do not exhibit any noticeable catalytic activity in the classical, chemical sense, which means that they do not facilitate splitting the H_2 molecule into H atoms. Thus, the documented beneficial effect of carbonaceous additives on H sorption properties of metal hydrides requires an explanation. Lototskyy *et al* have proposed that co-milling of Mg with carbon allotropes result in a formation of a thin graphene-like layer on the surface of Mg NPs [66]. Such layers prevent MgH_2 particles agglomeration during the processing, reduce their oxidation rate, serve as accelerated diffusion paths for atomic H, and prevent grain coarsening of the metals during a repeated cycling, thus improving stability.

Among various carbon allotropes, the CNTs seem to exhibit the highest beneficial effect on H_2 absorption, and an extensive reference publications describe studies of catalytic activity of single- and multiwall CNTs (MWCNTs) in H_2 absorption by Mg and its alloys [186, 187]. However, the experimental conditions and the processing methods employed by different research groups vary so greatly that a meaningful comparison is hardly possible. Moreover, the CNTs exhibit poor adhesion to metals (and to Mg in particular) and a high tendency to agglomeration, so that ensuring their good and homogeneous intermixing with the metallic phase is a big challenge. Many groups have employed high energy ball milling to improve the intermixing between the CNTs and Mg-based alloys, yet the long milling times result in mechanical destruction of CNTs and their transformation into isolated fragments, carbon nano-onions, and amorphous carbon. Therefore, a careful microstructural characterization of the Mg-based alloy—CNT composite after the processing is imperative in the studies of the catalytic effect of CNTs on H sorption by Mg-based alloys. Such a characterization was performed in the works of Popilevsky *et al* focused on the studies of the H storage performance of as-processed and pelletized Mg–MWCNT composites [188, 189]. It was shown that the fastest absorption kinetics is achieved in the Mg-2 wt.% MWCNT composites after a high energy ball milling for 4 h. However, this improvement is not caused by the MWCNTs themselves, since they become largely destroyed by co-milling with Mg for 4 h. The microstructural studies demonstrated that such prolonged co-milling produces anisotropic, aligned chains of carbon NPs and nano-onions exhibiting excellent adhesion to the metallic Mg. During H absorption, such anisotropic initial microstructure remains anisotropic in the partially hydrided composite, ensuring high thermal conductivity and highly-developed metal–hydride interfaces in the composite, which promote a rapid metal to hydride transformation.

Recently, a synergistic effect of CNTs mixed with other known catalysts on H storage properties of Mg has been reported [190, 191]. Systematic efforts to study the catalytic effect of Pd-decorated MWCNTs of

different types and of other carbon allotropes (graphene nanoplatelets and activated carbon) on H sorption kinetics by Mg was undertaken by Ruse *et al* [192, 193]. It was shown that the highest improvement in the kinetics is obtained for MWCNTs with the lowest defects density. The results were interpreted in terms of H spillover phenomenon, suggesting that H_2 molecules dissociate on the Pd NPs attached to the MWCNTs, followed by a diffusion-controlled spreading of atomic H along the MWCNTs and its penetration into the Mg matrix. Thus, while not catalysing the H absorption reaction directly, the MWCNTs serve as H conductors increasing the number of the active sites at the MWCNT–Mg interface where atomic H can penetrate into metallic Mg and initiate the nucleation of the hydride phase. As an example, the total length of the triple contact line gas–Mg–Pd is about 31 nm for the hemispherical Pd NPs of 10 nm in diameter attached to a metallic Mg. The same Pd NPs attached to a 1 μm long MWCNT segment adhered to Mg can feed 2 μm of the gas–MWCNT–Mg triple line, which increases its catalytic activity by a factor of 70.

4.4. Mg-based nanoparticles (NPs) and thin films

4.4.1. Thermodynamics of nanoparticles (NPs)

An important question concerning H storage in metallic NPs is whether the thermodynamics of hydride formation experiences a significant change compared to coarse-grained materials. In principle, altered thermodynamics are expected because a significant fraction of atoms is located at free surfaces or at interfaces with other phases; the local change in bond energy upon H absorption at surface or interface sites may differ from that in the bulk-like crystalline sites, thus modifying the reaction enthalpy ΔH_r. This argument can be rationalized introducing the concept of interface (or surface) free energy change $\Delta\gamma$, illustrated in figure 11(a) and defined as:

$$\Delta\gamma = \gamma_{hyd} - \gamma_{met} \tag{8}$$

where γ_{hyd} (γ_{met}) is the excess free energy per unit area associated to interfaces (or surfaces) in the hydride (metallic) state. $\Delta\gamma$ is a generalization of the free energy change at grain boundaries $\Delta\gamma_b$ that appears in equation (7). In addition, one must account for the change in volume, and hence in surface/interface area, that occurs upon hydride formation. Calculations carried out for fine particles of elemental hydrides showed that ΔH_f becomes less negative for both MgH_2 and NaH, where $\gamma_{hyd} > \gamma_{met}$, the opposite being true for VH_2, TiH_2, AlH_3 and LiH [194]. Measurable effects, i.e. enthalpy changes larger than 2 kJ mol^{-1} H_2, were predicted only for very small Mg particles with diameter below 6 nm, which represent an experimental challenge in terms of synthesis, protection from oxidation, and stabilization against coarsening. It is not worth the effort to take such a challenge for a modest reward in terms of reaction enthalpy, of course. A more relevant enthalpy change may be expected if free surfaces are replaced by interfaces with other phases, a notable examples being the Mg|TiH_2 interface, because $\Delta\gamma$ becomes higher [195]. Therefore, an experimental journey into the world of nanohydrides appeared necessary to check theoretical predictions and to quantity the real thermodynamic changes that can be achieved.

The research by Paskevicius *et al* [9] was the first experimental evidence to show that the thermodynamic properties of magnesium hydride change with the particle size. In comparison to bulk MgH_2, the NPs of MgH_2 (≈7 nm) embedded in LiCl salt matrix showed a small but measurable decrease of about 2.8 kJ mol^{-1} H_2 in ΔH_r of decomposition, with a similar reduction of 3.8 J K^{-1} mol H_2 in ΔS_r. The thermodynamic changes in the MgH_2 NP system correspond to a drop of T_{dec} (1 bar) by only 6 K. This is not as large as predicted by the theoretical calculations due to the effect of the decrease in ΔS_r, which partially counteracts the decrease in ΔH_r. Further work on the melt infiltrating $LiBH_4$ into a porous Mg scaffold with a distribution of pores sizes ranging from 1.7 nm—macropore size resulted in a significant reduction of the H_2 desorption temperature for $LiBH_4$ of 250 K, when compared to the bulk [196].

The interface-induced destabilization of MgH_2 was later demonstrated by model experiments on Mg films embedded within TiH_2 layers [197]. The dependence of equilibrium pressure on film thickness, down to 2 nm, allowed for the determination of $\Delta\gamma = 0.33$ J m^{-2} at 363 K, in reasonable agreement with calculations. The separate contributions of enthalpy and entropy to $\Delta\gamma$ were not disentangled, although $\Delta\gamma$ was found to change significantly with temperature, indicating that interface entropy plays a role.

Recently, the two features of fine particle size and high density of Mg|TiH_2 interfaces were simultaneously realized by Patelli *et al* [100, 198], who synthesized MgH_2–TiH_2 composite NPs by GPC, as described in section 3.5. The equilibrium pressure, measured in the low-temperature range 323 K–423 K, increases with Ti content, attaining a four-fold increase in Ti-rich NPs compared to pure Mg. The analysis of van't Hoff plots suggests that, also in this case, a simultaneous reduction of both enthalpy and entropy takes place, leading to a partial enthalpy-entropy compensation. In turn, the effect on equilibrium properties is much smaller than expected on a purely enthalpic basis. The interfacial free energy change was estimated as $\Delta\gamma = 0.38$ J m^{-2} at 373 K, in excellent agreement with thin films data. In summary, experimental research shows that the

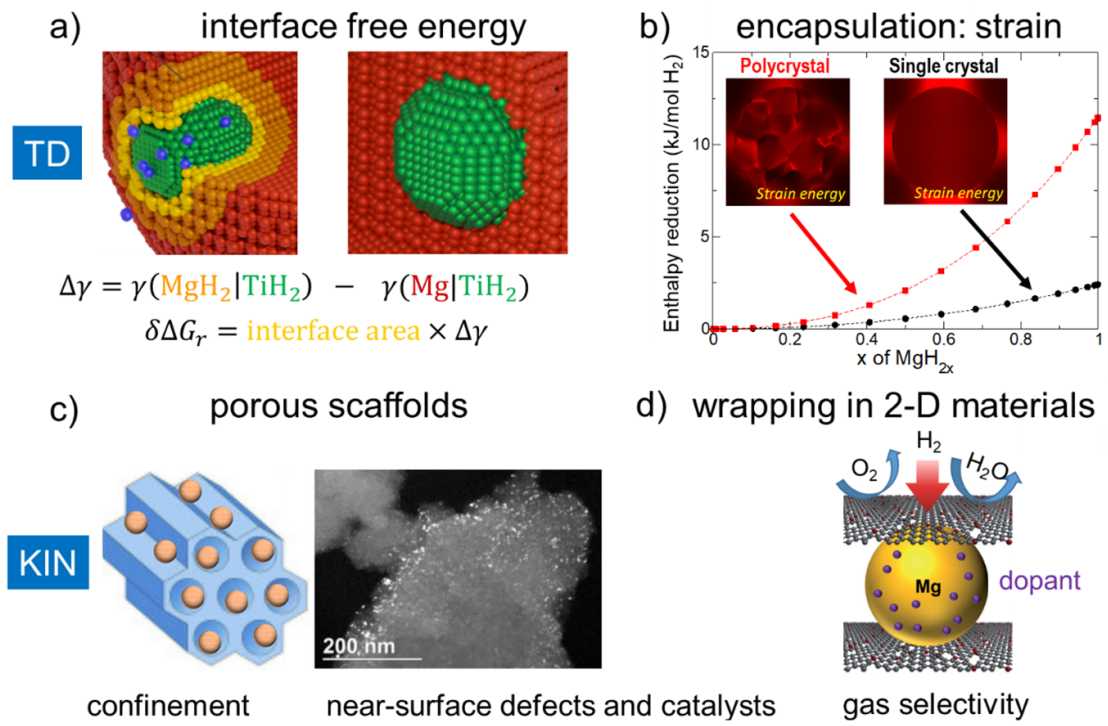

Figure 11. Schematic illustration of the main strategies to improve thermodynamics (top row) and kinetics (bottom row) of Mg-based nanostructures. (a) Thermodynamical bias δG_r associated with the free energy change at the interface between the active storage material and a second phase (TiH_2 in the figure); (b) predicted strain enthalpy contribution to the instantaneous thermodynamic driving force for hydride formation arising from stresses imposed by a confining host medium at each reaction stage. Insets show the corresponding relative von Mises stress distribution (red = high). Values are shown for single-crystal (black circles) and polycrystalline (red squares) Mg NPs encapsulated by carbon host under the assumption of fully elastic deformation; (c) confinement of Mg NPs in carbon-based porous scaffolds prevents sintering during cycling; (d) wrapping in graphene-like sheets provides gas selectivity enhancing resistance to oxidation. The addition of metal dopants such as Ni and Ti also enhances H sorption kinetics by a variety of mechanisms (see text for explanation).

reaction entropy changes with particle size, hence theoretical modelling calculations should no longer assume that the entropy can be kept constant. In this vein, theoretical models are being developed to directly compute entropy of surfaces using first-principles MD simulations, from which spatially dependent vibrational contributions in the interior and at surfaces of thin film models can be separated. Early results confirm that the entropy of certain surfaces is significantly enhanced with respect to the bulk due to the larger free volume and lessened constraint, which in turn leads to the enthalpy-entropy compensation [199].

An analogous yet alternative approach for modifying Mg–H thermodynamics involves confinement within a porous host. The confinement-induced mechanical stress exerted by the host upon volume expansion can then be leveraged to favourably alter the enthalpy [200]. Lawrence Livermore National Laboratory (LLNL) has been investigating the impact of Mg encapsulation on ΔH_r through a micromechanics modeling approach, introducing two factors for emulating more realistic conditions: (a) polygranular microstructure of the active material (Mg–H); and (b) mechanical boundary conditions corresponding to realistic hydride-host composite combinations. Figure 11(b) compares the modelling results for single-crystal versus polycrystalline Mg–H encapsulated by a carbon host as an example [199]. We point out that these initial models assume fully elastic deformation and adopt bulk values for elastic moduli, which results in significant quantitative overestimation of the effect of confinement on enthalpy. Nevertheless, qualitative comparisons can be made, for example as a function of grain structure. In particular, the polycrystalline sample results in a much larger confinement stress contribution to the reaction enthalpy effect. This is a consequence of the inhomogeneity of the stress field, which concentrates at junctions between certain grains to enhance the thermodynamic effect. Refinement of these modelling and analysis methods will guide optimization of the microstructural design of Mg composites for improved H storage performance.

Separately, progress has also been made in understanding the mechanics of Mg NPs at the atomic scale, which likewise has implications for assessing the contribution of elastic stress to reaction enthalpy changes at the nanoscale or under nanoconfinement. Kim *et al* reported a recipe for computing the bulk modulus of NPs, K_{nano} [23]. Although the original work focused on Pd, applying this same approach to Mg for 1–4 nm

NPs yields a bulk modulus K_{nano} of only 15–25 GPa, corresponding to 40%–66% of the bulk value. Among other consequences, this should reduce the expected quantitative effect of the confinement stress on reaction enthalpy (e.g. compared to the predictions in figure 11(b)). Similar predictions for MgH_2 NPs confined in various host materials are underway and can help to devise confinement strategies that can maximize the reduction of ΔH_r in Mg/MgH_2.

4.4.2. Kinetics of nanoparticles (NPs)

Beyond indications of possible modest alteration of thermodynamic equilibrium upon nanosizing due to confinement or interfacial effects, it has been definitively established that Mg-based NPs exhibit outstanding H sorption kinetics. This is particularly true if the refined morphology is accompanied by the addition of a catalyst phase of the type described in section 4.3. For example, the aforementioned MgH_2–TiH_2 NPs absorb H in about 10 min and release it in 120 min at 100 °C, with a reversible H capacity close to 5 wt.% for an optimized Ti content [101]. TiH_2 appears to act both as a catalyst for dissociation/recombination of H_2 and as a seed for heterogeneous nucleation of the hydride. Moreover, H diffusion is strongly accelerated along $Mg|TiH_2$ interfaces, as highlighted by recent studies in Mg thin films [201].

The main challenge with NPs is to maintain a high stability upon H cycling, which is only possible by suppressing oxidation and coarsening. One popular approach is confinement in carbon-based porous scaffolds such as aerogels, high surface area graphite, and carbon replicas of ordered mesoporous materials [96, 202], as illustrated in figure 11(c). Several synthesis routes produce MgH_2 NPs smaller than 5 nm that exhibit both fast H sorption kinetics and stability against sintering [203, 204]. Without a confining medium, high-surface area Mg NPs readily sinter upon cycling and their H sorption kinetics slow down considerably [96]. In this context, the recent claim that free MgH_2 NPs of 4–5 nm exhibit fast and stable kinetics with high capacity over 50 cycles at 423 K appears surprising, to say the least [205].

Clearly, the overall gravimetric storage capacity is significantly reduced by the weight of the scaffold. The quest for extreme lightness of the host medium has led to the use of 2D graphene-based layers to embed or wrap the NPs [206–208]. This approach can confer the additional advantage of protecting from oxidation by means of gas selectivity, because H_2 can penetrate the host while larger molecules such as O_2 and H_2O are blocked (see figure 11(d)). In the case of rGO, it was suggested that the formation of an atomically thin MgO layer at the surface favours H_2 dissociation, while the electronic interaction between Mg and rGO enhances interfacial binding, preventing agglomeration during cycles [206].

The incorporation of Ni dopants into rGO-encapsulated Mg NPs further enhances cycling performance. This was ascribed not only to the catalytic dissociation of H_2 by Ni, but also to the fact that nonstoichiometric Mg–Ni nanoalloys near the surface prevent the formation of thick MgH_2 layers, which are detrimental to H diffusion [207]. In other words, structural disorder effectively creates additional fast diffusion pathways for H transport through the H-rich surface layers during hydriding.

Finally, we notice that several terminating groups containing oxygen and/or nitrogen are possible at the edges of graphene sheets [186]. Although this rich landscape can lead to unintended side reactions, it may also provide new avenues to tune the (de)hydriding kinetics of Mg NPs via the interaction between Mg and functional groups, with concomitant creation of surface defects. This concept was explored recently using (bi)pyridine-N and ketone functional groups; however, the observed activation energies were about 90 kJ mol^{-1} for absorption and 140–180 kJ mol^{-1} for desorption [209], showing no significant changes compared to bulk Mg. Investigation of other terminating groups is needed in order to ascertain whether this strategy can be exploited to reduce the activation energies and boost the H sorption kinetics.

4.4.3. Thin films

Although thin films do not represent a viable solution for large scale H storage, they are an excellent platform to explore the influence of size [197], microstructure [210], elastic strains and alloying [211] on H sorption properties of Mg nanostructures. For instance, the morphology of Mg films can be tuned from flat to nanowire or nanoribbon by using glancing angle deposition. This technique allows an accurate control of length, width and tilt of the wires. It was observed that nanoribbon and nanotrees morphologies provide kinetics faster than flat films, suggesting an influence of crystalline orientation on H sorption [212–214].

The alloying of immiscible hydride-forming elements such as Mg and Ti in a thin film is of great interest both for applications and for structural studies of metastable alloys. Mg-rich $Mg_{1-x}Ti_x$ thin films exhibit interesting H-induced optical transition properties that can be applied to switchable smart coatings for solar collectors and hydrogen sensors [215, 216]. Conventional XRD methods suggest that these metastable thin films are solid solution alloys with a hexagonal close-packed (HCP) structure and transform into FCC hydrides upon hydriding [217]. However, the optical properties of the hydrogenated thin films are hardly explained by such simple structures and require a mixture of metallic TiH_2 NPs coherently embedded in a dielectric MgH_2 matrix [217]. Despite being extensively studied, this unique structure was not fully

determined. The reason is partly that the films are highly textured, exhibiting diffraction patterns with only few Bragg peaks. As an alternative, Kim *et al* [218] employed the atomic pair distribution function (PDF) technique [219], a local structural probing technique that gives the atomic probability distribution. The synchrotron x-ray PDFs of $Mg_{0.7}Ti_{0.3}$ thin films collected during hydriding unambiguously revealed the presence of TiH_2-particles of ∼3 nm in size. By combining this with the optical measurement results, it was estimated that ∼18% of Ti atoms in a TiH_2 NP are replaced by Mg. The Mg matrix, where TiH_2-NPs are embedded, is also transformed into FCC MgH_2, which differs from the rutile tetragonal structure of bulk MgH_2. Interestingly, in addition to FCC MgH_2, another MgH_2 phase with a face-centred tetragonal (FCT) structure appears. This phase is present throughout the transition and disappears when H uptake by the Mg matrix is completed. FCT MgH_2 seems to form between HCP Mg and FCC MgH_2 to reduce distortion energy caused by a lattice mismatch allowing this metastable thin film to retain its structure during transition and promoting its fast H uptake. There is very limited information about the atomic scale structure of immiscible hydride-forming alloy thin films and this example shows that PDF is a useful tool to extract their structural information.

5. Hydrogen storage in intermetallic alloys

5.1. State of the art and issues to be solved

Hydrogen storage in intermetallic compounds has been extensively investigated over the past 70 years [11] owing to their promising volumetric H capacity and reversible mild working conditions of temperature and pressure [220, 221]. For this reason, the characterization of intermetallic compounds can count on a vivid literature and many experimental and theoretical studies performed until now. Even prototype and modelling activities on intermetallic-based integrated H storage and energy systems have been widely explored [34].

Metal hydrides can achieve high-capacity storage at much lower pressures, allowing use of cost-efficient tank components. Because weight is comparatively unimportant for stationary storage, a broad range of materials can be considered. Indeed, several metal hydrides based on intermetallic compounds have long been studied as attractive candidates for stationary H storage applications [6, 222]. However, low cost is paramount for practical grid-scale storage, and many of these compounds feature elements that are not earth abundant.

Hydrogen storage by intermetallics is realized through the formation of hydride phases upon H absorption. The latter involves a crystal structure transition that must be characterized by suitable techniques, including conjoint x-ray and neutron diffraction methods, to determine crystallographic properties of the metal sub-lattice as well as H location.

Intermetallics for H storage can be classified in three main groups: AB_5, AB_2 and AB. AB_5 compounds were tested for H storage back in the 1970s [223], and they include lanthanide RE elements at the A site, and late TMs such as Fe, Co, Ni and Cu at the B site. They show high reversible capacities, good cyclability, good kinetics and resistance to impurities, together with fast activation. Their main drawback is that, upon cycling, they can disproportionate to form the constitutive elements. In addition, they are frequently based on RE materials which are critical raw materials [224, 225]. AB_2 compounds include A = Zr, Ti, Y, La and B = V, Cr, Mn, Fe, Ni and show good volumetric H capacities, fast formation/decomposition kinetics and easy activation. However, since the main elements included in their formulation are expensive, they exhibit high production costs. They also show lower resistance to impurities and lower structural stability as compared to AB_5 compounds. Finally, AB compounds were the first to be discovered and tested for H storage as early as 1958 [11]. They are primarily based on A = Ti, Zr and B = Fe, Co and Ni and are interesting for practical applications because of the low cost (Co being the exception) and limited amounts of critical raw materials. They can store H near ambient pressure and temperature while retaining good kinetics and capacities. The main drawbacks are related to harsh activation conditions, sensitivity to poisoning, and the possibility of multiple hydriding steps that may limit their capacity in a narrow pressure range.

5.2. TiFe-based alloys

Among available intermetallic compounds, TiFe-compound is known as a promising candidate as H storage material, especially for fuel cell applications and on-site stationary storage [226] because of its low materials cost, earth abundance, possibility to absorb H at ambient temperature and low pressure, and reasonable gravimetric H storage capacity up to 1.9 wt.%. In fact, TiFe-based intermetallic compounds for large scale stationary applications have been recently investigated experimentally both in Europe and Japan [226–230].

Although the later stages of H uptake are rather facile, TiFe is known to suffer from difficult initial activation for hydriding, requiring high temperatures and pressures (∼400 °C and ∼50 bar, respectively) [231] as well as long incubation times (∼10 h). Cycle life is also limited, plagued by irreversible H uptake.

The incubation time and poor reversibility are thought to originate from specific properties of the surface passivating layer, which covers industrially produced TiFe powder. The TiFe surface is strongly reactive to oxygen, forming surface oxides and accompanying precipitates, with a composition and microstructure that depend on processing temperature and oxygen partial pressure. To overcome limitations associated with the passivating oxide, an initial activation treatment is generally invoked. This treatment usually consists of two steps [14]: (a) a procedure to circumvent the passivating layer for improved H absorption, which is often a thermal treatment that aims at removing surface oxide; and (b) cyclic H sorption at elevated temperatures and $p(H_2)$ to create fresh TiFe surface induced by cracking of passivating layers [232–236]. This elaborate and energy-intensive activation procedure is one of the main drawbacks in the preparation and practical use of TiFe.

Many efforts have been made to improve the initial activation of TiFe or to develop synthesis methods for TiFe-based materials that do not require an activation process. The most common way is to exploit the compositional flexibility of TiFe-based materials, which permits tailoring via partial substitution of the constituent elements of TiFe with a third TM (i.e. Mn, Ni, Co, Al, V, Pd, Cr, and Zr) or the addition of further elements [231, 237–248]. These foreign elements can affect both thermodynamics and kinetics. Substituents can modify hydride phase stability or influence the formation of secondary phases according to equilibrium phase diagrams. The formation of secondary phases as precipitates at the grain boundaries, if reactive to H, can also aid activation to allow initial hydriding of the material at moderate temperatures and pressures. Elemental segregation to grain boundaries or secondary phases can also promote diffusion kinetics to aid penetration of H into the bulk. However, elemental substitution can also lead to a loss of maximum storage capacity, particularly for the substitution of Fe with Al and Ni [244, 245]. Likewise, secondary phases usually have poor H reversible uptake, so their amount should be minimized to prevent penalizing the capacity of the material.

There are several concrete examples of elemental substitutions in TiFe intermetallic compound that have significantly changed activation processes and H storage properties [249]. Activation, kinetics, thermodynamics, cycling and resistance to poisoning properties can be optimised by chemical substitution, with particularly remarkable results for Mn and V. Indeed, substitutions in TiFe intermetallic compound guarantee a wide range of operational working conditions that can be tailored to individual system demands by rational design of Ti or Fe substitution, as evidenced recently in a comprehensive review [249]. Other recent studies investigated the influence of substituting Ti, Mn or Cu for Fe on the structural and hydriding properties of TiFe-type ternary/quaternary alloys [237, 242]. Ti substitution for Fe at the B site, usually described as $TiFe_{0.9}$ but being exactly $AB = Ti(Fe_{0.947}Ti_{0.053})$ for 1*a* and 1*b* sites respectively in $Pm\bar{3}m$ space group (CsCl-type structure), was found to require almost no activation process [237]. Partial substitution of Fe by Mn relaxes activation conditions and lowers plateau pressures, while Cu seems to further decrease the first plateau pressure to form the monohydride (TiFeH) while destabilising formation of the dihydride ($TiFeH_2$) and shifting the second plateau pressure towards higher equilibrium pressures [242]. Substituted $Ti(Fe_{1-x}Mn_x)_{0.9}$ alloys combine easy activation and near-atmospheric plateau pressures, being good candidates for H storage applications [237].

Room-temperature activation of TiFe alloys has been also evidenced by the introduction of Cr and Zr as substituents, modifying the microstructure and activation mechanism [250, 251]. Based on the Ti–Fe–Cr ternary phase diagram, alloys containing 80 at% Ti(Fe, Cr) and 20 at% $Ti(Fe, Cr)_2$ were prepared [251]. Activation at RT was achieved when the overall Cr concentration is higher than 9.7 at%. Separate investigations of the Ti(Fe, Cr) and $Ti(Fe, Cr)_2$ single phase alloys revealed that the easy activation mainly relies on the fast H absorption of the AB_2 phase, and the Cr concentration in the AB_2 phase is critical. An optimal composition for Ti–Fe–Cr alloys can be designed given the conditions of easy activation at RT and maximum reversible capacity within an operating pressure range. Ti–Fe–Cr–Zr alloys also have similar RT activation capability with a smaller Cr content but a much less decrease in both the plateau pressure and usable storage capacity compared to the Ti–Fe–Cr alloys [250]. Here, Zr preferentially enters into AB_{2s} phases, while Cr distributes between *AB* and AB_2 phases. No significant degradation of H capacity was observed after 50 cycles at 28 °C mainly between TiFe and TiFeH.

While many 3*d* TM elements normally replace the Fe sublattice in TiFe, V can replace both the Ti and Fe sublattices. DFT calculation predicts that the substitution of Ti with V yields a unique effect: the equilibrium pressures of TiFe/TiFeH (P_1) and TiFeH/$TiFeH_2$ (P_2) become closer, resulting in a decreased P_2/P_1 ratio. In fact, a low P_2/P_1 is desirable as the two-step TiFe hydriding reaction is contained within a narrow pressure range [252].

Surface modification or pre-treatment can also be considered for improving the rate of initial activation of TiFe. Surface catalytic effects can improve the dissociative chemisorption of H_2 molecules [253], and the introduction of surface modifiers can reduce the negative impacts of oxygen and other surface impurities that can limit hydriding rates. Examples of metal deposition for surface modification of TiFe for improved

initial activation [253, 254] include the use of a metal–organic chemical vapour deposition (MOCVD) technique to deposit metallic palladium, as well as argon- and H-ion implantation [255]. Nevertheless, depending on the specific TiFe-based material, these methods can require different degrees of technical effort and may offer not the same level of improvement.

In addition to chemical modification, treatment based on the introduction of mechanical forces is another effective way for activating TiFe, including ball-milling and cryomilling [256, 257], cold rolling [258] and groove rolling [257, 259], SPD through HPT [239, 257, 259–262] and ECAP [257]. These mechanical treatments change the microstructure of TiFe and its surface oxide, while also generating clean TiFe surfaces that can help to reduce the effort of initial activation.

Tailoring and scale-up of substituted-TiFe intermetallic compounds towards use in real applications can be performed by mechanical ball milling, as recently demonstrated by Bellosta von Colbe *et al* [256]. The ball milling process modifies grain boundaries and interfaces, which can enhance activation. The effect of ball milling and cryomilling on Zr-modified TiFe alloys was investigated by Lv *et al* [263], who found that particle size is effectively reduced, improving activation and kinetics [263]. When Zr was introduced (TiFe + 4 wt.% Zr), the microstructure and initial hydriding kinetics were positively modified. On the other hand, the cryomilling process was not beneficial for H storage, and long milling times reduced the total H storage capacity. The increased kinetics were likely caused by the reduction of the crystallite sizes and the formation of new grain boundaries that enhanced H diffusion. The decreased H storage capacity with long milling time was attributed to the increase of the relative volume of grain boundaries. This suggests that grain boundaries, while acting as H diffusion pathways, are not storing H within their structure. In an investigation of TiFe + 4 wt.% Zr + 2 wt.% Mn alloy, Manna *et al* showed that after 30 d of air exposure, the alloy was completely inert to H [264]. However, ball milling for 30 min made the sample absorb H again, albeit with only 1/4 of the initial capacity. A much better technique to regenerate the air-exposed alloy is cold rolling. After five rolling passes in air, the 30 d air-exposed sample absorbed H as fast as the as-cast alloy and retained 2/3 of the initial capacity.

5.2.1. Multiscale modelling of TiFe activation

The examples listed above highlight the fact that the passivation and activation behaviour is highly sensitive to processing and operating conditions, as well as surface and alloy composition. Nevertheless, the specific mechanisms that govern the rate limitations and activation within the surface oxide remain relatively poorly understood. Recent multiscale modelling and simulation efforts for investigating the initial activation mechanisms of hydriding of TiFe are taking steps towards addressing this gap. These models incorporate a variety of interfacial kinetic processes occurring during H absorption and desorption, starting from surface reactions of sorption and diffusion, followed by interfacial diffusion and proceeding to phase nucleation and growth at the grain boundaries. The aim is to go beyond thermodynamics alone in understanding the activation process.

Because the key mechanism for determining the activation conditions and incubation time is closely associated with H permeation through the surface oxide, it is critical to model the character of the oxide correctly. Single-crystal oxides often have low H solubility and can be difficult to permeate; however, more realistic surface oxides are polycrystalline or amorphous. Because disorder at grain boundaries, interfaces, and in the amorphous regions may be more susceptible to H and can therefore aid in the activation process, these features should also be considered in atomic-scale models. An additional unknown feature is how the structural and chemical heterogeneity at the oxide/metal interface affects H solubility and transport into the metal to initiate the storage reaction.

Figures 12(a) and (b) show examples of how DFT-based simulations are being used by LLNL and Hereon to probe structural characteristics and H incorporation into these challenging interfacial and disordered regions of the oxide film. The general approach involves elevated-temperature *ab initio* MD simulations, which have been applied to create disordered models of the oxide/metal interface region (figure 12(a)) and amorphous TiO_2 (figure 12(b)), among other relevant structures. For instance, a recent study-utilized this approach to obtain an atomistic view of the initial TiFe surface oxidation stage and the interaction of the oxide/metal interface with H (figure 12(a)) [265]. In the simulation, the top TiFe surface layers were gradually exposed to oxygen molecules, which resulted in immediate formation of the first oxide atomic layer and subsequent oxide build-up on the metal surface. Simulation snapshots provided helpful insights into commonly appearing motifs at the oxide/metal interface and in certain bulk oxides. The energetics of H_2 molecule interactions with these near surface regions were also assessed, including the dissociation energetics and its interaction with the surface oxide prior to full incorporation.

A similar analysis of H incorporation into bulk models of disordered oxides, which can act as proxies for disordered, high-angle grain boundaries, interfaces, and amorphous regions, has also been carried out (figure 12(b)). Ordered and disordered structures for various oxide compositions (e.g. TiO_2, Fe_2O_3, Fe_3O_4,

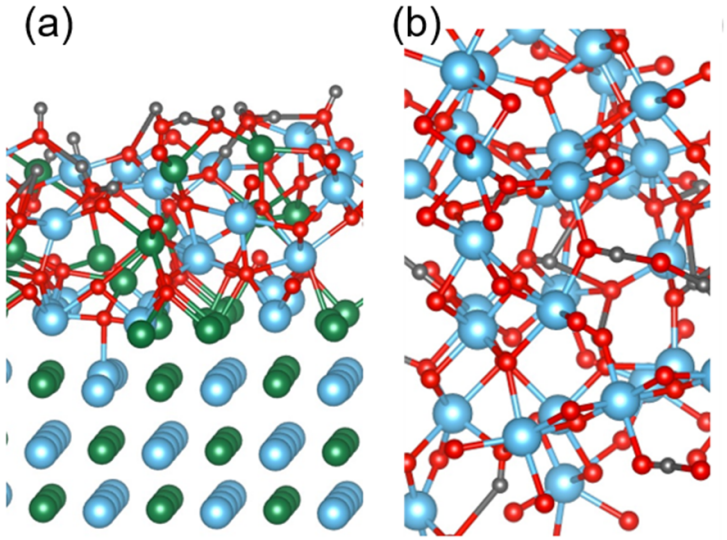

Figure 12. Snapshots of (a) H insertion into oxidized TiFe surface, and (b) H in disordered TiO_2. Grey, red, light blue, and green spheres represent H, O, Ti, and Fe atoms.

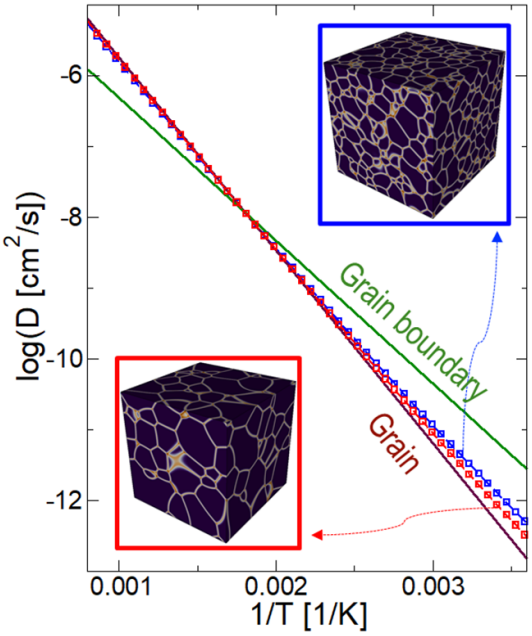

Figure 13. Modelling of H transport in polycrystalline TiO_2 accounting for H in disordered grain boundary regions. The computed effective H diffusivities of constructed TiO_2 polycrystalline structures with different grain sizes are reported (larger size = red, smaller size = blue). Diffusivity in single crystal and in grain boundary are reported as continuous lines for comparison.

and $TiFeO_3$) have been generated to probe differences in H interaction among the possible phases and compositions within the oxide. Ranges of H incorporation energies and barriers for H mobility can be assessed from such models, and results can form the basis for parameterization of multiscale permeation simulations.

An example of how atomic-scale data can be incorporated into a multiscale permeation simulation is depicted in figure 13. Here, phase-field methods were first used to generate controlled, realistic grain structures in a polycrystalline TiO_2 film. Two key parameters were then incorporated to determine the effective permeability through the generated microstructures: local H solubility and local H diffusivity in both the crystalline grain and disordered intergranular boundary regions. These properties were computed with DFT. Next, an effective property calculation method developed by Heo *et al* under HyMARC [266, 267] was used to extract the effective H diffusivity through the complex microstructure. Figure 13 extracts

illustrative cases of computed effective diffusivities for two different average grain sizes in polycrystalline TiO_2, showing the importance of grain boundaries in determining H permeation at elevated temperatures.

Beyond multiscale modelling approaches, close integration of models with experiments (structural and volumetric investigations, experimental design, statistical analysis) and data science approaches represents an emerging frontier for modelling kinetic activation. It is expected that these activities will play an increasingly important role in assessing the relationship between oxide composition, microstructure, and H permeation kinetics at different temperatures. The results will be critical for rationally guiding further processing and compositional modifications towards improved TiFe performance and cyclability.

5.3. Laves type hydrides

5.3.1. General regularities of hydride formation in Laves type intermetallics

The AB_2 Laves type alloys belong to a very extensive group of H storage materials that have been widely studied since the '80s. As A metals, the most robust H storage alloys that withstand pressure- and temperature-cycling contain Ti, Zr, Ta, and Hf, while the B elements include TMs such as Fe, Co, Ni, Mn, Cr, V, and non TM element Al. The most abundant are FCC C15 and hexagonal C14 type structures.

AB_2 Laves type alloys absorb up to 6 at. H/formula unit AB_2 (C15 ZrV_2H_6 and C14 $ZrVNbH_{5.4}$) and achieve practical reversible H storage capacities in a range between 1.5 and 2.0 wt.% H while also demonstrating high rates of H charge and discharge, thus making them suitable for building efficient H stores operating at ambient conditions.

The challenge in using Zr-based AB_2 alloys is in their sluggish H absorption kinetics and easy poisoning by reactive gases that may be present even in trace amounts. Fortunately, the RE metals (including mischmetal and La) when added to the composition of the AB_2 alloys, improve their activation behaviour. The catalysing effect of REs is caused by the presence of a secondary LaNi/MmNi phase easily forming a tetrahydride (La/Mm)$NiH_{3.6}$ and thus promoting hydriding of the matrix Laves phase.

In the multi-element $AB_{2\pm x}$ alloys, the constituting elements contribute to the H storage performance in a variable way. Indeed, Ti, Zr, and V are the hydride-forming elements A, Ni has a high catalytic activity facilitating H_2 splitting, Co and Mn provide surface activity that improves of H exchange, while Cr, Al, and Fe increase alloys stability on cycling.

Hydrogen storage capacity, thermodynamics and kinetics of the formation-decomposition of the Laves type hydrides are defined by a number of factors. These include:

(a) Type of intermetallic structure—FCC C15 $MgCu_2$ type or hexagonal C14 $MgZn_2$ type. Intermetallics with C15 type structures demonstrate fast kinetics of H diffusion and high rates of H charge and discharge while hexagonal C14 type intermetallics show high H storage capacities. Furthermore, mean electron concentration favours C15 (above 6.9 el. metal atom^{-1}) or C14 type structures (below 6.9 el. metal atom^{-1}) [268, 269].

(b) The ratio between Ti and Zr forming a solid solution on the A side defines the thermodynamic properties and stabilities of the AB_2H_x hydrides. In fact, while Ti and Zr have similar chemistry, they differ significantly in atomic size (Ti = 1.462 Å; Zr = 1.602 Å). Therefore, by increasing the Ti vs Zr content in the AB_2 intermetallics (up to a maximum value of 22 at.% for $Ti_{0.22}Zr_{0.78}$), a gradual contraction of the unit cell is observed, which causes a destabilization of the corresponding hydrides [270, 271].

(c) Elements and their relative content contributing on the *B* side (Fe, Co, Ni, Mn, Cr, V, and Al). An empirically defined optimal ratio of mixing of four TMs on the *B* side, namely $Ni_{10}Mn_{5.83}VFe$, allows to achieve excellent reversibility with extremely small hysteresis between the absorption and desorption isotherms (see figure 14). This makes it possible to carry out energy-efficient H_2 compression and to decrease overpotential of the metal hydride anodes [270, 271].

(d) The ratio between *B* and *A* can change between $AB_{1.9}$ and $AB_{2.1}$ while keeping a single-phase Laves type structure unchanged. Increase of the *B*/*A* ratio in the alloys causes a gradual contraction of the unit cell and a corresponding destabilization of the hydrides, which allows their stability to be finely tuned [271].

(e) Surface state and its activity towards H_2 splitting. The surface activity of Laves type Zr/Ti-based alloys is a challenging issue in achieving their efficient activation. Adding small amount of RE metals—La, Mm—solves the problem. These alloys do not form substitution derivatives replacing Zr on the *A* side. Instead they form secondary intermetallic RENi which easily form a hydride and provide the channels for the transfer of atomic H to the Laves type alloys, thus efficiently catalysing their activation performance [272].

(f) Homogeneity of the alloys and presence of secondary phases. Laves type H storage alloys can be easily obtained as single phase materials by selecting and optimizing their chemical composition and by annealing them at optimum temperature of 950 °C [270–274].

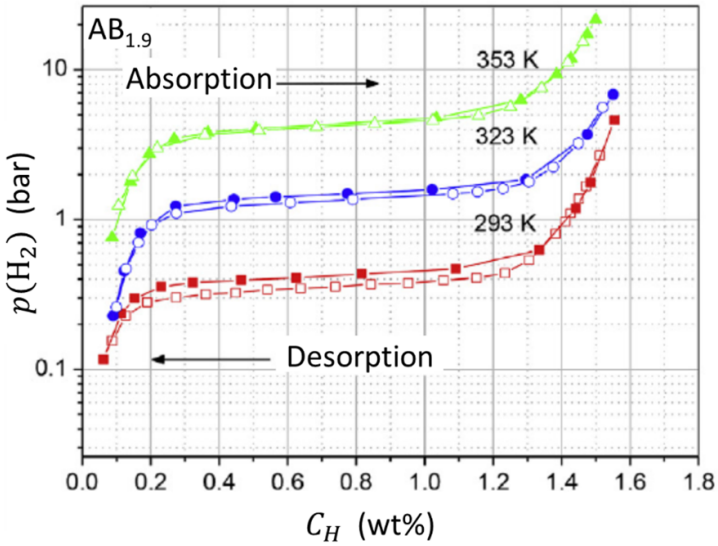

Figure 14. Temperature-dependent variation of the PCT curves for the $AB_{1.9}$ Laves type hydride showing several beneficial features, including (i) negligible hysteresis between absorption and desorption; (ii) flat single-plateau isotherms; (iii) merging of the isotherms of abs–des at 353 K thus indicating a proximity of the critical temperature.

(g) Grain size and effect of nanostructuring. Decreasing grain size increases the rates of H diffusion in the alloys. Planetary ball milling and rapid solidification were systematically studied in relation to the H storage performance and proved to cause beneficial changes [275–277].

5.3.2. Mechanism and kinetics of H sorption in a Zr/Ti-based Laves type alloy

A recent detailed study on the kinetics of H interaction with the Ti/Zr-based Laves phase alloys [278] was focused on $Ti_{0.15}Zr_{0.85}La_{0.03}Ni_{1.126}Mn_{0.657}V_{0.113}Fe_{0.113}$ that belongs to a family described above and contains La to improve the activation performance and cycling stability. The composition was selected based on in-house research performed at IFE on $AB_{2\pm x}$ C15 Laves-type alloys for their application as H storage and battery electrode materials.

Experimental data on H absorption and desorption were collected at isothermal conditions using a single-step charge/discharge while assuring a strict temperature stabilization of the sample. The experimental and modelling study of sorption kinetics was based on the application of the JMAK model modified by introducing pressure- and temperature-dependent rate constants. This approach yielded an excellent agreement with the experimental data as shown in figure 15. The temperature-dependent rate constant exhibits a classical Arrhenius-type behaviour, while the pressure-dependent term is directly related to the transformation mechanism and varies depending on the rate-limiting step of the process. The obtained Avrami exponent is $n = 1{-}1.25$ for absorption and $n = 1$ for desorption, indicating that the rate-limiting H sorption steps are jointly governed by H diffusion and grain boundary nucleation of α-solid solution and β hydride phases. The activation energies for both H absorption and desorption decrease with increasing H content in the hydride.

5.3.3. Determination of the heat transfer parameters relevant for the design of H storage systems based on Laves type hydrides

Scaling up metal hydride storage tanks to a kg or even ton scale rule implies that H uptake and release are no longer constrained merely by the intrinsic materials kinetics but turn into heat transfer-controlled mechanisms [279]. Therefore, the knowledge of the heat transfer properties is important for the design and optimization of solid-state hydrogen-energy reservoirs through numeric and experimental investigations. An efficient heat management technique for large storage systems is mandatory to reduce the uptake and release times and the temperature spikes inside the H storage tanks [280].

Among the properties of the hydride-forming material relevant to describe the heat transfer performance, the heat capacity and the effective thermal conductivity are the most important ones. The analysis of the heat transfer parameters was performed for the AB_2 C14-Laves alloy $((Ti_{0.9}Zr_{0.1})_{1.25}Cr_{0.85}Mn_{1.1}Mo_{0.05}$ with 10% addition of expanded natural graphite (AB_2-10 wt.% ENG material) utilized for the validation of the hybrid H storage concept (high-pressure gas and solid-state) [281].

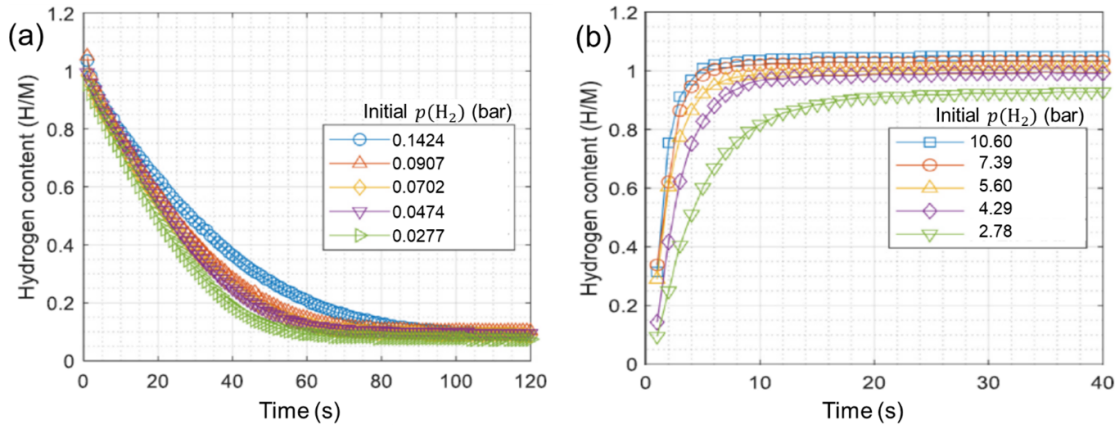

Figure 15. Experimental data and fitted pressure-dependent kinetics for (a) absorption and (b) desorption, both at $T = 293$ K. Clearly, an increase in pressure increases the absorption rate and decreases the desorption rate.

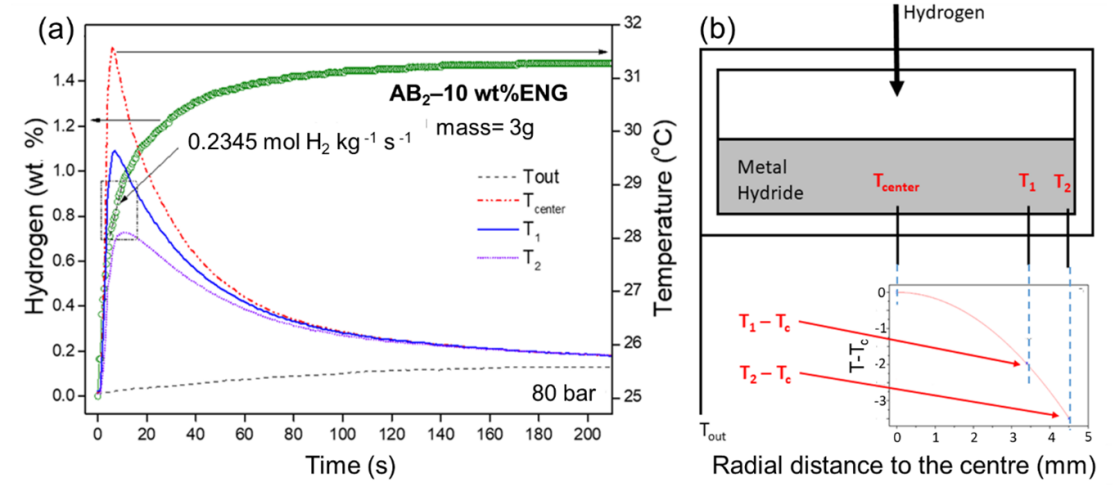

Figure 16. Determination of k_{eff} for the AB_2-10 wt.% ENG material: (a) temperature profiles and H content of the hydride bed upon hydriding. (b) Sketch of the experimental cell (above) and fit of the parabolic dependence of temperature on the radial distance (below).

The heat capacity at constant pressure C_P of the AB_2-10 wt.% ENG was measured by the linear temperature ramp method [282] as the ratio Φ/β between heat flux $\Phi = dQ/dt$ and heating rate $\beta = dT/dt$ and fitted as a function of T by applying the Shomate equation. In the reported simulations of hydride-based reservoirs, including the one discussed here, a C_P value of 500 J (kg K)$^{-1}$ at RT was assumed for the systems $LaNi_5$ [283, 284], $LaNi_{4.91}Sn_{0.15}$ [283], and Laves type $Ti_{1.1}CrMn$ [285]. The C_P of $(Ti_{0.9}Zr_{0.1})_{1.25}Cr_{0.85}Mn_{1.1}Mo_{0.05}$ has a quite similar value in the range of 500–514 J (kg K)$^{-1}$ at $T = 40$ °C–95 °C.

A sensitivity analysis via modelling of the material performance showed that the most relevant parameter affecting the hydriding process is the effective thermal conductivity k_{eff} [284, 286], which refers to the thermal conductivity of the hydride measured under H_2. By using a specially designed cell of a titration apparatus with thermocouples placed at different radial distances from the centre, it was possible to monitor the time- and pressure-dependent changes in the temperature of the hydride bed during hydriding/dehydriding, as shown in figure 16(a).

It was found that k_{eff} changes in the radial direction but not in the axial direction and that the hydride bed in steady state is a homogeneous cylinder [279, 282]. The temperature difference from the centre $\Delta T = T - T_c$ has a parabolic profile along the radial direction $\Delta T = mr^2$. The effective thermal conductivity can be determined as:

$$k_{eff} = \dot{Q}\rho/4m \tag{9}$$

where $\dot{Q}$ is the heat rate and ρ is the density of the hydride bed. The analysis of the data in figure 16 yields $k_{eff} = 9$ W (m K)$^{-1}$ at $p(H_2) = 80$ bar and $T = 25$ °C. This value agrees well with the ones reported for other

hydride systems, such as MgH_2 + 10 wt.% graphite (k_{eff} = 8 W (m K)$^{-1}$ [287]), TiH_2 + 10 wt.% graphite (k_{eff} = 20 W (m K)$^{-1}$ at 500 °C [287]), compacted hydralloy + 5 wt.% ENG (from k_{eff} = 14 W (m K)$^{-1}$ as-compacted to 7.5 W (m K)$^{-1}$ after cycling [288]). The experimental setup allows the dependence of k_{eff} on $p(H_2)$ and T to be determined [283, 289]; finally, the obtained values can be applied to model and design scaled-up H storage tanks.

5.4. High-entropy alloys (HEAs)

HEAs are characterized by having at least four constituents in near-equimolar ratio which form a solid solution with simple crystal structures like BCC, FCC or HCP. They have primarily attracted interest due to exceptional mechanical properties at high temperatures [290], but have lately also been studied for other applications such as H storage [291]. The interest for the latter application area was sparked by Sahlberg *et al* reporting that the five-element BCC HEA TiVZrNbHf absorbed H up to H/M = 2.5 [292], which is significantly higher than in previously reported TM alloys that reach H/M = 2.0 at maximum. Zlotea *et al* reported TiZrNbHfTa equimolar BCC alloy which absorb H up to H/M = 2.0 [293]. Both TiVZrNbHf and TiZrNbHfTa were reported to absorb H at around 300 °C, but no desorption PCIs have been reported. Further developments of HEAs for H sorption will focus on identifying compositions that operate around RT and display good cyclability.

On the basis of empirical maps for HEAs [294], Spaliviero *et al* have investigated H sorption in the $TiV_{0.6}Cr_{0.3}Zr_{0.3}NbMo$ HEA [295], which consists of a solid solution with BCC structure, plus a fraction of a Zr-rich C15 Laves phase. The maximum H storage capacity was determined at 300 °C equal to 1.2 wt.%, equivalent to ≈88 kg of H per m^3 of alloy. At 10 bar, a BCC solid solution with a lattice constant of 3.298(1) Å is formed, while higher pressures (over 50 bar) induce the transformation to a FCC metal hydride, with a lattice constant of 4.410(1) Å. By calorimetric analysis and XRD of hydrogenated samples, it has been observed that the material begins to desorb H at temperatures close to 55 °C, with a maximum rate at ≈75 °C. The presence in the alloy of the elements with different affinity to H leads to a promising storage capacity, with sorption reactions proceeding at low working temperatures.

Akiba *et al* developed five-element alloys by adding two elements to the TiVCr BCC alloy [296]. BCC TiVCrNbMo and $Ti_{0.1}V_{0.3}Cr_{0.2}Nb_{0.1}Mo_{0.3}$ alloys can be readily activated and absorb and desorb H at 30 °C. They show RT H absorption/desorption and good cyclability.

Experimentally synthesizing, characterizing, and testing the equilibrium hydriding thermodynamics of HEAs requires significant resources. As a result, the chemical space that can be explored in practice is miniscule compared to the possible number of compositions. Equimolar compositions in the 37-element space spanned in [290] produce ∼13 million possible equimolar HEA compositions with between four and seven different metal elements. First-principles simulations, such as computationally expensive enhanced-sampling Monte Carlo, can rigorously predict a PCT curve but do little to address this situation, particularly since high-accuracy, many-element force fields or an *ab initio* potential energy surface is required. These are either manual-time or compute-time intensive. A main effort has therefore been to establish ways to predict the H sorption behaviours HEAs based on the compositions [297, 298]. Large *local lattice strain* (δr) caused by size mismatch of the constituent atoms, has been suggested to be the reason behind the special properties of many HEA properties. It can be quantified by $\delta r = \sqrt{\sum_{i=1}^{n} c_i \frac{(r_i - \bar{r})^2}{n}} \times 100\%$, where c_i and r_i are the concentration and atomic radius of element i, and $\bar{r}$ is the average element radius in mixture of n elements. However, a survey of nine HEAs with compositions $TiVZr_xNbTa_{1-x}$ and $TiVZr_{1+y}Nb$ and δr between 3.53% and 6.34% did not reveal any correlation between δr and the maximum H/M. On the other hand, a strong correlation between the *valence electron concentration* (VEC) and H sorption properties was found in a study of seven quaternary and three quintenary equimolar BCC HEAs, where the stability of the hydride phase decrease with increasing VEC [297]. Under the applied hydriding conditions (RT, 20 bar H_2), the HEAs with VEC < 5.0 formed FCC hydrides with H/M = 2 while VEC > 5.0 resulted in hydrides with significantly lower H content. VEC = 5.0 is a borderline case where some HEAs form hydrides with full capacity (H/M = 2) while others achieve lower H contents. This VEC value thus represents the optimal combination of the highest possible capacity and the lowest possible desorption temperature. TiVCrNb, which is a VEC = 5.0 compound with full H capacity (H/M = 2; 3.1 wt.% H), was tested for H cycling. By alternating between 20 bar H_2 and dynamic vacuum, the material reversibly absorbed-desorbed 1.96 wt.% H over ten cycles. A combined neutron and synchrotron total scattering measurement of the hydride obtained after a full desorption at RT, $TiVCrNbD_{2.2}$ (deuterium was used rather than H due to a strong incoherent neutron scattering from natural H), revealed that the remaining H prefers interstitial sites coordinated by the low-VEC atoms [299]. Similarly, in the slightly under-stoichiometric deuteride $TiVNbD_{5.7}$ it was found that vacant tetrahedral sites were mostly coordinated by elements with the highest VEC (Nb and V; VEC = 5)

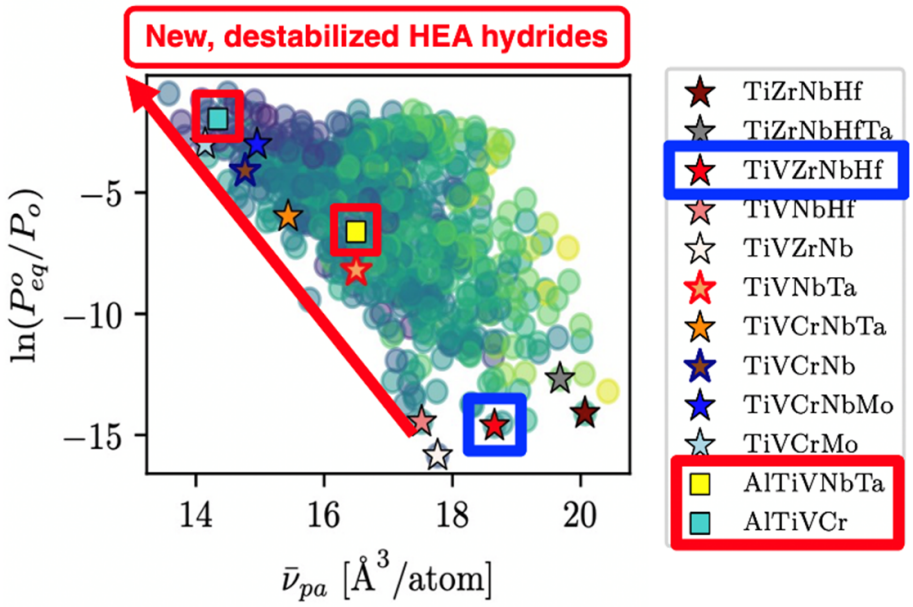

Figure 17. The ML-predicted equilibrium plateau pressure at 25 °C, $\ln(P^o_{eq}/P_o)$, plotted vs the composition fraction weighted mean elemental volume per atom, $\bar{\nu}_{pa}$, which is the most important feature in the ML model [302]. The benchmark HEA hydride is highlighted in blue along with the new destabilized HEA hydrides experimentally validated in [298] highlighted in red.

while sites coordinated by 3 or 4 Ti (VEC = 4) atoms were almost always occupied [300]. This shows that the inverse relationship between VEC and hydride stability applies also at a local atomic level.

Attempting to predict hydriding properties from a single parameter is the simplest approach, while a more comprehensive solution is to model HEA hydride thermodynamic properties via ML/data-driven techniques. Using gradient boosting tree models trained on the historical HydPARK database [301, 302], showed that compositional featurization [303, 304], i.e. in which material's features do not directly rely on the crystal structure, led to the predictive capabilities for the enthalpy of hydriding and to some extent the entropy of hydriding. Consequently, the equilibrium plateau pressure (and thus the Gibbs free energy of reaction) could be reliably predicted. Furthermore, the use of 'explainable' ML tools revealed simple, first-order design rules that, while not as accurate as the ML model itself, provide intuitive understanding of the model predictions and establish a correlation of the hydride stability with purely physical characteristics [302]. These efforts enabled high-throughput screening of HEA hydriding thermodynamics across all 4-,5-, and 6-element equimolar alloys in the {Al, Ti, V, Cr, Zr, Nb, Mo, Pd, Hf, Ta} space (672 possible compositions) [298]. The model predicted that the equilibrium plateau pressure varies over many orders of magnitude within this material set (figure 17), and that the mean element volume per atom, $\bar{\nu}_{pa}$, is the parameter with the strongest correlation to the thermodynamic stability. Experimental efforts validated the ML model predictions quantitatively for several novel HEA hydrides, including AlTiVCr, which exhibits a H_2 desorption enthalpy of ∼20 kJ mol H_2—lower than the benchmark TiVZrNbHf [292]. The resulting open-source code and associated data now provide a platform for the targeted experimental identification of the HEA hydrides with a desired thermodynamic stability. Future efforts will enable extensions of this model to identify HEA with other desirable properties, such as high H capacity. It is worth noting that the most significant limitation of this approach is the lack of a *standardized and centralized* database, as HydPARK has many limitations [302]. This issue has been largely resolved in the other areas of the materials research [305, 306]. A concerted effort within the H storage community to develop centralized repositories for accurate H storage data in standardized formats will be essential to unlock the full potential of data-driven approaches for the metal hydride discovery.

5.5. Pd-containing intermetallic compounds

Some binary intermetallic compounds of Pd, when alloyed with other hydride-forming metal elements, including $ZrPd_2$, $TiPd_2$, $HfPd_2$, UPd_3, do not form hydrides at ambient pressures and temperatures even though Pd and *A* metals (*A* = Zr, Ti, Hf and U) possess a high affinity to H. In order to shed light on this puzzling behaviour, new $Zr(Pd_xM_{1-x})_2$, *M* = V, Cr, Mn, pseudobinary intermetallic compounds with low Pd content, $x < 0.3$, have been studied [307–309]. The variation of the hydriding properties has been related to the extent of substitutions and to the reported hydrogen inactivity of $ZrPd_2$ [310]. The H absorption

capacity of these ternary $Zr(Pd_xM_{1-x})_2$ compounds appears to be rather high, 3.5–5 at.H/f.u. As shear modulus is considered as a parameter correlating with H storage capacity, a comparison of the shear moduli of Laves type $Zr(Pd_xM_{1-x})_2$, M = V, Cr, Mn, $x < 0.3$, intermetallics with the shear modulus of $ZrPd_2$ has been performed and this comparison eliminated it as the reason for the inactivity of $ZrPd_2$ in forming a hydride [311]. At high H_2 pressure of 60 bar, H sorption capacity of ~0.55 at.H/f.u. has been reached for $ZrPd_2$. Thus, it is reasonable to suggest that $ZrPd_2$ and other Pd-containing intermetallics, all having rather large heats of alloy formation, are able to form the hydrides at $p(H_2)$ in the kilobar range.

Analysis of the hydriding performance shows that hydride stabilities of the $Zr(Pd_xM_{1-x})_2$, M = V, Cr, Mn, compounds are defined by interplay between the heats of alloy formation and crystal cell volumes, i.e. the combined effect of Miedema's rule of reversed stability [19] and intermetallic crystal volumes [312]. High H absorption pressures required to synthesize $ZrFe_2$- and $ZrCo_2$- based hydrides may be reduced by small Pd substitutions for Fe and Co. Furthermore, the slopeness and the flatness of the H absorption isotherms is different respectively for $Zr(Pd_xCr_{1-x})_2$ and $Zr(Pd_xMn_{1-x})_2$, even though these two systems have common features. Critical temperatures T_c of about 565 K have been evaluated for $Zr(Pd_xM_{1-x})_2$–H_2 systems with $x = 0$, 0.05, 0.1 [309]. A particular value of T_c is determined by elastically mediated attractive H–H interactions as well as by repulsive, neutral or attractive H–H electronic interactions.

Although the number of the hydrides of pseudobinary intermetallics is almost unlimited, synthesizing new hydrides of binary or even ternary compounds is a relatively seldom event. The formation of two thermodynamically stable at RT intermetallic hydrides has been observed during the hydriding of $CaPd_2$ and CaPdMg.

$CaPd_2$ ($MgCu_2$-type Laves phase) becomes amorphous after absorbing about 2H atoms/f.u. at 60 bar H_2 and RT. The atomic size ratio Ca (1.974 Å): Pd (1.376 Å) is 1.43 [313] and it well exceeds the limiting value of 1.37 set for the H-induced amorphization caused by the hydriding of the C15 AB_2 Laves compounds [314]. After exposing to air, $CaPd_2$ hydride returns back to its original Laves phase structure. A significant broadening of the XRD pattern in the recovered $CaPd_2$ intermetallic compound indicates presence of the residual elastic strains.

CaMgPd (orthorhombic TiNiSi-type) absorbs 3.4–3.5 and 3.7H atoms/f.u. at 1.3 and 60 atm H_2 pressure, respectively. This is similar as to the related ZrNiAl-type LaMgPd compound, which absorbs 5 at.H/f.u [5, 315]. $CaMgPdH_{3.7}$ retains the crystal structure of the original intermetallic and undergoes 24% volume expansion upon hydriding. $CaPd_2$ and CaPdMg hydrides disproportionate above 100 °C.

5.6. Binary and oxygen-modified hydrides as reference systems

5.6.1. Rare earth (RE) hydrides

RE metals form di- and trihydrides, and the H content in the hydride phases together with the nature of the RE element defines their magnetic and electronic properties. The mechanism of REH_3 decomposition, which proceeds via two consecutive events $REH_3 \rightarrow REH_2 + 1/2H_2$ and $REH_2 \rightarrow RE + H_2$, has been established for RE = Y, Ce, Pr, Nd, Sm, Gd and Tb by Yartys *et al* [316]. Their complete decomposition takes place under high vacuum, at temperatures up to 1093 K according to TDS.

Recently, the kinetics and the mechanism of H desorption from the trihydrides of the 'heavy' REs: DyH_3, HoH_3, and ErH_3 were studied [68]. Two H evolution events were observed by TDS. The low-T one, associated to the $REH_3 \rightarrow REH_2 + 1/2H_2$ decomposition, gives rise to one peak at $T < 513$ K. The high-T one yields a more intense peak at $T = 1023$ K–1173 K and corresponds to $REH_2 \rightarrow RE + H_2$. The Kissinger method allowed their activation energies to be determined: the comparison with the results obtained on 'light' REs hydrides [316] reveals that trihydrides of heavy REs display lower thermal stability than those of light REs. Dihydrides show the opposite behaviour, being more stable for the heavy REs. For DyH_3 and ErH_3, the shapes of the TDS peaks were well described by a nucleation and growth model, while a phase boundary reaction appeared to control the dehydriding of HoH_3.

5.6.2. Effect of oxygen on the properties of metal-H systems

Oxygen (O) is always present in the composition of alloys. Its amount depends on the O content of the precursor elements as well as the time-temperature history of their preparation, including the gaseous environment and melting vessel.

Oxygen affects various aspects of metal–H interactions: H_2 dissociation and penetration through the surface, its diffusion into the bulk material, selection of H residence sites in the metal sublattice and, most importantly, H storage capacity and thermodynamics of the metal–H interactions. The most important aspects of H storage in O-containing materials include O influence on surface and bulk properties, as briefly summarised below.

(a) *Bulk behaviour*. When accommodated in the metal sublattice, O atoms fill the largest available octahedral interstitial sites Me_6 (Me = Ti, Zr), such as in Zr_3O, η-Ti_4Fe_2O and η-Zr_3V_3O [317].
(b) *Bulk behaviour*. Interstitial O decreases the stability and reduces the decomposition temperatures of the O-containing oxyhydrides as compared to O-free hydrides, and decreases occupancies by H atoms of the interstitial sites surrounding O-filled octahedra [318].
(c) *Bulk behaviour*. At high temperatures, O dissolved in the metal affects the mechanism of hydriding and dehydriding causing O-redistribution between the phase components and its eventual segregation to form stable, not dissolving hydrogen oxides. The phase composition of the hydrides (Ti–H system) can be manipulated by fine-tuning of the temperature- and time-dependent parameters of the oxidation process of TiH_2 [319–321].
(d) *Surface behaviour*. Surface oxide phenomena in H absorption kinetics of metals have been studied in detail for a long time [322]. Recently, the influence of surface oxides on the hydriding of thin Ti films was studied by XRD, electron microscopy and resistivity measurements [323]. Thin films of Ti covered with natural oxide show a reasonable hydriding rate at 300 °C with a layer-like growth of the hydride nucleated at the backside interface to the substrate. The pressure dependence of hydriding at 300 °C reveals that the rate-limiting step is diffusion across the oxide rather than H_2 splitting at the surface. The knowledge of diffusion mechanism as well as diffusion coefficients can help in improving materials for future use.

6. Applications of metal hydrides

Several classes of hydrides have already found use in commercial applications, such as sodium alanate in chemical reduction reactions and derivatives of $LaNi_5$ in Ni–MH batteries. Concerning Mg-based hydrides, demonstrators for both hydrogen and heat storage applications have been developed, as briefly reviewed below, but their market uptake is still lacking. Intermetallic hydrides have been more successful, especially thanks to Ni–MH batteries, and an expansion of their use is all but guaranteed, in particular considering the future need to store green hydrogen produced from renewable energies sources.

6.1. Mg-based hydrides

The appealing properties of MgH_2 led many researchers to explore its use for both H and heat storage applications [5, 6, 324–329]. The scale-up of Mg-based H storage systems requires an efficient heat management because of its high reaction enthalpy. A good example was provided by the realization of a tank with a MgH_2 content of 10 kg, a total weight of 55 kg and an internal volume of 14 l [330] that used a high temperature heat transfer fluid coupled to a heat source/sink. The system was able to store 0.6 kg of H, yielding an energy density of 360 Wh kg^{-1}, with loading and release times shorter than 1 h.

For heat storage, the functionality of MgH_2 was also successfully demonstrated using a rather large steam generator (19.4 l, 14.5 kg of MgH_2 for a total weight of 40.5 kg [326]) that showed a capacity of 0.835 kWh kg^{-1} of hydride for a temperature difference of 200 °C. For comparison, in order to get a heat storage capacity of 0.835 kWh kg^{-1} or more when using water, the material with the highest specific heat among the candidates for heat storage using sensible heat (4.19 kJ kg K^{-1}), an infeasible temperature difference of more than 710 °C would be needed [331].

Despite the success of the above demonstrators, a commercial application of MgH_2 and its derivatives is not yet established [5, 104, 331]. The main hurdle is the lack of compatibility between the material requirements (high temperatures and a large supply of heat for H_2 release) and those of the target application, which typically operates well below 300 °C. Another challenge is that large scale systems must be realized, especially for the case of heat storage. The corresponding large investments necessary to build the storage systems have thus far discouraged users from implementing the technology.

Nevertheless, plans are underway to employ H in a much wider variety of applications, such as the steel industry [332, 333], than ever before. In such large-scale industrial contexts, temperatures much higher than 300 °C are standard; this could very well make Mg a cost-effective raw material, since it can be obtained from scrap metal [334] and serve as an economical alternative to other forms of H storage. Moreover, the use of Mg as a heat storage material, e.g. for solar thermal applications, has been championed for some time [4, 5, 104]. The development of such alternative energy-generating methods has been slow, but their maturity is now sufficient to challenge more traditional power plants [104, 331]. The time seems therefore ripe for applications of Mg-based hydrides to reach the market [104].

6.2. Intermetallic hydrides

Intermetallic alloys capable of storing H at RT (or below 100 °C, at any rate), are among the earliest used hydrides that have been considered for H storage [14, 335]. They account for the highest amount of commercially successful hydrides. Although the overwhelming majority of intermetallic hydrides is actually

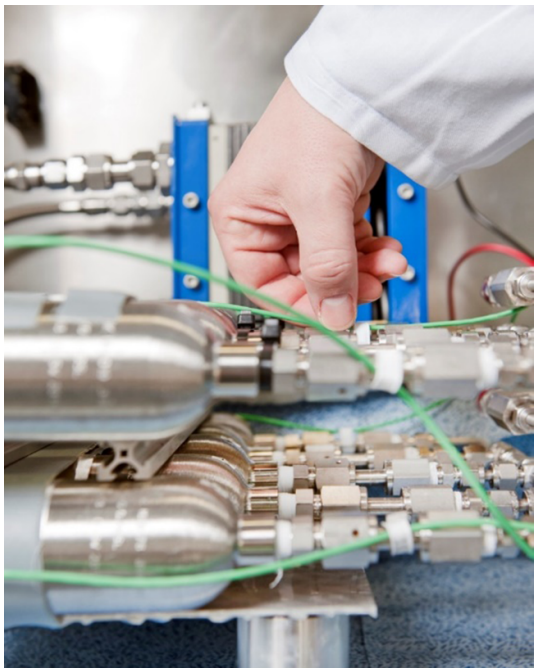

Figure 18. Metal hydride system for a prototype vehicle (metal hydride storage tanks in the foreground, fuel cell in the background).

found in Ni–MH batteries (basically to capture H produced during the electrochemical reaction) [336, 337], other applications have been highly successful as well. Submarines of class 212 and following classes (209 mod, 214, Dolphin) have used metal hydrides to store H underwater and provide power to PEM fuel cells in a routine way, even under the strict requirements of a military-grade application [222]. Due to military secrecy, the exact composition of this hydride was not published, although it is safe to assume that it is an AB_2 hydride because it must operate in a wide temperature range when the submarine is at sea from the tropics to polar regions. On the other hand, land-based mobility using these hydrides has been met with lukewarm acceptance. In fact, while experimental systems have been successfully developed (figure 18) [338] with a hydride weight of 9.5 kg, no commercial vehicles using this technology have achieved a widespread use.

In terms of energy storage density, H-driven fuel cells are superior to the rechargeable lithium-ion batteries reaching 2–4 times higher efficiency. Commercial implementation of H-powered forklifts using metal hydrides for H storage and PEM fuel cells boosts the development of pollution-free powertrains utilising H as a clean non-polluting fuel. For the forklift, high specific weight of the metallic hydrides is a benefit, as it allows counterbalancing the vehicle with no extra cost. The development is performed within the EU HORIZON2020 project HYDRIDE4MOBILITY [270] coordinated by Institute for Energy Technology as a joint effort of a consortium uniting academic teams and industrial partners from two EU and associated countries Member States (Norway, Germany, Croatia), and two partner countries (South Africa and Indonesia).

Another field of excellence of intermetallic hydrides is that of H compressors without moving parts, of which effective prototypes have been constructed and validated [47, 222]. In the case of [339], for example, the compression was from 10–20 bar to 200 bar with an average throughput between 0.7 and 1.3 $m^3\ h^{-1}$. The hydrides used in this work were an AB_5 alloy for the 1st stage (A = Ce, 15% and B = Ni) and an AB_2 for the 2nd stage, specifically an $AB_{(2-x)}$, where A = Ti + Zr and B = Mn + Fe + Cr + Ni and $x \sim 0.1$. Its structure is a C14 type ($MgZn_2$). It is to be expected that the advantages of reduced maintenance and noise, as well as the expected longevity of such compressors, will make them extremely popular in environments where the presence of the public cannot be avoided, such as refuelling stations.

Therefore, the development of a wide variety of H-oriented applications, as intended by the German [340, 341] and Japanese governments [342, 343] can be expected to give a decisive impulse to the commercialization of intermetallic alloys-based hydrides.

7. Summary and outlook

The IEA sees hydrogen as a key player in a clean, secure and affordable energy future. The ultimate goal for the transition to low-carbon energy future is green hydrogen produced from renewable energy.

The European Commission wishes to make the EU a pioneer in the use of hydrogen as an energy carrier. In 2020, it presented 'A hydrogen strategy for a climate-neutral Europe', the aim of which is to make the widespread use of hydrogen possible by 2050, with priority on green hydrogen. With the implementation of the hydrogen strategy, the European Commission aims at achieving various ambitious goals including: (a) a carbon-neutral EU by decarbonising sectors that are not accessible to direct electrification; (b) a better integration of wind and solar power with hydrogen as a storage medium; (c) the creation of new jobs within the hydrogen economy. The EU hydrogen strategy is part of the European Green Deal, that plans to attain a green hydrogen production rate of 1 Mt year^{-1} in 2024, reaching 10 Mt year^{-1} in 2030.

In the US, the DOE launched the Hydrogen Shot as the first Energy Earthshot initiative in June 2021, focused on reducing the cost of green hydrogen by 80% to USD $1 per kilogram within one decade [344]. These efforts are coupled to the activities of multi-institutional DOE consortia and other programs that focus on specific technology impediments to hydrogen production, storage, and delivery, as outlined in a recently issued DOE Hydrogen Program Plan [345]. Among these is the DOE Hydrogen Materials—Advanced Research Consortium, which focuses on the development of materials-based storage and liquid carrier solutions, with a target of doubling the energy density as compared to current pressurized tank-based storage. Hydrogen has also been recognized as a key economic driver in the US: a recent industry-led roadmap concluded that by 2050, the US H economy could generate USD $750 billion in revenue and 3.4 million additional jobs [346].

Australia has an abundance of natural resources for the production of renewable hydrogen and a vision to supply the world with clean hydrogen. The Australian National Hydrogen Strategy is to grow the hydrogen industry and position Australia as a major international player by 2030. It is forecast that Australia will produce up to 2 Mt of renewable hydrogen per year by 2030. The production of large quantities of renewable hydrogen will require storage solutions for domestic and export applications. To this end research in Australia will focus on increased volumetric energy storage densities in new materials for both domestic and export applications.

The 'Basic Hydrogen strategy' was established in 2017 in Japan, which sets a goal that the hydrogen cost will be reduced toward that for conventional energy. Then 'Green Growth Strategy Through Achieving Carbon Neutrality in 2050' was formulated in 2020. This strategy shows the challenging goals and future actions for 14 priority energy sectors to realize a carbon neutral society by 2050, and hydrogen technologies are involved in some of them. In order to boost the adoption of renewable sources, excess energy needs to be stored using batteries or hydrogen. Therefore, demonstration projects to store hydrogen, or transfer in local area using metal hydride tanks have been conducted. In addition, the large-scale metal hydride tanks were commercialized. However, material developments are still important for a wide distribution of hydrogen technology. Therefore, several projects to develop a new materials science of hydrogen/hydrides or improve the material properties have been conducted.

For the above reasons, the outlook for hydrogen storage materials looks brighter today than in the last 15 years, also thanks to the increased maturity of the technology. Stationary, mobile and portable hydrogen storage systems have specific targets to be met for their efficient and economically viable implementation. Both large storage systems for stationary fuel cells and small hydrogen storage and generation systems for portable applications will be on focus. However, no significant role for solid state materials in automotive transportation is envisaged, with the exception of hydrogen storage for forklifts powered by hydrogen fuel cells.

In this review, we have discussed the hydrogen storage properties of Mg-based hydrides and of different classes of intermetallic alloys-based hydrides, putting particular emphasis on recent developments, interesting scientific questions, and open challenges that need to be overcome to bring these materials closer to the market. Here below we report a brief summary for the different systems.

Magnesium-based hydrides, although offering high hydrogen capacity, cannot provide practical storage solutions today under normal conditions of pressure and temperature due to intrinsic stability (thermodynamic limitation) and low sorption rates (kinetic limitation). Modification of Mg–H thermodynamics is highly challenging, but improvement of reaction kinetics is feasible. In all cases, the combination of nanostructuring and catalytic additives is necessary to significantly enhance the reaction rates and limit the recrystallization of Mg upon hydrogen absorption/desorption to ensure cycling stability. Today, TMs and carbonaceous materials have been studied in particular, with a tangible improvement in reaction kinetics and cycling stability as well as a helpful understanding of the mechanisms. Based on this, research progress is expected to target new innovative catalysts combined with nano-engineering to tackle remaining issues for efficient reversible hydrogen storage in magnesium.

Mg-based alloys and compounds, on the other hand, can have markedly different thermodynamic stability with respect to pure or additive-modified MgH_2. In particular, the alloying of Mg with REs and TMs that form hydrides with both covalently bonded hydrogen (H^{cov}) and hydride ions (H^-) weakens the

chemical bonding of H^{cov}. In addition, some Mg based compounds show reversible hydrogen absorption and desorption at RT even though the gravimetric density becomes lower. The key issue to lower the thermodynamic stability is tuning the bonding nature with hydrogen. Therefore, an important future research should be to aim at understanding the effective elements or crystal structure that modify the bonding nature while retaining high hydrogen capacity.

TiFe intermetallic compound is considered a cheap and promising material for reversible hydrogen storage. It is especially appealing for large-scale stationary applications, owing to its reversible capacity up to 1.8 wt.% through two-step reactions in mild and safe conditions of pressure and temperature. The thermodynamics can be easily tailored by elemental substitution to favour activation, kinetics, cyclability and to adjust the plateau pressure at system conditions of application. Besides elemental substitution, improvements can be induced by nanosizing through ball milling or SPD techniques. Nowadays, applications of TiFe-based materials are mainly devoted to stationary storage and energy application in buildings to boost the green energy transition. Investigations that fully describe its hydriding and activation mechanisms have been recently proposed by *ab-initio* calculation and the CALPHAD approach.

High entropy alloys, despite the excellent hydrogen sorption properties reported for some of them, are not yet viable options for solid-state hydrogen storage systems due to reliance on expensive and/or critical elements. For example, the two lightest elements with the attractive VEC of 5, vanadium and niobium, are either very expensive (V) or are scored as highly critical both with respect to supply risk and economic importance (Nb). An important focus for further research should therefore be to develop new HEA without such elements while retaining superior hydrogen storage properties. Given the vast composition space potentially available for HEA synthesis, ML tools will serve as an invaluable guide in this quest.

For several reasons, Laves type hydrides will remain in focus of the research and development of intermetallic hydrides. The unique opportunity to tune their hydrogen storage performance based on the formation of the extended homogeneity ranges of the intermetallics allows their hydrogen storage performance to be tailored. Indeed, H_2 desorption plateau pressure spanning ten orders of magnitude can be realized, thus fitting the requirements for many applications. These include hydrogen getters, materials for hydrogen storage at ambient conditions, materials for efficient H_2 compression at output pressures of several hundred bars, and anode materials for metal hydride batteries operating in a challenging temperature range from below 0 °C to above 50 °C [347]. Pseudobinary Laves type intermetallics give an opportunity to achieve a continuous variation of hydrogen sorption properties, based on the interplay between the stability and crystal structure features of the original alloys. An excellent flatness and length of the absorption plateau pressure can be achieved and optimised based on the intrinsic behaviour of the alloys, including a contribution from elastic and electronic H–H interactions.

Data availability statement

The data that support the findings of this study are available upon reasonable request from the authors.

Acknowledgments

This paper was realised within the framework of the Hydrogen Technology Collaboration Programme (TCP) of the International Energy Agency (IEA) in Task 40 Energy Storage and Conversion Based on Hydrogen.

Some results reported in this publication were obtained thanks to funding from the Fuel Cells and Hydrogen 2 Joint Undertaking (JU) under Grant Agreement No. 826352, HyCARE project. The JU receives support from the European Union's Horizon 2020 research, Hydrogen Europe, Hydrogen Europe Research, innovation programme and Italy, France, Germany, Norway, which are all thankfully acknowledged.

V A Y, R V D, M V L, S S, J B V C and M D greatly acknowledge support from EU Horizon 2020 programme in the frame of the H2020-MSCA-RISE-2017 action, HYDRIDE4MOBILITY project, with Grant Agreement 778307.

J R A, J F F and F L from MIRE-group (UAM) acknowledge support from Ministerio de Ciencia, Innovación y Universidades (RTI2018-099794-B-I100).

B C H, M H S, and T R J gratefully acknowledge financial support from NordForsk Nordic Neutron Science Programme through the project FunHy (Grant Number 81942).

Portions of this work were funded through the Hydrogen Materials–Advanced Research Consortium (HyMARC) of the US Department of Energy (DOE), Office of Energy Efficiency and Renewable Energy, Hydrogen and Fuel Cell Technologies Office and performed under the auspices of the DOE by Lawrence Livermore National Laboratory (LLNL) under Contract DE-AC52-07NA27344. Additional funding for LLNL was provided through the Laboratory Directed Research and Development (LDRD) Program Project 20-SI-004. Computing resources were provided under the LLNL Institutional Computing Grand Challenge

program and the Innovative and Novel Computational Impact on Theory and Experiment (INCITE) program using resources of the Argonne Leadership Computing Facility, a US Department of Energy Office of Science User Facility supported under Contract DE-AC02-06CH11357.

Sandia National Laboratories is a multimission laboratory managed and operated by National Technology and Engineering Solutions of Sandia, LLC, a wholly owned subsidiary of Honeywell International, Inc., for the US Department of Energy's National Nuclear Security Administration under Contract DE-NA-0003525. The authors gratefully acknowledge funding from the US Department of Energy, Office of Energy Efficiency and Renewable Energy, Hydrogen and Fuel Cell Technologies Office, through the Hydrogen Storage Materials Advanced Research Consortium (HyMARC). This paper describes objective technical results and analysis. Any subjective views or opinions that might be expressed in the paper do not necessarily represent the views of the US Department of Energy or the United States Government.

C E B, M P P, and T D H (Curtin University) acknowledge financial support from the Australian Research Council for Grants DP150101708, LE0989180 and LE0775551.

T S (Shibaura Institute of Technology) acknowledges support from JST SICORP (JPMJSC 1802).

S O (Tohoku University) acknowledges support from MEXT/JSPS KAKENHI 'Hydrogenomics' (JP18H05513).

J-Y Suh and Y W Cho (KIST) acknowledge funding from National Research Foundation of Korea (NRF-2020M1A2A2080881).

S L (University of Nottingham) acknowledges support from EPSRC (EP/V042556/1) and the use of ARCHER2 supercomputer through membership of the UK's HPC Materials Chemistry Consortium funded by EPSRC (EP/R029431/1).

D B, M B, R Z S and I J (Ben Gurion University) acknowledge support from Israel Science Foundation Grant 745/15.

E R wishes to thank the Grand Technion Energy Program (GTEP) for continuing support.

ORCID iDs

Luca Pasquini https://orcid.org/0000-0001-8939-2204
Kouji Sakaki https://orcid.org/0000-0003-4781-1073
Etsuo Akiba https://orcid.org/0000-0002-9151-8926
Mark D Allendorf https://orcid.org/0000-0001-5645-8246
Ebert Alvares https://orcid.org/0000-0001-9002-3107
Josè R Ares https://orcid.org/0000-0001-5238-1800
Dotan Babai https://orcid.org/0000-0002-9408-3761
Marcello Baricco https://orcid.org/0000-0002-2856-9894
Josè Bellosta von Colbe https://orcid.org/0000-0002-3822-120X
Craig E Buckley https://orcid.org/0000-0002-3075-1863
Young Whan Cho https://orcid.org/0000-0001-9909-0082
Fermin Cuevas https://orcid.org/0000-0002-9055-5880
Patricia de Rango https://orcid.org/0000-0001-7416-5084
Erika Michela Dematteis https://orcid.org/0000-0002-3680-4196
Roman V Denys https://orcid.org/0000-0002-5479-8279
Martin Dornheim https://orcid.org/0000-0001-8491-435X
J F Fernández https://orcid.org/0000-0003-1224-3176
Arif Hariyadi https://orcid.org/0000-0003-4207-9127
Bjørn C Hauback https://orcid.org/0000-0002-2717-6941
Tae Wook Heo https://orcid.org/0000-0002-0765-3480
Michael Hirscher https://orcid.org/0000-0002-3143-2119
Terry D Humphries https://orcid.org/0000-0003-1015-4495
Jacques Huot https://orcid.org/0000-0002-8975-1569
Isaac Jacob https://orcid.org/0000-0003-2006-2834
Torben R Jensen https://orcid.org/0000-0002-4278-3221
Paul Jerabek https://orcid.org/0000-0002-2995-9755
Shin Young Kang https://orcid.org/0000-0001-9035-8169
Nathan Keilbart https://orcid.org/0000-0001-6219-7863
Hyunjeong Kim https://orcid.org/0000-0001-5018-3173
Michel Latroche https://orcid.org/0000-0002-8677-8280
F Leardini https://orcid.org/0000-0002-2864-2369
Haiwen Li https://orcid.org/0000-0001-7223-1754

Sanliang Ling https://orcid.org/0000-0003-1574-7476
Mykhaylo V Lototskyy https://orcid.org/0000-0001-8387-2856
Ryan Mullen https://orcid.org/0000-0002-2099-6955
Shin-ichi Orimo https://orcid.org/0000-0002-4216-0446
Mark Paskevicius https://orcid.org/0000-0003-2677-3434
Claudio Pistidda https://orcid.org/0000-0002-0706-6972
Marek Polanski https://orcid.org/0000-0003-0163-514X
Julián Puszkiel https://orcid.org/0000-0002-1547-997X
Eugen Rabkin https://orcid.org/0000-0001-5545-1261
Martin Sahlberg https://orcid.org/0000-0002-6486-5156
Sabrina Sartori https://orcid.org/0000-0002-9952-6488
Archa Santhosh https://orcid.org/0000-0002-1441-4998
Toyoto Sato https://orcid.org/0000-0002-0527-1235
Roni Z Shneck https://orcid.org/0000-0002-5802-1352
Magnus H Sørby https://orcid.org/0000-0002-8878-3331
Vitalie Stavila https://orcid.org/0000-0003-0981-0432
Jin-Yoo Suh https://orcid.org/0000-0003-3786-6652
Suwarno Suwarno https://orcid.org/0000-0003-1790-0868
Liwen F Wan https://orcid.org/0000-0002-5391-0804
Colin J Webb https://orcid.org/0000-0001-6659-0726
Matthew Witman https://orcid.org/0000-0001-6263-5114
ChuBin Wan https://orcid.org/0000-0002-9214-0283
Brandon C Wood https://orcid.org/0000-0002-1450-9719
Volodymyr A Yartys https://orcid.org/0000-0003-4207-9127

References

[1] European Commission 2050 long-term strategy (available at: https://ec.europa.eu/clima/policies/strategies/2050_en)
[2] Hydrogen Technology Collaboration Programme (available at: www.ieahydrogen.org/)
[3] Task 40: Energy Storage and Conversion Based on Hydrogen (available at: www.ieahydrogen.org/task/task-40-energy-storage-and-conversion-based-on-hydrogen/)
[4] Crivello J-C *et al* 2016 Review of magnesium hydride-based materials: development and optimisation *Appl. Phys.* A **122** 97
[5] Yartys V A *et al* 2019 Magnesium based materials for hydrogen based energy storage: past, present and future *Int. J. Hydrog. Energy* **44** 7809–59
[6] Hirscher M *et al* 2020 Materials for hydrogen-based energy storage—past, recent progress and future outlook *J. Alloys Compd.* **827** 153548
[7] Gross K J *et al* 2012 Recommended best practices for the characterization of storage properties of hydrogen storage materials *US DOE Hydrogen Program document V3.34* (available at: www1.eere.energy.gov/hydrogenandfuelcells/pdfs/best_practices_hydrogen_storage.pdf)
[8] Lide D R 2007 CRC Handbook of Chemistry and Physics, 88th ed Editor-in-Chief: David R Lide (National Institute of Standards and Technology) CRC Press/Taylor & Francis Group: Boca Raton, FL. 2007. 2640 pp $139.95. ISBN 0-8493-0488-1 *J. Am. Chem. Soc.* **130** 382
[9] Paskevicius M, Sheppard D A and Buckley C E 2010 Thermodynamic changes in mechanochemically synthesized magnesium hydride nanoparticles *J. Am. Chem. Soc.* **132** 5077–83
[10] Buckley A C, Carter D J, Sheppard D A and Buckley C E 2012 Density functional theory calculations of magnesium hydride: a comparison of bulk and nanoparticle thermodynamics *J. Phys. Chem.* C **116** 17985–90
[11] Libowitz G G, Hayes H F and Gibb T R P 1958 The system zirconium–nickel and hydrogen *J. Phys. Chem.* **62** 76–79
[12] Reilly J J and Wiswall R H 1967 Reaction of hydrogen with alloys of magnesium and copper *Inorg. Chem.* **6** 2220–3
[13] Reilly J J and Wiswall R H 1968 The reaction of hydrogen with alloys of magnesium and nickel and the formation of Mg_2NiH_4 *Inorg. Chem.* **7** 2254–6
[14] Reilly J J and Wiswall R H 1974 Formation and properties of iron titanium hydride *Inorg. Chem.* **13** 218–22
[15] van Vucht J H N, Kuijpers F A and Bruning H C A M 1970 Reversible room-temperature absorption of large quantities of hydrogen by intermetallic compounds *Philips Res. Rep.* **25** 133–40
[16] David W I F 2011 Effective hydrogen storage: a strategic chemistry challenge *Faraday Discuss.* **151** 399–414
[17] Rittmeyer P and Wietelmann U 1993 *Ullmann's Encyclopedia of Industrial Chemistry Fifth, Completely Revised Edition, A13* (Weinheim: Wiley-VCH)
pp 199–299
[18] Huot J 2010 Metal hydrides *Handbook of Hydrogen Storage: New Materials for Future Energy Storage* (Weinheim: Wiley-VCH) Hirscher M pp 81–116
[19] van Mal H H, Buschow K H J and Miedema A R 1974 Hydrogen absorption in $LaNi_5$ and related compounds: experimental observations and their explanation *J. Less-Common Met.* **35** 65–76
[20] Wood B C, Heo T W, Kang S, Wan L F and Li S 2020 Beyond idealized models of nanoscale metal hydrides for hydrogen storage *Ind. Eng. Chem. Res.* **59** 5786–96
[21] Heo T W, Colas K B, Motta A T and Chen L-Q 2019 A phase-field model for hydride formation in polycrystalline metals: application to δ-hydride in zirconium alloys *Acta Mater.* **181** 262–77
[22] Shi R, Heo T W, Wood B C and Wang Y 2020 Critical nuclei at hetero-phase interfaces *Acta Mater.* **200** 510–25

[23] Kim D, Koh J, Kang S, Heo T W, Wood B C, Cho E S and Han S M 2021 Chemomechanical effect of reduced graphene oxide encapsulation on hydrogen storage performance of Pd nanoparticles *J. Mater. Chem.* A **9** 11641–50
[24] Kim D, Han D J, Heo T W, Kang S, Wood B C, Lee J, Cho E S and Lee B J 2022 Enhancement of effective thermal conductivity of rGO/Mg nanocomposite packed beds *Int. J. Heat Mass Transfer* **192** 122891
[25] Milanese C *et al* 2019 Complex hydrides for energy storage *Int. J. Hydrog. Energy* **44** 7860–74
[26] Bourgeois N, Crivello J-C, Cenedese P and Joubert J-M 2017 Systematic first-principles study of binary metal hydrides *ACS Comb. Sci.* **19** 513–23
[27] Joubert J-M 2012 CALPHAD modeling of metal–hydrogen systems: a review *JOM* **64** 1438–47
[28] Joubert J-M 2015 Thermodynamic modelling of metal–hydrogen systems using the Calphad method *J. Alloys Compd.* **645** S379–83
[29] Liu Z-K 2018 Ocean of data: integrating first-principles calculations and CALPHAD modeling with machine learning *J. Phase Equilibria Diffus.* **39** 635–49
[30] Pottmaier D, Pinatel E R, Vitillo J G, Garroni S, Orlova M, Baró M D, Vaughan G B M, Fichtner M, Lohstroh W and Baricco M 2011 Structure and thermodynamic properties of the $NaMgH_3$ perovskite: a comprehensive study *Chem. Mater.* **23** 2317–26
[31] Pinatel E R, Corno M, Ugliengo P and Baricco M 2014 Effects of metastability on hydrogen sorption in fluorine substituted hydrides *J. Alloys Compd.* **615** S706–10
[32] Fonneløp J E, Corno M, Grove H, Pinatel E, Sørby M H, Ugliengo P, Baricco M and Hauback B C 2011 Experimental and computational investigations on the AlH_3/AlF_3 system *J. Alloys Compd.* **509** 10–14
[33] Baldissin D, Urgnani J, Palumbo M, Gagliano S and Baricco M 2008 Thermofluidodynamic modelling of hydrogen absorption and desorption in a $LaNi_{4.8}Al_{0.2}$ hydride bed *Present. MH2008 Int. Symp. Met. Syst. Reykjavik, Icel.* (23–28 June)
[34] Dematteis E M, Barale J, Corno M, Sciullo A, Baricco M and Rizzi P 2021 Solid-state hydrogen storage systems and the relevance of a gender perspective *Energies* **14** 6158
[35] Baricco M, Palumbo M, Pinatel E, Corno M and Ugliengo P 2010 Thermodynamic database for hydrogen storage materials *Adv. Sci. Technol.* **72** 213–8
[36] Urgnani J, di Chio M, Palumbo M, Feuerbacher M, Fernandez J F, Leardini F and Baricco M 2009 Hydrogen absorption and desorption in rapidly solidified Mg–Al alloys *J. Phys.: Conf. Ser.* **144** 012016
[37] Palumbo M, Torres F J, Ares J R, Pisani C, Fernandez J F and Baricco M 2007 Thermodynamic and *ab initio* investigation of the Al–H–Mg system *Calphad* **31** 457–67
[38] Alvares E, Jerabek P, Shang Y, Santhosh A, Pistidda C, Heo T W, Sundman B and Dornheim M 2022 Modeling the thermodynamics of the FeTi hydrogenation under para-equilibrium: An *ab-initio* and experimental study *Calphad* **77** 102426
[39] Palumbo M, Urgnani J, Baldissin D, Battezzati L and Baricco M 2009 Thermodynamic assessment of the H–La–Ni system *Calphad* **33** 162–9
[40] Pinatel E R, Palumbo M, Massimino F, Rizzi P and Baricco M 2015 Hydrogen sorption in the $LaNi_{5-x}Al_x$-H system ($0 \leqslant x \leqslant 1$) *Intermetallics* **62** 7–16
[41] Endo N, Saitoh H, Machida A and Katayama Y 2013 Formation of BCC TiFe hydride under high hydrogen pressure *Int. J. Hydrog. Energy* **38** 6726–9
[42] Yamanaka K, Saito H and Someno M 1975 Hydride formation of intermetallic compounds of titanium-iron, -cobalt, -nickel and -copper *Nippon Kagaku Kaishi* **1975** 1267–72
[43] Sundman B, Kattner U R, Palumbo M and Fries S G 2015 OpenCalphad—a free thermodynamic software *Integr. Mater. Manuf. Innov.* **4** 1–15
[44] Sundman B, Kattner U R, Sigli C, Stratmann M, Le Tellier R, Palumbo M and Fries S G 2016 The OpenCalphad thermodynamic software interface *Comput. Mater. Sci.* **125** 188–96
[45] Lototskyy M V, Tolj I, Parsons A, Smith F, Sita C and Linkov V 2016 Performance of electric forklift with low-temperature polymer exchange membrane fuel cell power module and metal hydride hydrogen storage extension tank *J. Power Sources* **316** 239–50
[46] Lototsky M V, Yartys V A, Marinin V S and Lototsky N M 2003 Modelling of phase equilibria in metal–hydrogen systems *J. Alloys Compd.* **356–357** 27–31
[47] Lototskyy M V, Yartys V A, Tarasov B P, Davids M W, Denys R V and Tai S 2021 Modelling of metal hydride hydrogen compressors from thermodynamics of hydrogen—metal interactions viewpoint: part I. Assessment of the performance of metal hydride materials *Int. J. Hydrog. Energy* **46** 2330–8
[48] Mohammadshahi S S, Gray E M and Webb C J 2016 A review of mathematical modelling of metal-hydride systems for hydrogen storage applications *Int. J. Hydrog. Energy* **41** 3470–84
[49] Chabane D, Harel F, Djerdir A, Candusso D, Elkedim O and Fenineche N 2019 Energetic modeling, simulation and experimental of hydrogen desorption in a hydride tank *Int. J. Hydrog. Energy* **44** 1034–46
[50] Chibani A, Merouani S, Bougriou C and Hamadi L 2020 Heat and mass transfer during the storage of hydrogen in $LaNi_5$-based metal hydride: 2D simulation results for a large scale, multi-pipes fixed-bed reactor *Int. J. Heat Mass Transfer* **147** 118939
[51] Chandra S, Sharma P, Muthukumar P and Tatiparti S S V 2020 Modeling and numerical simulation of a 5 kg $LaNi_5$-based hydrogen storage reactor with internal conical fins *Int. J. Hydrog. Energy* **45** 8794–809
[52] Lototskyy M V 2016 New model of phase equilibria in metal—hydrogen systems: features and software *Int. J. Hydrog. Energy* **41** 2739–61
[53] Ledovskikh A V, Danilov D L, Vliex M and Notten P H L 2016 Modeling and experimental verification of the thermodynamic properties of hydrogen storage materials *Int. J. Hydrog. Energy* **41** 3904–18
[54] Wu G-X, Peng W-J and Zhang J-Y 2017 Statistic thermodynamic model of hydrogen absorption on metal powders *Wuli Huaxue Xuebao/Acta Phys.-Chim. Sin.* **33** 1108–13
[55] Bajahzar A, Bouzid M, Briki C, Nasri F, Belmabrouk H and Jemni A 2020 Experimental and numerical study of the isotherms and determination of physicochemical parameters of the hydrogen absorption/desorption process by the metal hydrides *Int. J. Hydrog. Energy* **45** 15281–93
[56] Kierstead H A 1980 A theory of multiplateau hydrogen absorption isotherms *J. Less-Common Met.* **71** 303–9
[57] Kierstead H A 1984 A theory of hydrogen absorption with interactions *J. Less-Common Met.* **96** 141–52
[58] Fujitani S, Nakamura H, Furukawa A, Nasako K, Satoh K, Imoto T, Saito T and Yonezu I 1993 A method for numerical expressions of P-C isotherms of hydrogen-absorbing alloys *Z. Phys. Chem.* **179** 27–33
[59] Park C-N, Luo S and Flanagan T B 2004 Analysis of sloping plateaux in alloys and intermetallic hydrides: I. Diagnostic features *J. Alloys Compd.* **384** 203–7

[60] Skripnyuk V M and Rabkin E 2012 Mg_3Cd: a model alloy for studying the destabilization of magnesium hydride *Int. J. Hydrog. Energy* **37** 10724–32
[61] Sharma A, Hickman J, Gazit N, Rabkin E and Mishin Y 2018 Nickel nanoparticles set a new record of strength *Nat. Commun.* **9** 4102
[62] Issa I, Amodeo J, Réthoré J, Joly-Pottuz L, Esnouf C, Morthomas J, Perez M, Chevalier J and Masenelli-Varlot K 2015 *In situ* investigation of MgO nanocube deformation at room temperature *Acta Mater.* **86** 295–304
[63] Wendlandt W W 1974 *Thermal Methods of Analysis* (New York: Wiley)
[64] Spivak L V, Shchepina N E and Dyshluyk M A 2020 General regularities of thermal decomposition of transition metal dihydrides in a medium with low hydrogen partial pressure *Int. J. Hydrog. Energy* **45** 25075–85
[65] Evard E, Gabis I and Yartys V A 2010 Kinetics of hydrogen evolution from MgH_2: experimental studies, mechanism and modelling *Int. J. Hydrog. Energy* **35** 9060–9
[66] Lototskyy M, Sibanyoni J M, Denys R V, Williams M, Pollet B G and Yartys V A 2013 Magnesium-carbon hydrogen storage hybrid materials produced by reactive ball milling in hydrogen *Carbon* **57** 146–60
[67] Gabis I, Evard E, Voyt A, Chernov I and Zaika Y 2003 Kinetics of decomposition of erbium hydride *J. Alloys Compd.* **356–357** 353–7
[68] Suwarno S, Lototskyy M V and Yartys V A 2020 Thermal desorption spectroscopy studies of hydrogen desorption from rare earth metal trihydrides REH_3 (RE = Dy, Ho, Er) *J. Alloys Compd.* **842** 155530
[69] Kissinger H E 1957 Reaction kinetics in differential thermal analysis *Anal. Chem.* **29** 1702–6
[70] Blaine R L and Kissinger H E 2012 Homer Kissinger and the Kissinger equation *Thermochim. Acta* **540** 1–6
[71] Boswell P G 1980 On the calculation of activation energies using a modified Kissinger method *J. Therm. Anal.* **18** 353–8
[72] Agresti F 2013 An extended Kissinger equation for near equilibrium solid–gas heterogeneous transformations *Thermochim. Acta* **566** 214–7
[73] Lototskyy M, Denys R, Nyamsi S N, Bessarabskaia I and Yartys V 2018 Modelling of hydrogen thermal desorption spectra *Mater. Today Proc.* **5** 10440–9
[74] Dimitra K and Konstantinos C 2021 Nonisothermal crystallization kinetics: studying the validity of different Johnson–Mehl–Avrami–Erofeev–Kolmogorov (JMAEK) based equations *Thermochim. Acta* **704** 179030
[75] Aghili A 2021 Representation and evaluation of the Arrhenius and general temperature integrals by special functions *Thermochim. Acta* **705** 179034
[76] Barale J, Deledda S, Dematteis E M, Sørby M H, Baricco M and Hauback B C 2020 Synthesis and characterization of magnesium-iron-cobalt complex hydrides *Sci. Rep.* **10** 9000
[77] Zhang Y, Wei X, Zhang W, Yuan Z, Gao J, Qi Y and Ren H 2020 Effect of milling duration on hydrogen storage thermodynamics and kinetics of Mg-based alloy *Int. J. Hydrog. Energy* **45** 33832–45
[78] Zhang Y, Sun H, Zhang W, Yuan Z, Wei X, Gao J and Ren H 2021 Improvement of substituting La with Ce on hydrogen storage thermodynamics and kinetics of Mg-based alloys *Int. J. Hydrog. Energy* **46** 28719–33
[79] Šesták J and Berggren G 1971 Study of the kinetics of the mechanism of solid-state reactions at increasing temperatures *Thermochim. Acta* **3** 1–12
[80] Gibson R L, Simmons M J H, Hugh Stitt E, West J, Wilkinson S K and Gallen R W 2021 Kinetic modelling of thermal processes using a modified Sestak-Berggren equation *Chem. Eng. J.* **408** 127318
[81] Suryanarayana C 2001 Mechanical alloying and milling *Prog. Mater. Sci.* **46** 1–184
[82] Klassen T, Herr U and Averback R S 1997 Ball milling of systems with positive heat of mixing: effect of temperature in Ag–Cu *Acta Mater.* **45** 2921–30
[83] Gaffet E, Harmelin M and Faudot F 1993 Far-from-equilibrium phase transition induced by mechanical alloying in the Cu–Fe system *J. Alloys Compd.* **194** 23–30
[84] Huot J *et al* 2019 Mechanochemistry of metal hydrides: recent advances *Materials* **12** 2778
[85] Liu H, Sun P, Bowman R C, Fang Z Z, Liu Y and Zhou C 2020 Effect of air exposure on hydrogen storage properties of catalyzed magnesium hydride *J. Power Sources* **454** 227936
[86] Vincent S D and Huot J 2011 Effect of air contamination on ball milling and cold rolling of magnesium hydride *J. Alloys Compd.* **509** L175–9
[87] Estrin Y and Vinogradov A 2013 Extreme grain refinement by severe plastic deformation: a wealth of challenging science *Acta Mater.* **61** 782–817
[88] Ivanisenko Y, Kulagin R, Fedorov V, Mazilkin A, Scherer T, Baretzky B and Hahn H 2016 High pressure torsion extrusion as a new severe plastic deformation process *Mater. Sci. Eng.* A **664** 247–56
[89] Omranpour B, Kommel L, Garcia Sanchez E, Ivanisenko Y and Huot J 2019 Enhancement of hydrogen storage in metals by using a new technique in severe plastic deformations *Key Eng. Mater.* **799** 173–8
[90] Brown T L, Swaminathan S, Chandrasekar S, Compton W D, King A H and Trumble K P 2002 Low-cost manufacturing process for nanostructured metals and alloys *J. Mater. Res.* **17** 2484–8
[91] Huot J and Tousignant M 2019 Effect of cold rolling on metal hydrides *Mater. Trans.* **60** 1571–6
[92] Asselli A A C, Leiva D R, Cozentino G H, Floriano R, Huot J, Ishikawa T T and Botta W J 2014 Hydrogen storage properties of MgH_2 processed by cold forging *J. Alloys Compd.* **615** S719–24
[93] de Rango P, Wen J, Skryabina N, Laversenne L, Fruchart D and Borges M 2020 Hydrogen storage properties of Mg–Ni alloys processed by fast forging *Energies* **13** 3509
[94] Sandrock G D 1978 The metallurgy and production of rechargeable hydrides *Hydrides for Energy Storage; Proceedings of the International Symposium* (*Geilo, Norway, 14–19 August 1977*) (Oxford: Pergamon Press Ltd) pp 353–93
[95] Fadonougbo J O, Kim H-J, Suh B-C, Suh J-Y, Lee Y-S, Shim J-H, Yim C D and Cho Y W 2020 Kinetics and thermodynamics of near eutectic Mg–Mg_2Ni composites produced by casting process *Int. J. Hydrog. Energy* **45** 29009–22
[96] de Jongh P E, Allendorf M, Vajo J J and Zlotea C 2013 Nanoconfined light metal hydrides for reversible hydrogen storage *MRS Bull.* **38** 488–94
[97] Jeon K-J, Moon H R, Ruminski A M, Jiang B, Kisielowski C, Bardhan R and Urban J J 2011 Air-stable magnesium nanocomposites provide rapid and high-capacity hydrogen storage without using heavy-metal catalysts *Nat. Mater.* **10** 286–90
[98] Pasquini L, Callini E, Brighi M, Boscherini F, Montone A, Jensen T R, Maurizio C, Antisari M V and Bonetti E 2011 Magnesium nanoparticles with transition metal decoration for hydrogen storage *J. Nanopart. Res.* **13** 5727–37

[99] Calizzi M, Venturi F, Ponthieu M, Cuevas F, Morandi V, Perkisas T, Bals S and Pasquini L 2016 Gas-phase synthesis of Mg–Ti nanoparticles for solid-state hydrogen storage *Phys. Chem. Chem. Phys.* **18** 141–8
[100] Patelli N, Migliori A, Morandi V and Pasquini L 2020 Interfaces within biphasic nanoparticles give a boost to magnesium-based hydrogen storage *Nano Energy* **20** 1325–33
[101] Patelli N, Migliori A and Pasquini L 2019 Reversible metal-hydride transformation in Mg–Ti–H nanoparticles at remarkably low temperatures *ChemPhysChem* **20** 1325–33
[102] Holleman A F and Wiberg E 1995 *Inorganic Chemistry* (New York: Academic)
[103] Møller K T, Sheppard D, Ravnsbæk D B, Buckley C E, Akiba E, Li H-W and Jensen T R 2017 Complex metal hydrides for hydrogen, thermal and electrochemical energy storage *Energies* **10** 1645
[104] Sheppard D A *et al* 2016 Metal hydrides for concentrating solar thermal power energy storage *Appl. Phys.* A **122** 395
[105] Pardo P, Deydier A, Anxionnaz-Minvielle Z, Rougé S, Cabassud M and Cognet P 2014 A review on high temperature thermochemical heat energy storage *Renew. Sustain. Energy Rev.* **32** 591–610
[106] Javadian P, Sheppard D A, Jensen T R and Buckley C E 2016 Destabilization of lithium hydride and the thermodynamic assessment of the Li–Al–H system for solar thermal energy storage *RSC Adv.* **6** 94927–33
[107] Cheng X-B, Zhang R, Zhao C-Z and Zhang Q 2017 Toward safe lithium metal anode in rechargeable batteries: a review *Chem. Rev.* **117** 10403–73
[108] Jensen T R, Andreasen A, Vegge T, Andreasen J W, Ståhl K, Pedersen A S, Nielsen M M, Molenbroek A M and Besenbacher F 2006 Dehydrogenation kinetics of pure and nickel-doped magnesium hydride investigated by *in situ* time-resolved powder x-ray diffraction *Int. J. Hydrog. Energy* **31** 2052–62
[109] Huot J, Liang G, Boily S, van Neste A and Schulz R 1999 Structural study and hydrogen sorption kinetics of ball-milled magnesium hydride *J. Alloys Compd.* **293** 495–500
[110] Jander W 1927 Reaktionen im festen Zustande bei höheren Temperaturen. Reaktionsgeschwindigkeiten endotherm verlaufender Umsetzungen *Z. Anorg. Allg. Chem.* **163** 1–30
[111] Kempen A T W, Sommer F and Mittemeijer E J 2002 Determination and interpretation of isothermal and non-isothermal transformation kinetics; the effective activation energies in terms of nucleation and growth *J. Mater. Sci.* **37** 1321–32
[112] Montone A, Aurora A, Gattia D M and Antisari M V 2010 On the barriers limiting the reaction kinetics between catalysed Mg and hydrogen *Scr. Mater.* **4** 456–9
[113] Baran A and Polański M 2020 Magnesium-based materials for hydrogen storage—a scope review *Materials* **13** 3993
[114] Alsabawi K, Webb T A, Gray E M A and Webb C J 2017 Kinetic enhancement of the sorption properties of MgH_2 with the additive titanium isopropoxide *Int. J. Hydrog. Energy* **42** 5227–34
[115] Webb C J 2015 A review of catalyst-enhanced magnesium hydride as a hydrogen storage material *J. Phys. Chem. Solids* **84** 96–106
[116] Alsabawi K, Webb T A, Gray E M and Webb C J 2015 The effect of C_{60} additive on magnesium hydride for hydrogen storage *Int. J. Hydrog. Energy* **33** 10508–15
[117] Pitt M, Paskevicius M, Webb C, Sheppard D, Buckley C and Gray E 2012 The synthesis of nanoscopic Ti based alloys and their effects on the MgH_2 system compared with the $MgH_2 + 0.01Nb_2O_5$ benchmark *Int. J. Hydrog. Energy* **37** 4227–37
[118] Oelerich W, Klassen T and Bormann R 2001 Metal oxides as catalysts for improved hydrogen sorption in nanocrystalline Mg-based materials *J. Alloys Compd.* **315** 237–42
[119] Aguey-Zinsou K-F, Nicolaisen T, Fernandez J R A, Klassen T and Bormann R 2007 Effect of nanosized oxides on MgH_2 (de)hydriding kinetics *J. Alloys Compd.* **434–435** 738–42
[120] Dornheim M, Eigen N, Barkhordarian G, Klassen T and Bormann R 2006 Tailoring hydrogen storage materials towards application *Adv. Eng. Mater.* **8** 377–85
[121] Janot R, Cuevas F, Latroche M and Percheron-Guégan A 2006 Influence of crystallinity on the structural and hydrogenation properties of Mg_2X phases (X = Ni, Si, Ge, Sn) *Intermetallics* **2** 163–9
[122] Fernandez J F, Widom M, Cuevas F, Ares J R, Bodega J, Leardini F, Mihalkovič M and Sánchez C 2011 First-principles phase stability calculations and estimation of finite temperature effects on pseudo-binary $Mg_6(Pd_xNi_{1-x})$ compounds *Intermetallics* **19** 502–10
[123] Ares J-R, Nevshupa R, Muñoz-Cortés E, Sánchez C, Leardini F, Ferrer I-J, Minh Huy Tran V, Aguey-zinsou F and Fernández J-F 2019 Unconventional approaches to hydrogen sorption reactions: non-thermal and non-straightforward thermally driven methods *ChemPhysChem* **20** 1248–60
[124] Nevshupa R, Ares J R, Fernández J F, del Campo A and Roman E 2015 Tribochemical decomposition of light ionic hydrides at room temperature *J. Phys. Chem. Lett.* **6** 2780–5
[125] Sun Y and Aguey-Zinsou K-F 2018 Light-activated hydrogen storage in Mg, LiH and $NaAlH_4$ *ChemPlusChem* **83** 904–8
[126] Skripnyuk V M, Rabkin E, Estrin Y and Lapovok R 2004 The effect of ball milling and equal channel angular pressing on the hydrogen absorption/desorption properties of Mg–4.95 wt% Zn–0.71 wt% Zr (ZK60) alloy *Acta Mater.* **52** 405–14
[127] Rabkin E, Skripnyuk V and Estrin Y 2019 Ultrafine-grained magnesium alloys for hydrogen storage obtained by severe plastic deformation *Front. Mater.* **6** 240
[128] Berube V, Chen G and Dresselhaus M S 2008 Impact of nanostructuring on the enthalpy of formation of metal hydrides *Int. J. Hydrog. Energy* **33** 4122–31
[129] Edalati K *et al* 2018 Design and synthesis of a magnesium alloy for room temperature hydrogen storage *Acta Mater.* **149** 88–96
[130] Huang S-J, Rajagopal V and Ali A N 2019 Influence of the ECAP and HEBM processes and the addition of Ni catalyst on the hydrogen storage properties of AZ31-x Ni (x = 0,2,4) alloy *Int. J. Hydrog. Energy* **44** 1047–58
[131] Osorio-García M, Suárez-Alcántara K, Todaka Y, Tejeda-Ochoa A, Herrera-Ramírez M, Hernández-Silva O, Cruz-Gandarilla F and Cabañas-Moreno J G 2021 Low-temperature hydrogenation of Mg–Ni–Nb_2O_5 alloy processed by high-pressure torsion *J. Alloys Compd.* **878** 160309
[132] Leiva D R, Jorge Jr. A M, Ishikawa T T and Botta W J 2019 Hydrogen storage in Mg and Mg-based alloys and composites processed by severe plastic deformation *Mater. Trans.* **60** 1561–70
[133] Skryabina N *et al* 2019 Microstructure optimization of Mg-alloys by the ECAP process including numerical simulation, SPD treatments, characterization, and hydrogen sorption properties *Molecules* **24** 89
[134] Grill A, Horky J, Panigrahi A, Krexner G and Zehetbauer M 2015 Long-term hydrogen storage in Mg and ZK60 after severe plastic deformation *Int. J. Hydrog. Energy* **40** 17144–52

[135] Wen J, de Rango P, Allain N, Laversenne L and Grosdidier T 2020 Improving hydrogen storage performance of Mg-based alloy through microstructure optimization *J. Power Sources* **480** 228823

[136] Løken S, Solberg J K, Maehlen J P, Denys R V, Lototsky M V, Tarasov B P and Yartys V A 2007 Nanostructured Mg–Mm–Ni hydrogen storage alloy: structure–properties relationship *J. Alloys Compd.* **446–7** 114–20

[137] Denys R V, Riabov A B, Maehlen J P, Lototsky M V, Solberg J K and Yartys V A 2009 *In situ* synchrotron x-ray diffraction studies of hydrogen desorption and absorption properties of Mg and Mg–Mm–Ni after reactive ball milling in hydrogen *Acta Mater.* **57** 3989–4000

[138] Tran X Q, McDonald S D, Gu Q, Yamamoto T, Shigematsu K, Aso K, Tanaka E, Matsumura S and Nogita K 2017 *In-situ* investigation of the hydrogen release mechanism in bulk Mg_2NiH_4 *J. Power Sources* **341** 130–8

[139] Crivello J-C, Zhang J and Latroche M 2011 Structural stability of AB_y phases in the (La,Mg)ÀNi system obtained by density functional theory calculations *J. Phys. Chem.* C **115** 25470–8

[140] Yartys V, Noreus D and Latroche M 2016 Metal hydrides as negative electrode materials for Ni–MH batteries *Appl. Phys.* A **122** 43

[141] Denys R V and Yartys V A 2011 Effect of magnesium on the crystal structure and thermodynamics of the $La_{3-x}Mg_xNi_9$ hydrides *J. Alloys Compd.* **509** S540–8

[142] Denys R V, Yartys V A, Gray E M A and Webb C J 2015 $LaNi_5$-assisted hydrogenation of $MgNi_2$ in the hybrid structures of $La_{1.09}Mg_{1.91}Ni_9D_{9.5}$ and $La_{0.91}Mg_{2.09}Ni_9D_{9.4}$ *Energies* **8** 3198–211

[143] Yartys V A *et al* 2015 Hydrogen-assisted phase transition in a trihydride $MgNi_2H_3$ synthesized at high H_2 pressures: thermodynamics, crystallographic and electronic structures *Acta Mater.* **82** 316–27

[144] Yartys V A, Antonov V E, Chernyshov D, Crivello J-C, Denys R V, Fedotov V K, Gupta M, Kulakov V I, Latroche M and Sheptyakov D 2015 Structure and chemical bonding in $MgNi_2H_3$ from combined high resolution synchrotron and neutron diffraction studies and *ab initio* electronic structure calculations *Acta Mater.* **98** 416–22

[145] Zhang J, Charbonnier V, Madern N, Monnier J and Latroche M 2021 Improvement of reversible H storage capacity by fine tuning of the composition in the pseudo-binary systems $A_{2-x}La_xNi_7$ (A = Gd, Sm, Y, Mg) *J. Alloys Compd.* **852** 157008

[146] Charbonnier V, Madern N, Monnier J, Zhang J, Paul-Boncour V and Latroche M 2020 Thermodynamic and corrosion study of $Sm_{1-x}Mg_xNi_y$ (y = 3.5 or 3.8) compounds forming reversible hydrides *Int. J. Hydrog. Energy* **45** 11686–94

[147] Wan C B, Hu W, Denys R V, Nwakwuo C C, Solberg J K and Yartys V A 2021 Effect of Mg content in the $La_{3-x}Mg_xNi_9$ battery anode alloys on the structural, hydrogen storage and electrochemical properties *J. Alloys Compd.* **856** 157443

[148] Wan C B, Denys R V and Yartys V A 2021 Towards understanding the influence of Mg content on phase transformations in the $La_{3-x}Mg_xNi_9$ alloys by *in-situ* neutron powder diffraction study *Prog. Nat. Sci.: Mater. Int.* **31** 698–704

[149] Aono K, Orimo S and Fujii H 2000 Structural and hydriding properties of $MgYNi_4$:: a new intermetallic compound with C15*b*-type Laves phase structure *J. Alloys Compd.* **309** L1–L4

[150] Kadir K, Noréus D and Yamashita I 2002 Structural determination of $AMgNi_4$ (where A = Ca, La, Ce, Pr, Nd and Y) in the $AuBe_5$ type structure *J. Alloys Compd.* **345** 140–3

[151] Sato T *et al* 2020 Crystal structural investigations for understanding the hydrogen storage properties of $YMgNi_4$-based alloys *ACS Omega* **5** 31192–8

[152] Guénée L, Favre-Nicolin V and Yvon K 2003 Synthesis, crystal structure and hydrogenation properties of the ternary compounds $LaNi_4Mg$ and $NdNi_4Mg$ *J. Alloys Compd.* **348** 129–37

[153] Terashita N, Sakaki K, Tsunokake S, Nakamura Y and Akiba E 2012 Hydrogenation properties of ternary intermetallic compounds $Mg_{2-x}Pr_xNi_4$ *Mater. Trans.* **53** 513–7

[154] Chotard J-N, Sheptyakov D and Yvon K 2008 Hydrogen induced site depopulation in the $LaMgNi_4$-hydrogen system *Z. Kristallogr.* **223** 690–6

[155] Roquefere J-G, Matar S F, Huot J and Bobet J-L 2009 X-ray/neutron diffraction studies and *ab initio* electronic structure of $CeMgNi_4$ and its hydride *Solid State Sci.* **11** 1971–8

[156] Sakaki K, Terashita N, Tsunokake S, Nakamura Y and Akiba E 2011 *In situ* x-ray diffraction study of phase transformation of $Mg_{2-x}Pr_xNi_4$ during hydrogenation and dehydrogenation (x = 0.6 and 1.0) *J. Phys. Chem.* C **116** 1401–7

[157] Sakaki K, Terashita N, Tsunokake S, Nakamura Y and Akiba E 2012 Effect of rare earth elements and alloy composition on hydrogenation properties and crystal structures of hydrides in $Mg_{2-x}RE_xNi_4$ *J. Phys. Chem.* C **116** 19156–63

[158] Sakaki K, Terashita N, Kim H, Proffen T, Majzoub E H, Tsunokake S, Nakamura Y and Akiba E 2013 Crystal structure and local structure of $Mg_{2-x}Pr_xNi_4$ (x = 0.6 and 1.0) deuteride using *in situ* neutron total scattering *Inorg. Chem.* **52** 7010–9

[159] Shtender V V, Denys R V, Paul-Boncour V, Riabov A B and Zavaliy I Y 2014 Hydrogenation properties and crystal structure of $YMgT_4$ (T = Co, Ni, Cu) compounds *J. Alloys Compd.* **603** 7–13

[160] Denys R V, Riabov A B, Černý R, Kovalchuk I V and Zavaliy I Y 2012 New $CeMgCo_4$ and Ce_2MgCo_9 compounds: hydrogenation properties and crystal structure of hydrides *J. Solid State Chem.* **187** 1–6

[161] Shtender V V, Denys R V, Paul-Boncour V, Verbovytskyy Y V and Zavaliy I Y 2015 Effect of Co substitution on hydrogenation and magnetic properties of $NdMgNi_4$ alloy *J. Alloys Compd.* **639** 526–32

[162] Yartys V A, Denys R V, Hauback B, Fjellvåg H, Bulyk I, Riabov A and Kalychak Y 2002 Short hydrogen–hydrogen separations in novel intermetallic hydrides, $RE_3Ni_3In_3D_4$ (RE = La, Ce and Nd) *J. Alloys Compd.* **330–332** 132–40

[163] Klein R A, Balderas-Xicohténcatl R, Maehlen J P, Udovic T J, Brown C M, Delaplane R, Cheng Y, Denys R V, Ramirez-Cuesta A J and Yartys V A 2022 Neutron vibrational spectroscopic evidence for short H···H contacts in the $RNiInH_{1.4;\,1.6}$ (R = Ce, La) metal hydride *J. Alloys Compd.* **894** 162381

[164] Borgschulte A, Terreni J, Billeter E, Daemen L, Cheng Y, Pandey A, Łodziana Z, Hemley R J and Ramirez-Cuesta A J 2020 Inelastic neutron scattering evidence for anomalous H–H distances in metal hydrides *Proc. Natl Acad. Sci.* **117** 4021–6

[165] Renaudin G, Guénée L and Yvon K 2003 $LaMg_2NiH_7$, a novel quaternary metal hydride containing tetrahedral $[NiH_4]^{4-}$ complexes and hydride anions *J. Alloys Compd.* **350** 145–50

[166] Yvon K, Renaudin G, Wei C M and Chou M Y 2005 Hydrogenation-induced insulating state in the intermetallic compound $LaMg_2Ni$ *Phys. Rev. Lett.* **94** 066403

[167] Miwa K, Sato T, Matsuo M, Ikeda K, Otomo T, Deledda S, Hauback B C, Li G, Takagi S and Orimo S-I 2016 Metallic intermediate hydride phase of $LaMg_2Ni$ with Ni–H covalent bonding: precursor state for complex hydride formation *J. Phys. Chem.* C **120** 5926–31

[168] Sato T, Ikeda K, Matsuo M, Miwa K, Otomo T, Deledda S, Hauback B C, Li G, Takagi S and Orimo S 2017 *In-situ* powder neutron diffraction study on the formation process of $LaMg_2NiH_7$ *Int. J. Hydrog. Energy* **42** 22449–53

[169] Sato T, Ramirez-Cuesta A J, Daemen L L, Cheng Y and Orimo S 2018 Evidence of intermediate hydrogen states in the formation of a complex hydride *Inorg. Chem.* **57** 867–72

[170] Sato T, Daemen L L, Cheng Y, Ramirez-Cuesta A J, Ikeda K, Aoki T, Otomo T and Orimo S 2019 Hydrogen-release reaction of a complex transition metal hydride with covalently bound hydrogen and hydride ions *ChemPhysChem* **20** 1392–7
[171] Tomiyasu K, Sato T, Horigane K, Orimo S and Yamada K 2012 Hydrogen release from Li alanates originates in molecular lattice instability emerging at ∼100 K *Appl. Phys. Lett.* **100** 193901
[172] Sato T, Ramirez-Cuesta A J, Daemen L, Cheng Y-Q, Tomiyasu K, Takagi S and Orimo S 2016 Hydrogen release reactions of Al-based complex hydrides enhanced by vibrational dynamics and valences of metal cations *Chem. Commun.* **52** 11807–10
[173] Liang G, Huot J, Boily S, van Neste A and Schulz R 1999 Catalytic effect of transition metals on hydrogen sorption in nanocrystalline ball milled MgH_2–Tm (Tm = Ti, V, Mn, Fe and Ni) systems *J. Alloys Compd.* **292** 247–52
[174] Yao X, Zhu Z H, Cheng H M and Lu G Q 2008 Hydrogen diffusion and effect of grain size on hydrogenation kinetics in magnesium hydrides *J. Mater. Res.* **23** 336–40
[175] Vegge T 2004 Locating the rate-limiting step for the interaction of hydrogen with Mg(0001) using density-functional theory calculations and rate theory *Phys. Rev.* B **70** 035412
[176] Cuevas F, Korablov D and Latroche M 2012 Synthesis, structural and hydrogenation properties of Mg-rich MgH_2–TiH_2 nanocomposites prepared by reactive ball milling under hydrogen gas *Phys. Chem. Chem. Phys.* **14** 1200
[177] Huot J, Ravnsbæk D B, Zhang J, Cuevas F, Latroche M and Jensen T R 2013 Mechanochemical synthesis of hydrogen storage materials *Prog. Mater. Sci.* **58** 30–75
[178] Rizo-Acosta P, Cuevas F and Latroche M 2018 Optimization of TiH_2 content for fast and efficient hydrogen cycling of MgH_2-TiH_2 nanocomposites *Int. J. Hydrog. Energy* **43** 16774–81
[179] Rizo-Acosta P, Cuevas F and Latroche M 2019 Hydrides of early transition metals as catalysts and grain growth inhibitors for enhanced reversible hydrogen storage in nanostructured magnesium *J. Mater. Chem.* A **7** 23064
[180] Lotoskyy M, Denys R, Yartys V A, Eriksen J, Goh J, Nyamsi S N, Sita C and Cummings F 2018 An outstanding effect of graphite in nano-MgH_2-TiH_2 on hydrogen storage performance *J. Mater. Chem.* A **6** 10740–54
[181] Lototskyy M, Goh J, Davids M W, Linkov V, Khotseng L, Ntsendwana B, Denys R and Yartys V A 2019 Nanostructured hydrogen storage materials prepared by high-energy reactive ball milling of magnesium and ferrovanadium *Int. J. Hydrog. Energy* **44** 6687–701
[182] Tarasov B P, Arbuzov A A, Mozhzhuhin S A, Volodin A A, Fursikov P V, Lototskyy M V and Yartys V A 2019 Hydrogen storage behavior of magnesium catalyzed by nickel-graphene nanocomposites *Int. J. Hydrog. Energy* **44** 29212–23
[183] Wu C Z, Wang P, Yao X, Liu C, Chen D M, Lu G Q and Cheng H M 2006 Effect of carbon/noncarbon addition on hydrogen storage behaviors of magnesium hydride *J. Alloys Compd.* **414** 259–64
[184] Bouaricha S, Dodelet J-P, Guay D, Huot J and Schulz R 2001 Study of the activation process of Mg-based hydrogen storage materials modified by graphite and other carbonaceous compounds *J. Mater. Res.* **16** 2893–905
[185] Panella B, Hirscher M and Roth S 2005 Hydrogen adsorption in different carbon nanostructures *Carbon* **43** 2209–14
[186] Adelhelm P and de Jongh P E 2011 The impact of carbon materials on the hydrogen storage properties of light metal hydrides *J. Mater. Chem.* **21** 2417–27
[187] Lillo-Ródenas M A, Guo Z X, Aguey-Zinsou K F, Cazorla-Amorós D and Linares-Solano A 2008 Effects of different carbon materials on MgH_2 decomposition *Carbon* **46** 126–37
[188] Popilevsky L, Skripnyuk V M, Beregovsky M, Sezen M, Amouyal Y and Rabkin E 2016 Hydrogen storage and thermal transport properties of pelletized porous Mg-2 wt.% multiwall carbon nanotubes and Mg-2 wt.% graphite composites *Int. J. Hydrog. Energy* **41** 14461–74
[189] Popilevsky L, Skripnyuk V M, Amouyal Y and Rabkin E 2017 Tuning the thermal conductivity of hydrogenated porous magnesium hydride composites with the aid of carbonaceous additives *Int. J. Hydrog. Energy* **42** 22395–405
[190] Zhang L, Sun Z, Cai Z, Yan N, Lu X, Zhu X and Chen L 2020 Enhanced hydrogen storage properties of MgH_2 by the synergetic catalysis of $Zr_{0.4}Ti_{0.6}Co$ nanosheets and carbon nanotubes *Appl. Surf. Sci.* **504** 144465
[191] Yahya M S and Ismail M 2018 Improvement of hydrogen storage properties of MgH_2 catalyzed by K_2NbF_7 and multiwall carbon nanotube *J. Phys. Chem.* C **122** 11222–33
[192] Ruse E, Pevzner S, Pri Bar I, Nadiv R, Skripnyuk V M, Rabkin E and Regev O 2016 Hydrogen storage and spillover kinetics in carbon nanotube-Mg composites *Int. J. Hydrog. Energy* **41** 2814–9
[193] Ruse E, Buzaglo M, Pevzner S, Pri-Bar I, Skripnyuk V M, Rabkin E and Regev O 2017 Tuning Mg hydriding kinetics with nanocarbons *J. Alloys Compd.* **725** 616–22
[194] Kim K C, Dai B, Karl Johnson J and Sholl D S 2009 Assessing nanoparticle size effects on metal hydride thermodynamics using the Wulff construction *Nanotechnology* **20** 204001
[195] Hao S Q and Sholl D S 2012 Effect of TiH_2-induced strain on thermodynamics of hydrogen release from MgH_2 *J. Phys. Chem.* C **116** 2045–50
[196] Sofianos M V, Sheppard D A, Rowles M R, Humphries T D, Liu S and Buckley C E 2017 Novel synthesis of porous Mg scaffold as a reactive containment vessel for $LiBH_4$ *RSC Adv.* **7** 36340–50
[197] Mooij L P A, Baldi A, Boelsma C, Shen K, Wagemaker M, Pivak Y, Schreuders H, Griessen R and Dam B 2011 Interface energy controlled thermodynamics of nanoscale metal hydrides *Adv. Energy Mater.* **1** 754–8
[198] Patelli N, Calizzi M, Migliori A, Morandi V and Pasquini L 2017 Hydrogen desorption below 150 °C in MgH_2–TiH_2 composite nanoparticles: equilibrium and kinetic properties *J. Phys. Chem.* C **121** 11166–77
[199] Wood B C *et al* 2019 HyMARC: LLNL activities *Proc. 2019 DOE Hydrogen Program Annual Merit Review*
[200] Pasquini L, Sacchi M, Brighi M, Boelsma C, Bals S, Perkisas T and Dam B 2014 Hydride destabilization in core-shell nanoparticles *Int. J. Hydrog. Energy* **39** 2115–23
[201] Duan X, Griessen R, Wijngaarden R J, Kamin S and Liu N 2018 Self-recording and manipulation of fast long-range hydrogen diffusion in quasifree magnesium *Phys. Rev. Mater.* **2** 085802
[202] Nielsen T K, Besenbacher F and Jensen T R 2011 Nanoconfined hydrides for energy storage *Nanoscale* **3** 2086–98
[203] Zlotea C, Oumellal Y, Hwang S-J, Ghimbeu C M, de Jongh P E and Latroche M 2015 Ultrasmall MgH_2 nanoparticles embedded in an ordered microporous carbon exhibiting rapid hydrogen sorption kinetics *J. Phys. Chem.* C **119** 18091–8
[204] Nielsen T K, Manickam K, Hirscher M, Besenbacher F and Jensen T R 2009 Confinement of MgH_2 nanoclusters within nanoporous aerogel scaffold materials *ACS Nano* **3** 3521–8
[205] Zhang X, Liu Y, Ren Z, Zhang X, Hu J, Huang Z, Lu Y, Gao M and Pan H 2021 Realizing 6.7 wt% reversible storage of hydrogen at ambient temperature with non-confined ultrafine magnesium hydrides *Energy Environ. Sci.* **14** 2302–13

[206] Wan L F, Liu Y-S, Cho E S, Forster J D, Jeong S, Wang H-T, Urban J J, Guo J and Prendergast D 2017 Atomically thin interfacial suboxide key to hydrogen storage performance enhancements of magnesium nanoparticles encapsulated in reduced graphene oxide *Nano Lett.* **17** 5540–5

[207] Cho E S *et al* 2017 Hierarchically controlled inside-out doping of Mg nanocomposites for moderate temperature hydrogen storage *Adv. Funct. Mater.* **27** 1704316

[208] Xia G, Tan Y, Chen X, Sun D, Guo Z, Liu H, Ouyang L, Zhu M and Yu X 2015 Monodisperse magnesium hydride nanoparticles uniformly self-assembled on graphene *Adv. Mater.* **27** 5981–8

[209] Wan L F *et al* 2019 Edge-functionalized graphene nanoribbon encapsulation to enhance stability and control kinetics of hydrogen storage materials *Chem. Mater.* **31** 2960–70

[210] Hamm M, Bongers M D, Roddatis V, Dietrich S, Lang K-H and Pundt A 2019 *In situ* observation of hydride nucleation and selective growth in magnesium thin-films with environmental transmission electron microscopy *Int. J. Hydrog. Energy* **44** 32112–23

[211] Baldi A, Mooij L, Palmisano V, Schreuders H, Krishnan G, Kooi B J, Dam B and Griessen R 2018 Elastic versus alloying effects in Mg-based hydride films *Phys. Rev. Lett.* **121** 255503

[212] Tang F, Parker T, Li H-F, Wang G-C and Lu T-M 2008 The Pd catalyst effect on low temperature hydrogen desorption from hydrided ultrathin Mg nanoblades *Nanotechnology* **19** 465706

[213] Ouyang L, Tang J, Zhao Y, Wang H, Yao X, Liu J, Zou J and Zhu M 2015 Express penetration of hydrogen on Mg(10$\bar{1}$0)13) along the close-packed-planes *Sci. Rep.* **5** 10776

[214] Ares J R 2018 Uncovering critical parameters in hydrogenation properties of magnesium films *16th Int. Symp. on Metal-Hydrogen Systems* (*Guanzhou*)

[215] Niessen R A H and Notten P H L 2005 Electrochemical hydrogen storage characteristics of thin film MgX (X = Sc, Ti, V, Cr) compounds *Electrochem. Solid-State Lett.* **8** A534

[216] Borsa D M, Baldi A, Pasturel M, Schreuders H, Dam B, Griessen R, Vermeulen P and Notten P H L 2006 Mg–Ti–H thin films for smart solar collectors *Appl. Phys. Lett.* **88** 241910

[217] Borsa D M, Gremaud R, Baldi A, Schreuders H, Rector J H, Kooi B, Vermeulen P, Notten P H L, Dam B and Griessen R 2007 Structural, optical, and electrical properties of MgyTi1-yHx thin films *Phys. Rev.* B **75** 205408

[218] Kim H, Schreuders H, Sakaki K, Asano K, Nakamura Y, Maejima N, Machida A, Watanuki T and Dam B 2020 Unveiling nanoscale compositional and structural heterogeneities of highly textured $Mg_{0.7}Ti_{0.3}H_y$ thin films *Inorg. Chem.* **59** 6800–7

[219] Egami T and Billinge S J L 2012 *Underneath the Bragg Peaks: Structural Analysis of Complex Materials* 2nd edn vol **16** (Oxford: Pergamon), pp 1–481

[220] El Kharbachi A *et al* 2020 Metal hydrides and related materials. Energy carriers for novel hydrogen and electrochemical storage *J. Phys. Chem.* C **124** 7599–607

[221] Bannenberg L J *et al* 2020 Metal (boro-) hydrides for high energy density storage and relevant emerging technologies *Int. J. Hydrog. Energy* **45** 33687–730

[222] Bellosta von Colbe J *et al* 2019 Application of hydrides in hydrogen storage and compression: achievements, outlook and perspectives *Int. J. Hydrog. Energy* **44** 7780–808

[223] Zijlstra H and Westendorp F F 1969 Influence of hydrogen on the magnetic properties of $SmCo_5$ *Solid State Commun.* **7** 857–9

[224] European Commission 2017 *Commission's communication on the 2017 list of critical raw materials for the EU* COM 490 European Union

[225] European Commission 2020 *Critical raw materials resilience: charting a path towards greater security and sustainability. Communication from the commission to the European parliament, the council, the European Economic and Social Committee and the committee of the regions* COM 474 European Union

[226] Endo N, Suzuki S, Goshome K and Maeda T 2017 Operation of a bench-scale TiFe-based alloy tank under mild conditions for low-cost stationary hydrogen storage *Int. J. Hydrog. Energy* **42** 5246–51

[227] HyCARE project 2019 HyCARE focuses on large-scale, solid-state hydrogen storage *Fuel Cells Bull.* **2019** 11

[228] Endo N, Shimoda E, Goshome K, Yamane T, Nozu T and Maeda T 2019 Construction and operation of hydrogen energy utilization system for a zero emission building *Int. J. Hydrog. Energy* **44** 14596–604

[229] Endo N, Shimoda E, Goshome K, Yamane T, Nozu T and Maeda T 2020 Operation of a stationary hydrogen energy system using TiFe-based alloy tanks under various weather conditions *Int. J. Hydrog. Energy* **45** 207–15

[230] Endo N, Saita I, Nakamura Y, Saitoh H and Machida A 2015 Hydrogenation of a TiFe-based alloy at high pressures and temperatures *Int. J. Hydrog. Energy* **40** 3283–7

[231] Modi P and Aguey-Zinsou K-F 2019 Titanium-iron-manganese ($TiFe_{0.85}Mn_{0.15}$) alloy for hydrogen storage: reactivation upon oxidation *Int. J. Hydrog. Energy* **44** 16757–64

[232] Schlapbach L and Riesterer T 1983 The activation of FeTi for hydrogen absorption *Appl. Phys.* A **32** 169–82

[233] Kulshreshtha S K, Sasikala R, Pushpa K K, Rao K A and Iyer R M 1989 On activation of FeTi: surface effects *Mater. Res. Bull.* **24** 545–50

[234] Zhu H Y, Wu J and Wang Q D 1992 Disproportionation of $LaNi_5$ and TiFe in 4 MPa H_2 at 300 °C *J. Alloys Compd.* **185** 1–6

[235] Zeaiter A, Nardin P, Pour Yazdi M A and Billard A 2019 Outstanding shortening of the activation process stage for a TiFe-based hydrogen storage alloy *Mater. Res. Bull.* **112** 132–41

[236] Zadorozhnyy V Y, Milovzorov G S, Klyamkin S N, Zadorozhnyy M Y, Strugova D V, Gorshenkov M V and Kaloshkin S D 2017 Preparation and hydrogen storage properties of nanocrystalline TiFe synthesized by mechanical alloying *Prog. Nat. Sci.: Mater. Int.* **27** 149–55

[237] Dematteis E M, Dreistadt D M, Capurso G, Jepsen J, Cuevas F and Latroche M 2021 Fundamental hydrogen storage properties of TiFe-alloy with partial substitution of Fe by Ti and Mn *J. Alloys Compd.* **874** 159925

[238] Singh B K, Singh A K and Srivastava O N 1996 Improved hydrogen sorption characteristics in $FeTi_{1+x}$Mm material *Int. J. Hydrog. Energy* **21** 111–7

[239] Bratanich T I, Solonin S M and Skorokhod V V 1995 Mechanical activation of hydrogen sorption with intermetallic compounds $LaNi_5$ and TiFe in powder systems *Int. J. Hydrog. Energy* **20** 353–5

[240] Bakulin A V, Kulkov S S, Kulkova S E, Hocker S and Schmauder S 2014 Influence of substitutional impurities on hydrogen diffusion in B2-TiFe alloy *Int. J. Hydrog. Energy* **39** 12213–20

[241] Buchner H 1982 *Energiespeicherung in Metallhydriden* (Vienna: Springer Vienna)

[242] Dematteis E M, Cuevas F and Latroche M 2021 Hydrogen storage properties of Mn and Cu for Fe substitution in $TiFe_{0.9}$ intermetallic compound *J. Alloys Compd.* **851** 156075

[243] Leng H, Yu Z, Yin J, Li Q, Wu Z and Chou K-C 2017 Effects of Ce on the hydrogen storage properties of $TiFe_{0.9}Mn_{0.1}$ alloy *Int. J. Hydrog. Energy* **42** 23731–6

[244] Ćirić K D, Kocjan A, Gradišek A, Koteski V J, Kalijadis A M, Ivanovski V N, Laušević Z V and Stojić D L 2012 A study on crystal structure, bonding and hydriding properties of Ti–Fe–Ni intermetallics—behind substitution of iron by nickel *Int. J. Hydrog. Energy* **37** 8408–17

[245] Lim S H and Jai-Young L 1984 The effects of aluminium substitution in TiFe on its hydrogen absorption properties *J. Less-Common Met.* **97** 65–71

[246] Qu H, Du J, Pu C, Niu Y, Huang T, Li Z, Lou Y and Wu Z 2015 Effects of Co introduction on hydrogen storage properties of Ti–Fe–Mn alloys *Int. J. Hydrog. Energy* **40** 2729–35

[247] Guéguen A and Latroche M 2011 Influence of the addition of vanadium on the hydrogenation properties of the compounds $TiFe_{0.9}V_x$ and $TiFe_{0.8}Mn_{0.1}V_x$ ($x = 0$, 0.05 and 0.1) *J. Alloys Compd.* **509** 5562–6

[248] Yamashita I, Tanaka H, Takeshita H, Kuriyama N, Sakai T and Uehara I 1997 Hydrogenation characteristics of $TiFe_{1-x}Pd_x$ ($0.05 \leqslant x \leqslant 0.30$) alloys *J. Alloys Compd.* **253–254** 238–40

[249] Dematteis E M, Berti N, Cuevas F, Latroche M and Baricco M 2021 Substitutional effects in TiFe for hydrogen storage: a comprehensive review *Mater. Adv.* **2** 2524–60

[250] Ha T, Lee S-I, Hong J, Lee Y-S, Kim D-I, Suh J-Y, Cho Y W, Hwang B, Lee J and Shim J-H 2021 Hydrogen storage behavior and microstructural feature of a TiFe–$ZrCr_2$ alloy *J. Alloys Compd.* **853** 157099

[251] Kim H *et al* 2021 Activation of Ti–Fe–Cr alloys containing identical AB_2 fractions *J. Alloys Compd.* **864** 158876

[252] Jung J Y, Lee Y-S, Suh J-Y, Huh J-Y and Cho Y W 2021 Tailoring the equilibrium hydrogen pressure of TiFe via vanadium substitution *J. Alloys Compd.* **854** 157263

[253] Davids M W, Lototskyy M, Nechaev A, Naidoo Q, Williams M and Klochko Y 2011 Surface modification of TiFe hydrogen storage alloy by metal-organic chemical vapour deposition of palladium *Int. J. Hydrog. Energy* **36** 9743–50

[254] Williams M, Lototsky M V, Davids M W, Linkov V, Yartys V A and Solberg J K 2011 Chemical surface modification for the improvement of the hydrogenation kinetics and poisoning resistance of TiFe *J. Alloys Compd.* **509** S770–4

[255] Suda T, Ohkawa M, Sawada S, Watanabe S, Ohnuki S and Nagata S 2002 Effect of surface modification by ion implantation on hydrogenation property of TiFe alloy *Mater. Trans.* **43** 2703–5

[256] Bellosta von Colbe J M, Puszkiel J, Capurso G, Franz A, Benz H U, Zoz H, Klassen T and Dornheim M 2019 Scale-up of milling in a 100 L device for processing of TiFeMn alloy for hydrogen storage applications: procedure and characterization *Int. J. Hydrog. Energy* **44** 29282–90

[257] Huot J 2016 *Enhancing Hydrogen Storage Properties of Metal Hybrides* (Cham: Springer International Publishing)

[258] Vega L E R, Leiva D R, Leal Neto R M, Silva W B, Silva R A, Ishikawa T T, Kiminami C S and Botta W J 2018 Mechanical activation of TiFe for hydrogen storage by cold rolling under inert atmosphere *Int. J. Hydrog. Energy* **43** 2913–8

[259] Edalati K, Matsuda J, Yanagida A, Akiba E and Horita Z 2014 Activation of TiFe for hydrogen storage by plastic deformation using groove rolling and high-pressure torsion: similarities and differences *Int. J. Hydrog. Energy* **39** 15589–94

[260] Haraki T, Oishi K, Uchida H, Miyamoto Y, Abe M, Kokaji T and Uchida S 2008 Properties of hydrogen absorption by nano-structured FeTi alloys *Int. J. Mater. Res.* **99** 507–12

[261] Edalati K, Matsuo M, Emami H, Itano S, Alhamidi A, Staykov A, Smith D J, Orimo S, Akiba E and Horita Z 2016 Impact of severe plastic deformation on microstructure and hydrogen storage of titanium-iron-manganese intermetallics *Scr. Mater.* **124** 108–11

[262] Sujan G K, Pan Z, Li H, Liang D and Alam N 2020 An overview on TiFe intermetallic for solid-state hydrogen storage: microstructure, hydrogenation and fabrication processes *Crit. Rev. Solid State Mater. Sci.* **45** 410–27

[263] Lv P, Guzik M N, Sartori S and Huot J 2019 Effect of ball milling and cryomilling on the microstructure and first hydrogenation properties of TiFe+4 wt.% Zr alloy *J. Mater. Res. Technol.* **8** 1828–34

[264] Manna J, Tougas B and Huot J 2020 First hydrogenation kinetics of Zr and Mn doped TiFe alloy after air exposure and reactivation by mechanical treatment *Int. J. Hydrog. Energy* **45** 11625–31

[265] Izanlou A and Aydinol M K 2010 An *ab initio* study of dissociative adsorption of H_2 on FeTi surfaces *Int. J. Hydrog. Energy* **35** 1681–92

[266] Wood B C *et al* 2021 HyMARC: LLNL activities *Proc. 2021 DOE Hydrogen Program Annual Merit Review*

[267] Heo T W, Grieder A, Wang B, Wood M, Hsu T, Akhade S A, Wan L F, Chen L-Q, Adelstein N and Wood B C 2021 Microstructural impacts on ionic conductivity of oxide solid electrolytes from a combined atomistic-mesoscale approach *npj Comput. Mater.* **7** 214

[268] Young K-H, Nei J, Wan C, Denys R V and Yartys V A 2017 Comparison of C14- and C15-predomiated AB_2 metal hydride alloys for electrochemical applications *Batteries* **3** 22

[269] Young K-H, Koch J M, Wan C, Denys R V and Yartys V A 2017 Cell performance comparison between C14- and C15-predomiated AB_2 metal hydride alloys *Batteries* **3** 29

[270] Yartys V A *et al* 2021 HYDRIDE4MOBILITY: an EU HORIZON 2020 project on hydrogen powered fuel cell utility vehicles using metal hydrides in hydrogen storage and refuelling systems *Int. J. Hydrog. Energy* **46** 35896–909

[271] Wan C, Denys R V and Yartys V A 2021 Effects of Ti substitution for Zr on the electrochemical characteristics and structure of AB_2-type Laves-phase alloys as metal hydride anodes *J. Alloys Compd.* **889** 161655

[272] Volodin A A, Denys R V, Wan C, Wijayanti I D, Suwarno S, Tarasov B P, Antonov V E and Yartys V A 2019 Study of hydrogen storage and electrochemical properties of AB_2-type $Ti_{0.15}Zr_{0.85}La_{0.03}Ni_{1.2}Mn_{0.7}V_{0.12}Fe_{0.12}$ alloy *J. Alloys Compd.* **793** 564–75

[273] Wijayanti I D, Denys R, Suwarno S, Volodin A A, Lototskyy M V, Guzik M N, Nei J, Young K, Roven H J and Yartys V 2020 Hydrides of Laves type Ti–Zr alloys with enhanced H storage capacity as advanced metal hydride battery anodes *J. Alloys Compd.* **828** 154354

[274] Wan C, Denys R V, Lelis M, Milčius D and Yartys V A 2019 Electrochemical studies and phase-structural characterization of a high-capacity La-doped AB_2 Laves type alloy and its hydride *J. Power Sources* **418** 193–201

[275] Wijayanti I D, Mølmen L, Denys R V, Nei J, Gorsse S, Guzik M N, Young K and Yartys V 2019 Studies of Zr-based C15 type metal hydride battery anode alloys prepared by rapid solidification *J. Alloys Compd.* **804** 527–37

[276] Wijayanti I D, Mølmen L, Denys R V, Nei J, Gorsse S, Young K, Guzik M N and Yartys V 2020 The electrochemical performance of melt-spun C14-Laves type TiZr-based alloy *Int. J. Hydrog. Energy* **45** 1297–303

[277] Wijayanti I, Mølmen L, Denys R, Guzik M, Gorsse S and Yartys V 2021 Studies of the effect of melt spinning on the electrochemical properties of the AB_2 Laves phase alloys *Int. J. Mech. Eng. Sci.* **5** 24–29

[278] Hariyadi A, Suwarno S, Denys R V, von Colbe J B, Sætre T O and Yartys V 2022 Modeling of the hydrogen sorption kinetics in an AB_2 laves type metal hydride alloy *J. Alloys Compd.* **893** 162135
[279] Lozano G A, Eigen N, Keller C, Dornheim M and Bormann R 2009 Effects of heat transfer on the sorption kinetics of complex hydride reacting systems *Int. J. Hydrog. Energy* **34** 1896–903
[280] Shafiee S and McCay M H 2016 Different reactor and heat exchanger configurations for metal hydride hydrogen storage systems—a review *Int. J. Hydrog. Energy* **41** 9462–70
[281] Puszkiel J, Bellosta von Colbe J M, Jepsen J, Mitrokhin S V, Movlaev E, Verbetsky V and Klassen T 2020 Designing an AB_2-type alloy (TIZr-CrMNMO) for the hybrid hydrogen storage concept *Energies* **13** 2751
[282] Jepsen J *et al* 2018 Fundamental material properties of the $2LiBH_4$-MgH_2 reactive hydride composite for hydrogen storage: (I) thermodynamic and heat transfer properties *Energies* **11** 1081
[283] Bürger I, Sourmelis Terzopoulos V E, Kretschmer C, Kölbig M, Brack C and Linder M 2021 Lightweight reactor design by additive manufacturing for preheating applications using metal hydrides *Int. J. Hydrog. Energy* **46** 28686–99
[284] Bedrunka M, Bornemann N, Steinebach G and Reith D 2021 A metal hydride system for a forklift: feasibility study on on-board chemical storage of hydrogen using numerical simulation *Int. J. Hydrog. Energy* **47** 12240–50
[285] Visaria M, Mudawar I, Pourpoint T and Kumar S 2010 Study of heat transfer and kinetics parameters influencing the design of heat exchangers for hydrogen storage in high-pressure metal hydrides *Int. J. Heat Mass Transfer* **53** 2229–39
[286] Visaria M, Mudawar I and Pourpoint T 2011 Enhanced heat exchanger design for hydrogen storage using high-pressure metal hydride: part 1. Design methodology and computational results *Int. J. Heat Mass Transfer* **54** 413–23
[287] Chaise A, de Rango P, Marty P, Fruchart D, Miraglia S, Olivès R and Garrier S 2009 Enhancement of hydrogen sorption in magnesium hydride using expanded natural graphite *Int. J. Hydrog. Energy* **34** 8589–96
[288] Pohlmann C, Röntzsch L, Heubner F, Weißgärber T and Kieback B 2013 Solid-state hydrogen storage in hydralloy–graphite composites *J. Power Sources* **231** 97–105
[289] Visaria M, Mudawar I and Pourpoint T 2011 Enhanced heat exchanger design for hydrogen storage using high-pressure metal hydride—part 2. Experimental results *Int. J. Heat Mass Transfer* **54** 424–32
[290] Miracle D B and Senkov O N 2017 A critical review of high entropy alloys and related concepts *Acta Mater.* **122** 448–511
[291] Marques F, Balcerzak M, Winkelmann F, Zepon G and Felderhoff M 2021 Review and outlook on high-entropy alloys for hydrogen storage *Energy Environ. Sci.* **14** 5191–227
[292] Sahlberg M, Karlsson D, Zlotea C and Jansson U 2016 Superior hydrogen storage in high entropy alloys *Sci. Rep.* **6** 36770
[293] Zlotea C *et al* 2019 Hydrogen sorption in TiZrNbHfTa high entropy alloy *J. Alloys Compd.* **775** 667–74
[294] Poletti M G and Battezzati L 2014 Electronic and thermodynamic criteria for the occurrence of high entropy alloys in metallic systems *ACTA Mater.* **75** 297–306
[295] Spaliviero U, Poletti M G, Battezzati L and Baricco M 2019 Hydrogen sorption in $TiV_{0.6}Cr_{0.3}Zr_{0.3}NbMo$ high entropy alloy *Metall. Ital.* **9** 14–21
[296] Akiba E and Iba H 1998 Hydrogen absorption by Laves phase related BCC solid solution *Intermetallics* **6** 461–70
[297] Nygård M M, Ek G, Karlsson D, Sørby M H, Sahlberg M and Hauback B C 2019 Counting electrons—a new approach to tailor the hydrogen sorption properties of high-entropy alloys *Acta Mater.* **175** 121–9
[298] Witman M, Ek G, Ling S, Chames J, Agarwal S, Wong J, Allendorf M D, Sahlberg M and Stavila V 2021 Data-driven discovery and synthesis of high entropy alloy hydrides with targeted thermodynamic stability *Chem. Mater.* **33** 4067–76
[299] Nygård M M *et al* 2021 The average and local structure of $TiVCrNbD_x$ (x = 0,2.2,8) from total scattering and neutron spectroscopy *Acta Mater.* **205** 116496
[300] Nygård M M, Ek G, Karlsson D, Sahlberg M, Sørby M H and Hauback B C 2019 Hydrogen storage in high-entropy alloys with varying degree of local lattice strain *Int. J. Hydrog. Energy* **44** 29140–9
[301] Hattrick-Simpers J R, Choudhary K and Corgnale C 2018 A simple constrained machine learning model for predicting high-pressure-hydrogen-compressor materials *Mol. Syst. Des. Eng.* **3** 509–17
[302] Witman M, Ling S L, Grant D M, Walker G S, Agarwal S, Stavila V and Allendorf M D 2020 Extracting an empirical intermetallic hydride design principle from limited data via interpretable machine learning *J. Phys. Chem. Lett.* **11** 40–47
[303] Ward L, Agrawal A, Choudhary A and Wolverton C 2016 A general-purpose machine learning framework for predicting properties of inorganic materials *npj Comput. Mater.* **2** 16028
[304] Ward L *et al* 2018 Matminer: an open source toolkit for materials data mining *Comput. Mater. Sci.* **152** 60–69
[305] Evans J D, Bon V, Senkovska I and Kaskel S 2021 A universal standard archive file for adsorption data *Langmuir* **37** 4222–6
[306] Jain A *et al* 2013 Commentary: The Materials Project: a materials genome approach to accelerating materials innovation *APL Mater.* **1** 11002
[307] Babai D, Bereznitsky M, Mogilyanski D, Filipek S M, Shneck R Z and Jacob I 2018 Hydrogen sorption behavior of some Pd-containing compounds *J. Alloys Compd.* **750** 206–12
[308] Babai D, Bereznitsky M, Shneck R Z and Jacob I 2020 Mutual impact of crystal volume and heat of alloy formation on hydride stabilities in $Zr(Pd_xCr_{1-x})_2$ and similar intermetallics *J. Alloys Compd.* **814** 152268
[309] Babai D, Bereznitsky M, Shneck R Z and Jacob I 2022 The effect of Pd on hydride formation in $Zr(Pd_xM_{1-x})_2$ intermetallics where M is a 3d element *J. Alloys Compd.* **889** 161503
[310] Maeland A J and Libowitz G G 1980 Hydrogen absorption in some A_2B intermetallic compounds with the $MoSi_2$-type structure ($C11_b$) *J. Less-Common Met.* **74** 295–300
[311] Jacob I, Bereznitsky M, Yeheskel O and Leisure R G 2006 Role of shear stiffening in reducing hydrogenation in intermetallic compounds *Appl. Phys. Lett.* **89** 201909
[312] Lartigue C 1984 Etude structurale et thermodynamique du systeme $LaNi_{5-X}Mn_X$—hydrogene *PhD Thesis* Université Paris VI
[313] King H W 1966 Quantitative size-factors for metallic solid solutions *J. Mater. Sci.* **1** 79–90
[314] Aoki K, Li X-G and Masumoto T 1992 Factors controlling hydrogen-induced amorphization of C15 Laves compounds *Acta Metall. Mater.* **40** 1717–26
[315] Bereznitsky M, Mogilyanski D, Jacob I, Denys R V, Chernyshov D and Yartys V A Thermodynamically stable ternary $LaMgPdH_5$ hydride based on ZrNiAl type intermetallic *16th Int. Symp. on Metal-Hydrogen Systems, MH2018* (*Guangzhou, China*, *28 October–2 November 2018*)
[316] Yartys V A, Gutfleisch O, Panasyuk V V and Harris I R 1997 Desorption characteristics of rare earth (R) hydrides (R = Y, Ce, Pr, Nd, Sm, Gd and Tb) in relation to the HDDR behaviour of R–Fe-based-compounds *J. Alloys Compd.* **253–254** 128–33
[317] Yartys V, Riabov A and Hauback B 2001 Neutron diffraction studies of Zr-containing intermetallic hydrides *J. Alloys Compd.* **317–318** 92–97

[318] Riabov A B, Yartys V A, Hauback B C, Guegan P W, Wiesinger G and Harris I R 1999 Hydrogenation behaviour, neutron diffraction studies and microstructural characterization of boron oxide-doped Zr-V alloys *J. Alloys Compd.* **293** 93–100
[319] Davids M W, Martin T, Lototskyy M, Denys R and Yartys V 2021 Study of hydrogen storage properties of oxygen modified Ti-based AB_2 type metal hydride alloy *Int. J. Hydrog. Energy* **46** 13658–63
[320] Suwarno S, Maehlen J P, Denys R V and Yartys V A 2019 Effect of oxygen on the mechanism of phase-structural transformations in O-containing titanium hydride *Int. J. Hydrog. Energy* **44** 24821–8
[321] Ben David R, Finkelstein Y, Grinberg E, Samuha S, Rabkin E and Cohen D 2020 Oxidation induced cubic-tetragonal phase transformation in titanium hydride powders *Int. J. Hydrog. Energy* **45** 25043–53
[322] Fromm E and Uchida H 1987 Surface phenomena in hydrogen absorption kinetics of metals and intermetallic compounds *J. Less-Common Met.* **131** 1–12
[323] Hadjixenophontos E, Michalek L, Roussel M, Hirscher M and Schmitz G 2018 The role of surface oxides on hydrogen sorption kinetics in titanium thin films *Appl. Surf. Sci.* **441** 324–30
[324] Bogdanovic B, Hartwig T H and Spliethoff B 1993 The development, testing and optimization of energy-storage materials based on the MgH_2-Mg system *Int. J. Hydrog. Energy* **18** 575–89
[325] Bogdanovic B and Spliethoff B 1987 Active MgH_2—Mg-systems for hydrogen storage *Int. J. Hydrog. Energy* **12** 863–73
[326] Bogdanovic B, Ritter A, Spliethoff B and Straburger K 1995 A process steam generator based on the high temperature magnesium hydride/magnesium heat storage system *Int. J. Hydrog. Energy* **20** 811–22
[327] Crivello J-C *et al* 2016 Mg-based compounds for hydrogen and energy storage *Appl. Phys.* A **122** 85
[328] Bogdanovic B, Hofmann H, Neuy A, Reiser A, Schlichte K, Spliethoff B and Wessel S 1999 Ni-doped versus undoped Mg-MgH_2 materials for high temperature heat or hydrogen storage *J. Alloys Compd.* **292** 57–71
[329] Verga M, Armanasco F, Guardamagna C, Valli C, Bianchin A, Agresti F, Lo Russo S, Maddalena A and Principi G 2009 Scaling up effects of Mg hydride in a temperature and pressure-controlled hydrogen storage device *Int. J. Hydrog. Energy* **34** 4602–10
[330] Delhomme B, de Rango P, Marty P, Bacia M, Zawilski B, Raufast C, Miraglia S and Fruchart D 2012 Large scale magnesium hydride tank coupled with an external heat source *Int. J. Hydrog. Energy* **37** 9103–11
[331] Felderhoff M and Bogdanović B 2009 High temperature metal hydrides as heat storage materials for solar and related applications *Int. J. Mol. Sci.* **10** 325–44
[332] Liu W, Zuo H, Wang J, Xue Q, Ren B and Yang F 2021 The production and application of hydrogen in steel industry *Int. J. Hydrog. Energy* **46** 10548–69
[333] Rambhujun N, Salman M S, Wang T, Pratthana C, Sapkota P, Costalin M, Lai Q and Aguey-Zinsou K-F 2020 Renewable hydrogen for the chemical industry *MRS Energy Sustain.* **7** 33
[334] Hardian R *et al* 2018 Waste Mg-Al based alloys for hydrogen storage *Int. J. Hydrog. Energy* **43** 16738–48
[335] Reilly J J and Sandrock G D 1980 Hydrogen storage in metal-hydrides *Sci. Am.* **242** 118-31
[336] Hasegawa K, Ohnishi M, Oshitani M, Takeshima K, Matsumaru Y and Tamura K 1994 Nickel—metal hydride battery *Z. Phys. Chem.* **183** 325–31
[337] Dhar S K, Ovshínsky S R, Gifford P R, Corrigan D A, Fetcenko M A and Venkatesan S 1997 Nickel/metal hydride technology for consumer and electric vehicle batteries—a review and up-date *J. Power Sources* **65** 1–7
[338] Capurso G, Schiavo B, Jepsen J, Lozano G, Metz O, Saccone A, de Negri S, von Colbe J M, Klassen T and Dornheim M 2016 Development of a modular room-temperature hydride storage system for vehicular applications *Appl. Phys.* A **122** 236
[339] Lototskyy M, Klochko Y, Linkov V, Lawrie P and Pollet B G 2012 Thermally driven metal hydride hydrogen compressor for medium-scale applications *Energy Proc.* **29** 347–56
[340] Weger L B, Leitão J and Lawrence M G 2021 Expected impacts on greenhouse gas and air pollutant emissions due to a possible transition towards a hydrogen economy in German road transport *Int. J. Hydrog. Energy* **46** 5875–90
[341] Husarek D, Schmugge J and Niessen S 2021 Hydrogen supply chain scenarios for the decarbonisation of a German multi-modal energy system *Int. J. Hydrog. Energy* **46** 38008–25
[342] Behling N, Williams M C and Managi S 2015 Fuel cells and the hydrogen revolution: analysis of a strategic plan in Japan *Econ. Anal. Policy* **48** 204–21
[343] Mitsugi C, Harumi A and Kenzo F 1998 WE-NET: Japanese hydrogen program *Int. J. Hydrog. Energy* **23** 159–65
[344] U.S. Department of Energy - Hydrogen Shot (available at: www.energy.gov/eere/fuelcells/hydrogen-shot)
[345] U.S. Department of Energy - Hydrogen Program Plan (available at: www.hydrogen.energy.gov/pdfs/hydrogen-program-plan-2020.pdf)
[346] Fuel Cell and Hydrogen Energy Association - Road Map to a US Hydrogen Economy (available at: www.fchea.org/us-hydrogen-study)
[347] Yartys V A and Lototskyy M V 2022 Laves type intermetallic compounds as hydrogen storage materials: A review *J. Alloys Compounds* **916** 165219